Experiments on Cold-Formed Steel Beams with Holes

Behrooz H. Soroori Rad

Thesis submitted to the Faculty of the Virginia Polytechnic Institute and State University

in partial fulfillment of the requirements for the degree of

Master of Science

In

Civil Engineering

Cristopher D. Moen, Chairperson

Carin L. Roberts-Wollmann

Thomas E. Cousins

May 3, 2010

Blacksburg, Virginia

Keywords: Cold-Formed Steel Beams, Holes, Elastic Buckling, Finite Element Analysis,

Direct Strength Method

Experiments on Cold-Formed Steel Beams with Holes

Behrooz H. Soroori Rad

Abstract

Experimental testing and elastic buckling studies were performed on 68 C-section cold-formed steel joists with unstiffened rectangular web holes. Four Steel Stud Manufacturers Association (SSMA) cross-section types; 800S200-33, 800S200-43, 1000S162-54, and 1200S162-97, were evaluated to explore the influence of holes on local, distortional, and global bucking failure modes. Hole depth was varied in the tests to identify trends in ultimate strength. Ultimate strength was observed to decrease with increasing hole depth for 800S200-33, 1200S162-97 cross-sections. Due to small number of specimen and unidentified behavior of the beams, a more in depth study of the behavior of 800S200-43 and 1000S162-54 beams are necessary. Local buckling of the unstiffened strip above the hole was observed to accompany distortional buckling at the hole for the locally slender 800S200-33 and 1000S162-54 cross-sections. Thin shell finite element eigen-buckling analysis of each joist specimen, including measured cross-section dimensions and tested boundary and loading conditions, were conducted in parallel with the experiments to identify those elastic buckling mode shapes which influence load-deformation response. The distortional and lateral-torsional buckling moments were observed to decrease with increasing hole depth while a contrasting behavior was captured for local buckling modes. A modification to the AISI Direct Strength Method equations for beams with slotted web-holes was compared against the experimental results with predictions lower than tested strength. Initial cross-section imperfections led to inclined webs which decreased the capacity of the beams. The use of a water-jet cutting process was employed successfully to

produce accurate holes sizes and locations in each joist specimen and is recommended for researchers and manufacturers as a method for custom fabrication of cold-formed steel members.

Acknowledgements

I am grateful for the guidance of my advisors, Dr. Cristopher Moen. He taught me that unexpected results are not devastating and often times more interesting than expected results. I appreciate the endless hours he spent reviewing and editing my manuscripts and thesis chapters. I would like to thank Kalyani Tipnis, who assisted with MTS set up, and Leonardo Hasbund, who helped me with the experiments. I could not have finished my lab work without the assistance of many people. I am indebted to the folks at the Thomas M. Murray laboratory who helped cutting beam holes including Brett Farmer and Dennis Huffman. I would like to thank Kayle Severin who happily assisted me emotionally and intellectually during the course of writing. Finally, I would like to thank my dad, Gholamreza Soroori Rad and my family who have supported me through my life and through my career as a graduate student.

Table of Contents

List of Figures

List of Tables

Chapter 1. Introduction

1.1 History and uses for cold-formed steel

The use of cold formed steel in the construction industry started in 1850's in the United States. Due to the lack of the material knowledge and an absence of a standard code, the application of this material was limited until 1946 when the first edition of the Specification for the Design of Light Gage Steel Structural Members was published by American Iron and Steel Institute (AISI, 1946). Nowadays the cold-formed steel members are widely used in the construction industry both as primary and secondary framing components including roof purlins, stay-in-place concrete forms, sandwich panels and wall panels. The broad application of cold-formed steel is due to several factors (Yu 2000): high strength to weight ratio, variety of available profile shapes, corrosion resistance, versatility of connection type (Hancock 2001), economical in transportation and erection, non-combustibility and recyclability.

Cold-formed steel members are produced either through press braking or by roll forming of thin steel sheets through a series of dies as shown in Figure 1.1 and Figure 1.2 respectively. The capacity of cold-formed steel members is controlled by the placement of the different plate elements in the cross-section; i.e. the loads are carried through the shape of the cross-section rather than the strength of steel.

Holes are provided within the cross-section elements to facilitate the passage of ductwork and to enable an easier handling of the cold-formed steel members. Figure 1.3 and Figure 1.4 illustrate two examples of such applications.

Figure 1.1. Press-braking of cold-formed steel sections (photo courtesy of Folsana)

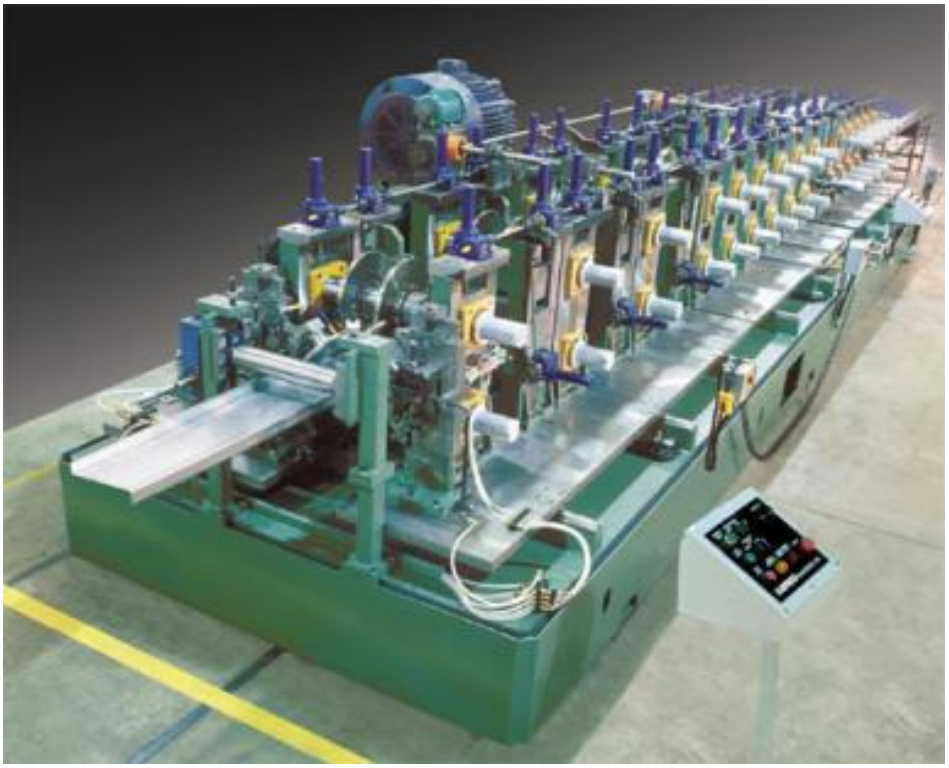

Figure 1.2. Roll-forming of cold-formed steel sections (photo courtesy of Samco machinery)

Figure 1.3. Web holes are provided in the roof purlins (photo courtesy of Steel framing)

Figure 1.4. Web holes are provided in the supporting beams (photo courtesy of Steel framing)

1.2 Design methods for cold-formed steel

Cold-formed steel structural members have locally slender cross-sections that tend to buckle under applied compressive stresses. Two design methods are currently provided by the American Iron and Steel Institute (AISI) for cold-formed steel members: the effective width method presented in the Main Specification (AISI-S100-07) and the Direct Strength Method (AISI-S100-07, Appendix 1). A detailed explanation of each method is provided in the following

sections. The effective width method relies on the strength provided by each element in the cross-section (e.g. web and flanges of a lipped C-section) while the Direct Strength Method (DSM) considers the stability of the whole cross-section including the interaction between the elements.

1.2.1 Effective width method

Because of their locally slender cross-sections, cold-formed steel members often exhibit local buckling before the steel reaches its yield strength. However, cold-formed steel members hold a considerable amount of post-buckling reserve. This post-buckling reserve is based on the fact that each plate element in the cross-section provides a continuous support for the adjacent elements and restraints the plate buckling which in turn increases the capacity of the member. A graphical illustration of this concept is provided in Figure 1.5.

The effective width method was first introduced in 1930's to calculate the strength of thin plates in compression and was later extended to the design of cold-formed steel members (von Karman, Sechler et al. 1932; Winter 1947).

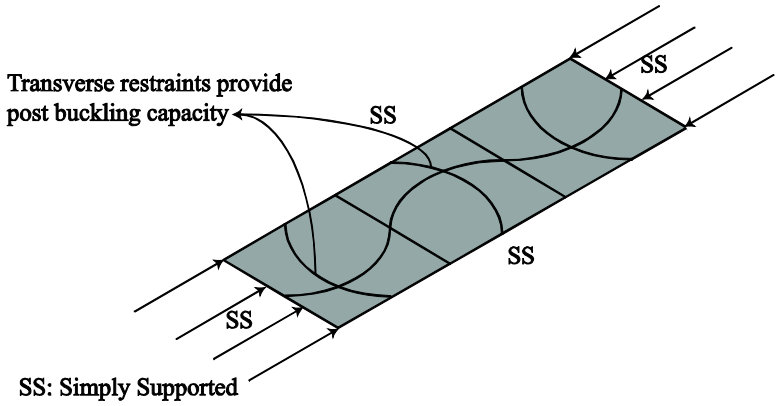

Figure 1.5. Illustration of transverse restraints in the buckling of the stiffened elements

Investigation of the development of stresses on a compression stiffened element in Figure 1.6 indicates that at early loading stages stress f is uniformly distributed across the width

of the element as shown in Figure 1.7. With an increase in the applied load, as f approach the yield stress, f_y, a non-uniform stress distribution with higher stresses applied at the stiffened edges is observed. Consequently, the element fails due to the yielding of the regions of maximum stress at the stiffened edges. The application of a non-uniform stress distribution in design is a complicated process. The effective width method simplifies the procedure by assuming that a uniform stress equal to f_{max} (stress at the edges of the stiffened plate) is applied on the reduced width b of the element as illustrated in

Figure 1.8. Therefore, the procedure for analysis and design of a cold-formed steel stiffened element is reduced to the calculation of the effective width b of the compression element and finding the capacity of the element ($P_n=f_{max}tb$ where t is the cross section thickness).

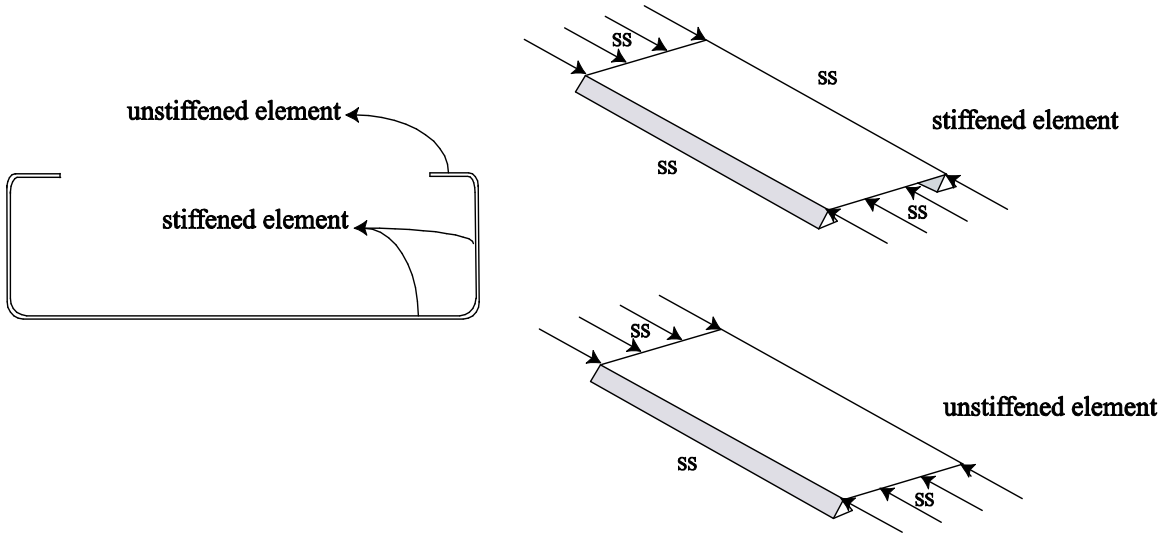

Figure 1.6. Illustration of a stiffened element and unstiffened element in a lipped C-section

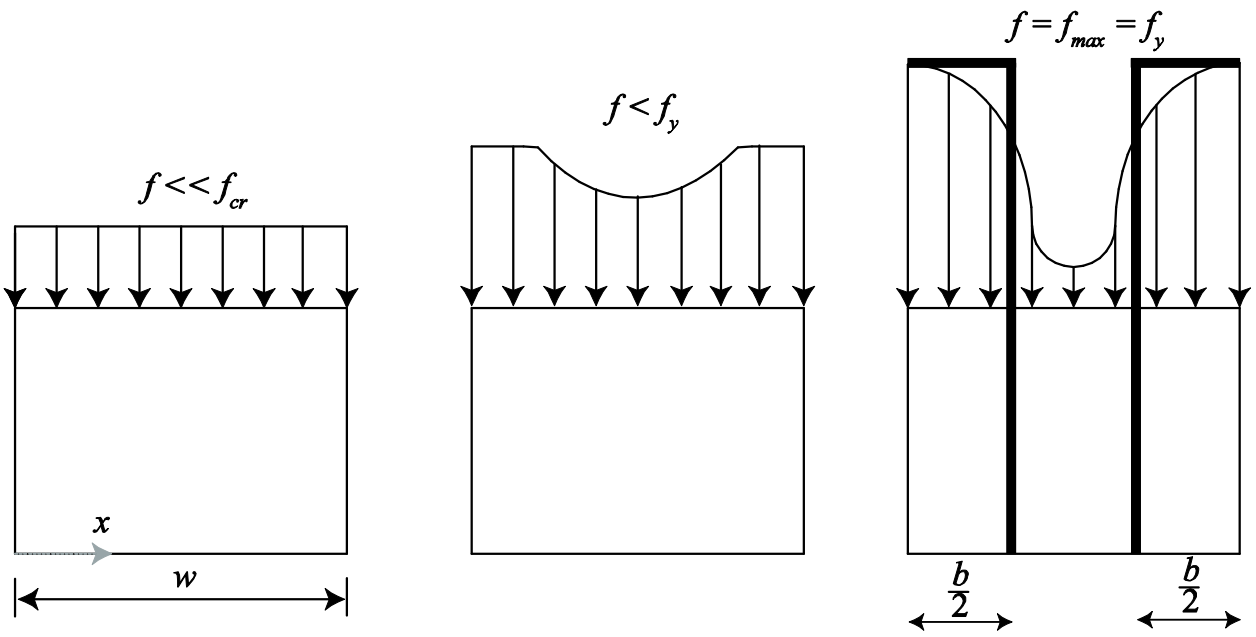

Figure 1.7. Stress distribution in stiffened plate element

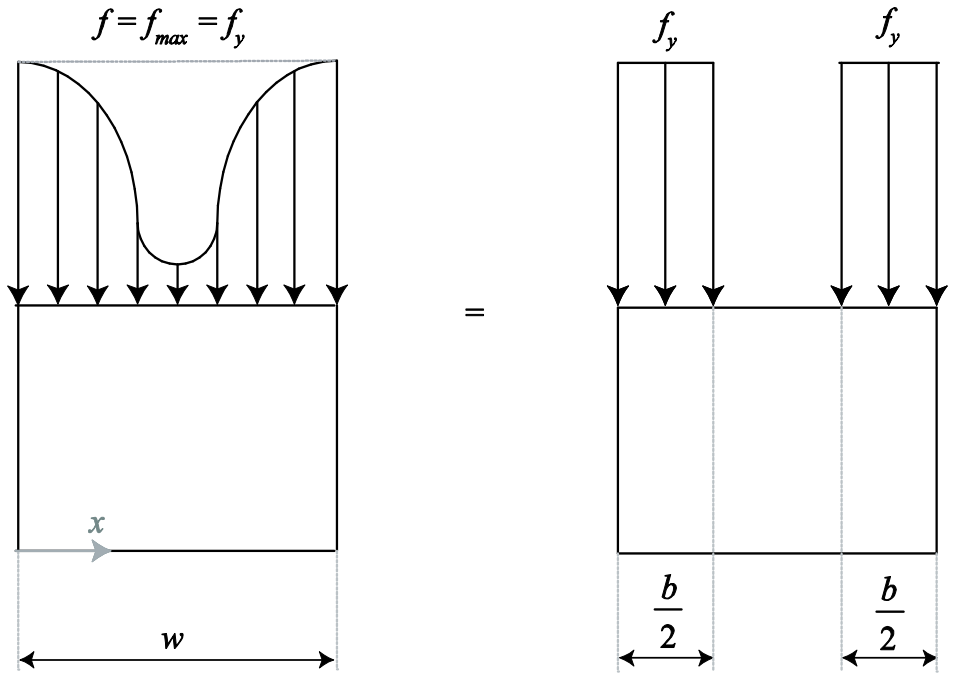

$$tbf_y = \int_0^w f t \, dx$$

Figure 1.8. Schematic illustration of the effective width concept

For the more complicated case such as the lipped C-section in bending shown in Figure 1.9, the effective width calculations are carried out for each of the compressive elements in the cross-section and the effective section modulus, S_e, is calculated with an iterative procedure considering the shift in neutral axis depth.

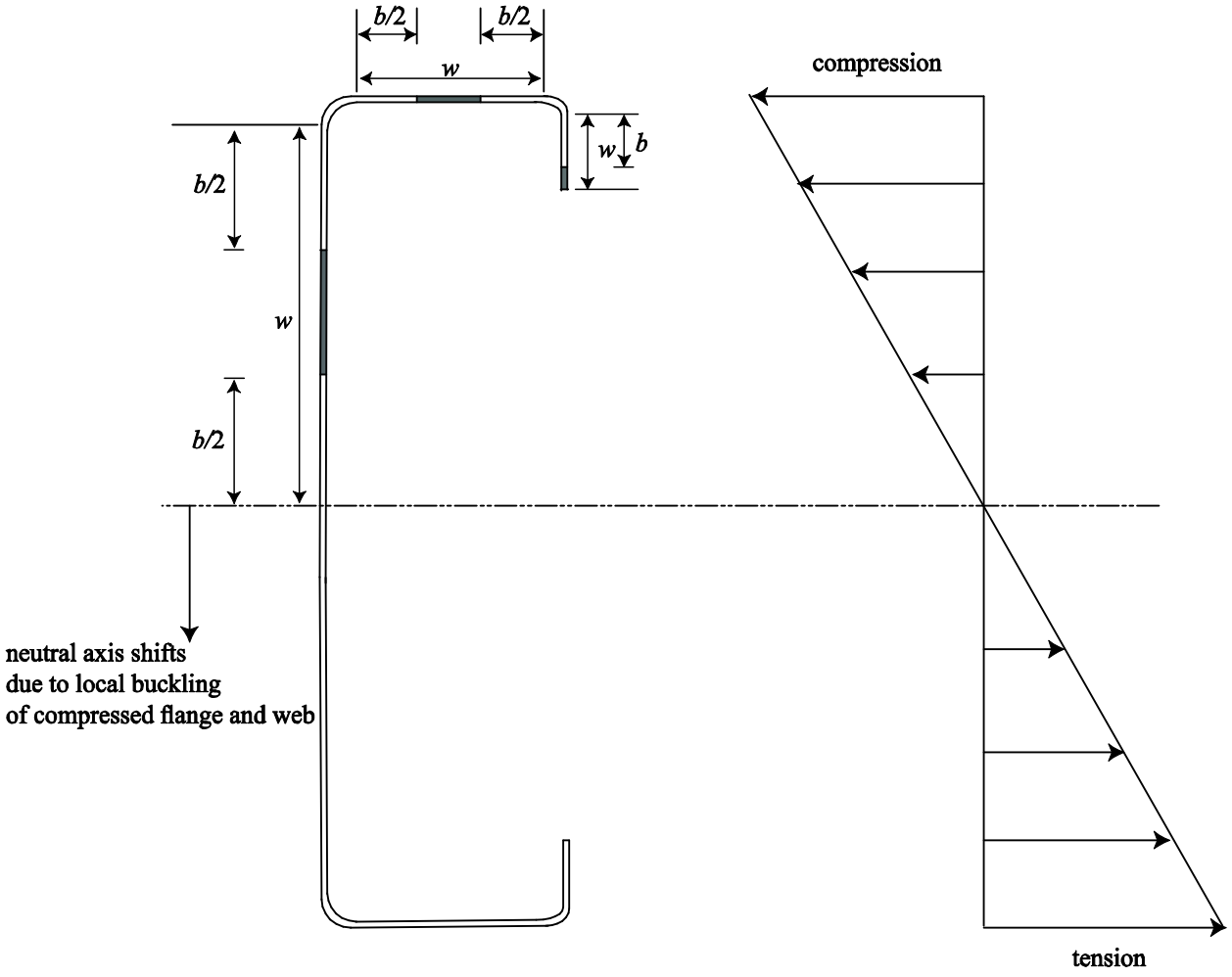

Figure 1.9. Effective width concept for cold-formed steel beams

The equations for calculating the effective width of a stiffened element are presented in the AISI North American Specification (AISI-S100 2007). The effective width calculations for a flange element of a C-section are summarized in Eq (1.2) through Eq (1.6). The two design limit states are local-global buckling interaction and distortional buckling.

$$M_n = \min(S_e f_y, M_{nd}) \tag{1.1}$$

where M_n is the nominal section strength, S_e is the effective modulus about a given axis computed at the yield stress, M_{nd} is the distortional buckling strength. The distortional buckling design curve is shown in Figure 1.10.

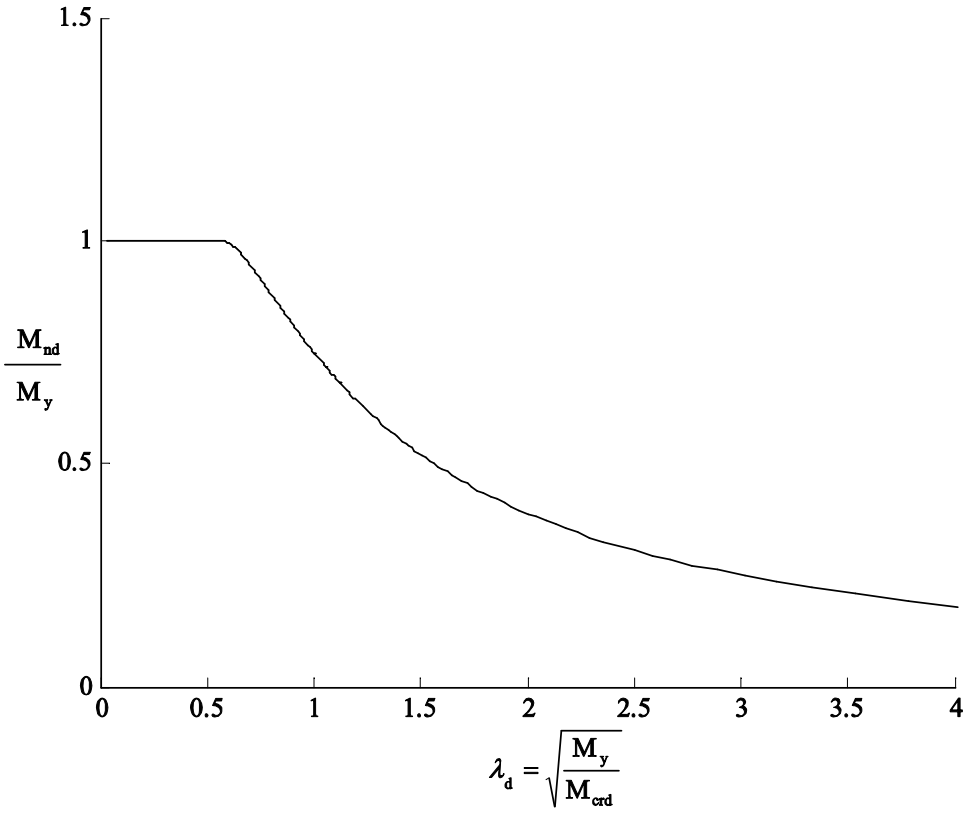

Figure 1.10. Distortional buckling design curve

To calculate the section modulus of the cross-section, the effective width of each compression element can be estimated as follow:

$$\lambda \leq 0.673\,, \qquad b = w \tag{1.2}$$

$$\lambda > 0.673\,, \qquad b = \rho w \tag{1.3}$$

where w is the flat width of the plate as shown in Figure 1.7 and ρ is the local reduction factor defined as

$$\rho = (1 - 0.22/\lambda)/\lambda \leq 1 \tag{1.4}$$

In addition, λ, the plate slenderness factor is defined as

$$\lambda = \sqrt{\frac{f}{f_{cr}}} \tag{1.5}$$

where f is the stress in the compression element and f_{cr}, the plate critical buckling stress is

$$f_{cr} = k\frac{\pi^2 E}{12(1-\mu^2)}\left(\frac{t}{w}\right)^2 \tag{1.6}$$

where k represents the plate buckling coefficient, t symbolizes the thickness of the element, E denotes the modulus of elasticity of the cross-section and μ represents the Poisson's ratio of steel.

1.2.2 AISI Direct Strength Method (DSM)

The AISI Direct Strength Method (DSM) was introduced in 2004 and uses the elastic buckling properties of the entire cross-section to calculate the capacity (Schafer 2002). The advantages of this method can be seen in the design of members with complex cross-sections, for example intermediate and edge stiffeners, where the calculations based upon the effective width method would be cumbersome and time consuming.

The elastic buckling mode shapes pertinent to design can be obtained from an elastic buckling curve generated with a finite strip analysis (Cheung 1998). Buckling modes assumed to control capacity are local buckling, distortional buckling and global buckling (lateral-torsional buckling in the beams). A schematic view of an elastic buckling curve generated employing CUFSM, a freely available program (Schafer and Adány 2006), and the associated buckling modes are presented in Figure 1.11.

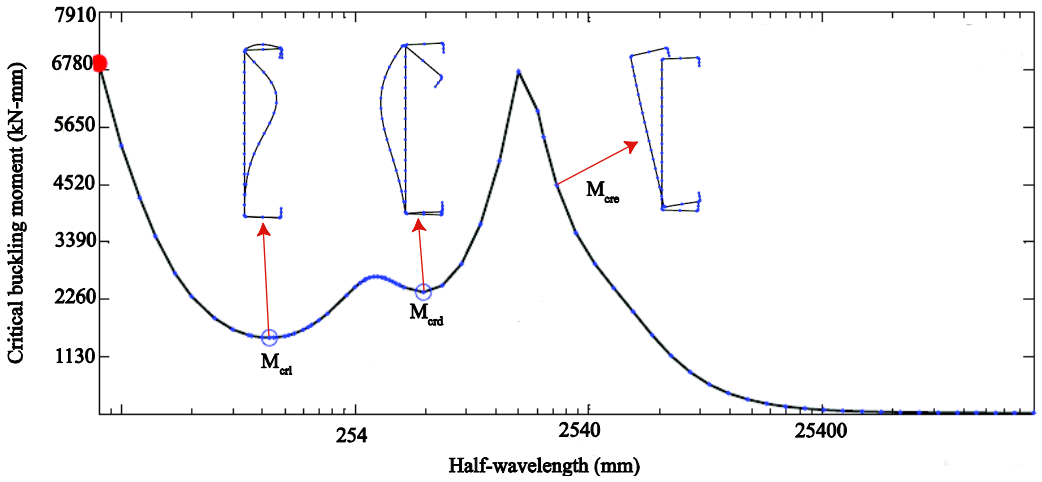

Figure 1.11. Elastic buckling curve for a cold-formed steel beam

The elastic buckling values corresponding to the buckling mode shapes are used in combination with the DSM equations to estimate the strength of the cold-formed steel members. The formulas used to calculate the strength of flexural members as well as the DSM design curves for lateral-torsional, local and distortional buckling modes are provided in AISI specifications and are summarized in Figure 1.12 through Figure 1.14. The horizontal axis in the design curves represents slenderness while the vertical axis represents capacity.

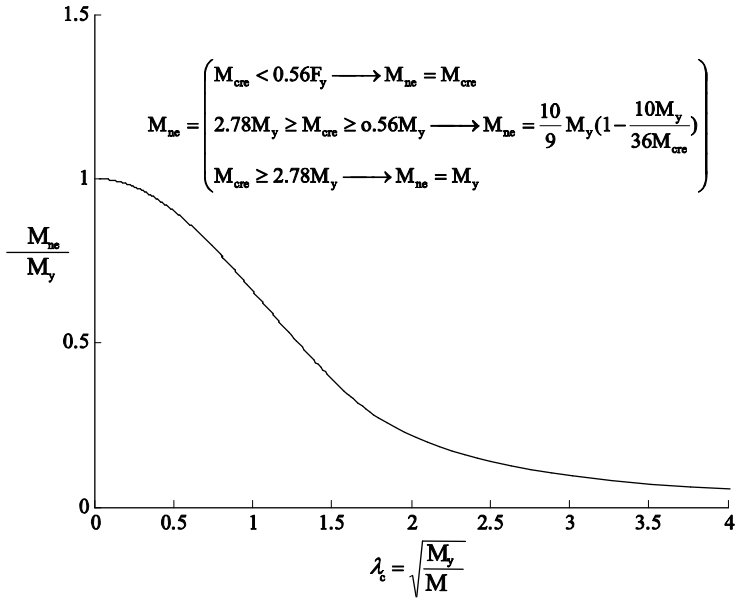

Figure 1.12. DSM lateral-torsional buckling design curve

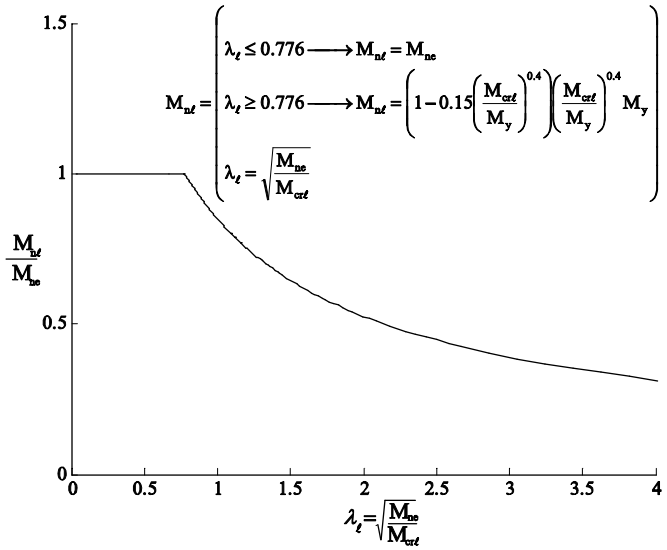

Figure 1.13. DSM local buckling design curve

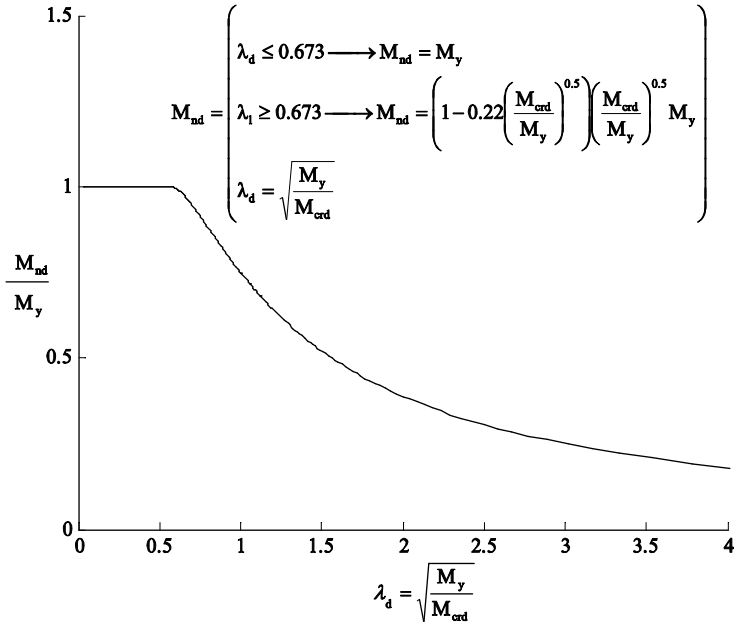

Figure 1.14. DSM distortional buckling design curve

According to the AISI specification, the DSM is only applicable to unperforated members. Modifications to DSM equations for cold-formed steel beams with web-holes have been proposed (Moen 2008). The local buckling capacity of the beam is limited by imposing an

upper bound equal to the strength of the net section. A transition is employed in the distortional buckling equations to capture the effects of net-section yielding more accurately as shown in Figure 1.15.

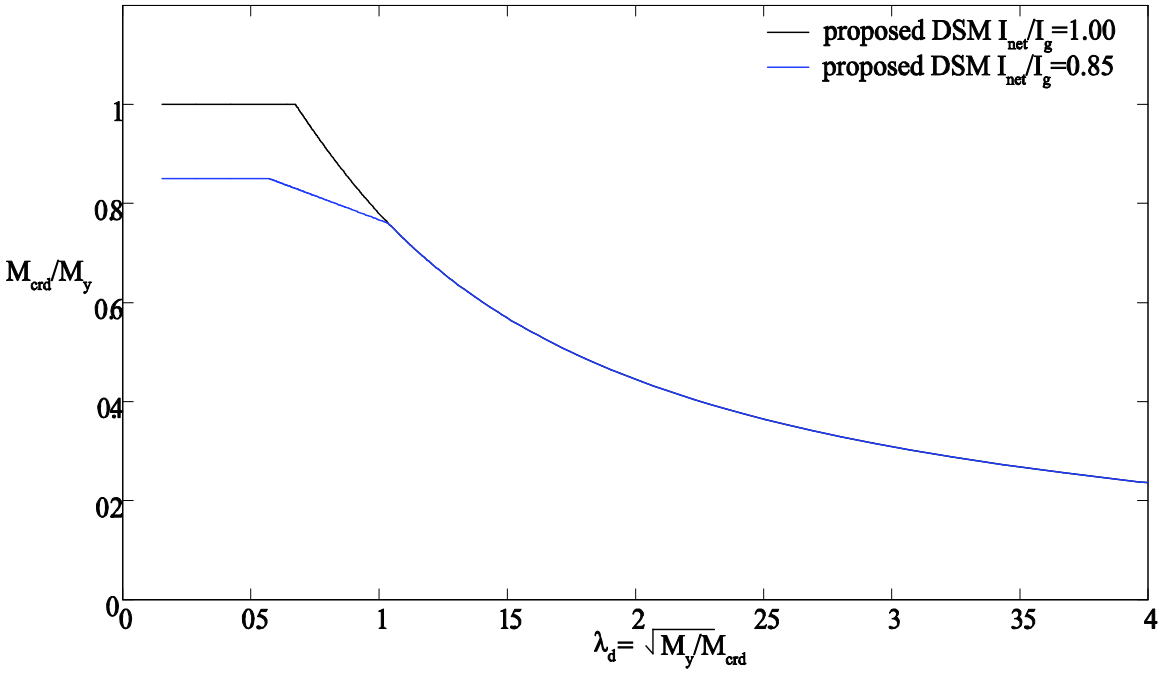

Figure 1.15. Modification in DSM distortional buckling curves

1.3 Research motivation and plan

This research is aimed at studying and quantifying the effects of web holes on the capacity of cold-formed steel beams and validation of modified DSM equations for holes.

Chapter 2 focuses on the specimen specifications and the test set up. The beams cross-section was varied throughout the tests to explore the influence of holes on local, distortional, and global bucking failure modes. Hole depth was varied in the tests to identify trends in ultimate strength. The specimen details such as cross-section and web-hole dimensions, measurement techniques, specimen configuration and the experiment results are presented.

Chapter 3 examines the elastic buckling of cold-formed steel beams with holes. Thin shell finite element eigen-buckling analysis of each joist specimen, including measured cross-section dimensions and tested boundary and loading conditions, were conducted in parallel with the experiments to identify those elastic buckling mode shapes which influence load-deformation response. Description of the modeling process and model specification such as element type, element aspect ratio, material characteristics, load and boundary conditions applied and the choice of eigen-solver employed are provided. The specific critical buckling moments ($M_{cr\ell}$, M_{crd} and M_{cre}) are identified and the influence of web holes on elastic buckling behavior is quantified.

Chapter 4 is focused on the experiments that were conducted during the course of this research. Sixty-eight C-section cold-formed steel joists with unstiffened rectangular web holes were tested to failure. The tested capacity of the beams are provided and the influence of web holes are discussed.

Chapter 5 employs the finite element results from Chapter 3 in conjunction with the modified DSM equations developed (Moen 2008) to estimate the capacity of the pre-punched cold-formed steel beams. The calculated capacities are compared with the experiment results from Chapter 4 to examine the validity of the proposed DSM equations. Conclusions are drawn regarding the influence of initial specimen imperfections and the hole size on the lateral-torsional buckling modes of the beams and the prediction accuracy of DSM for beams with holes.

Chapter 2. Experimental program

The ultimate strength of 68 perforated cold-formed steel lipped C-section beams with slotted web-holes were determined where each specimen was tested under four-point bending to failure as shown in Figure 2.1. Cross sections were selected to explore the local, distortional and lateral-torsional buckling controlled failures. The hole dimensions were determined to provide I_{net}/I_gratio ranging from 0.85 to 1.0 (no hole) where I_{net} and I_g are the net and gross strong axis moment of inertia of the cross-section respectively.

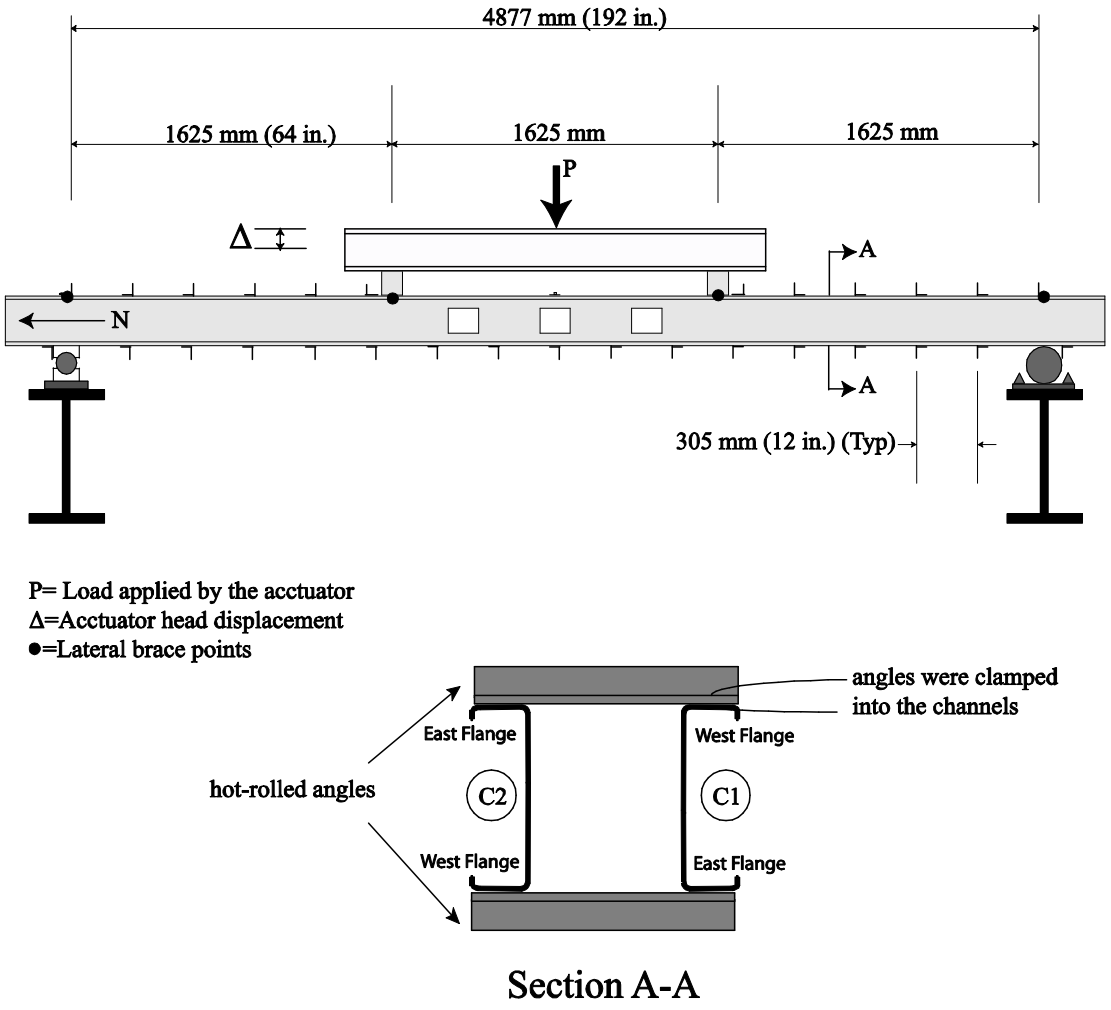

Figure 2.1. Cold formed steel beams are tested under four-point bending configuration

2.1 Cross-section notation and dimensions

Three Structural Stud Manufacturers Association (SSMA) cross-section types were evaluated in this study: SSMA 800S200-33, SSMA 1000S162-54 and SSMA 1200S162-97 (SSMA 2001). Due to damage during delivery, six beams of the 800S200-33 type were replaced with SSMA 800S200-43 beams, which introduced the fourth cross-section category. Each beam was labeled as shown in Figure 2.2. The first set of numbers represent the nominal joist depth, the second set of numbers represents the nominal flange width and the third set of numbers represents the nominal base metal thickness. The test matrix is provided in Table 2.1.

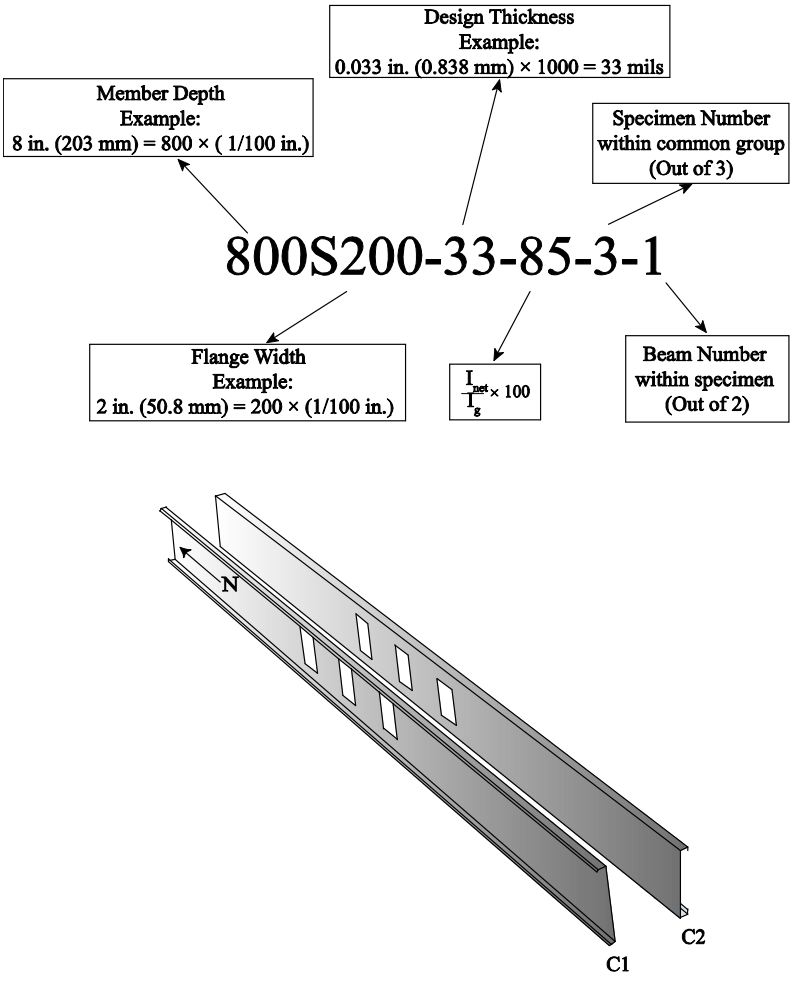

Figure 2.2. Cross-section notation

Table 2.1. Test matrix

cross-section		800S200-33		800S200-43		1000S162-54		1200S162-97	
I_{net}/I_g ratio	Specimen Number	No Holes	Holes	No Holes	Holes	No Holes	Holes	No Holes	Holes
I_{net}/I_g=1.00	1	800 S 200-33-100-1-1	-	-	-	1000 S 162-54-100-1-1	-	1200 S 162-97-100-1-1	-
		800 S 200-33-100-1-2				1000 S 162-54-100-1-2		1200 S 162-97-100-1-2	
	2	800 S 200-33-100-2-1				1000 S 162-54-100-2-1		1200 S 162-97-100-2-1	
		800 S 200-33-100-2-2				1000 S 162-54-100-2-2		1200 S 162-97-100-2-2	
	3	-				1000 S 162-54-100-3-1		1200 S 162-97-100-3-1	
						1000 S 162-54-100-3-2		1200 S 162-97-100-3-2	
I_{net}/I_g=0.95	1	-	800 S 200-33-95-1-1	-	800 S 200-43-95-3-1	-	1000 S 162-54-95-1-1	-	1200 S 162-97-95-1-1
			800 S 200-33-95-1-2		800 S 200-43-95-3-2		1000 S 162-54-95-1-2		1200 S 162-97-95-1-2
	2		800 S 200-33-95-2-1		-		1000 S 162-54-95-2-1		1200 S 162-97-95-2-1
			800 S 200-33-95-2-2				1000 S 162-54-95-2-2		1200 S 162-97-95-2-2
	3		800 S 200-33-90-1-1				1000 S 162-54-95-3-1		1200 S 162-97-95-3-1
			800 S 200-33-90-1-2				1000 S 162-54-95-3-2		1200 S 162-97-95-3-2
I_{net}/I_g=0.90	1	-	800 S 200-33-90-2-1	-	800 S 200-43-90-3-1	-	1000 S 162-54-90-1-1	-	1200 S 162-97-90-1-1
			800 S 200-33-90-2-2		800 S 200-43-90-3-2		1000 S 162-54-90-1-2		1200 S 162-97-90-1-2
	2		800 S 200-33-85-1-1		-		1000 S 162-54-90-2-1		1200 S 162-97-90-2-1
			800 S 200-33-85-1-2				1000 S 162-54-90-2-2		1200 S 162-97-90-2-2
	3		800 S 200-33-85-2-1				1000 S 162-54-90-3-1		1200 S 162-97-90-3-1
			800 S 200-33-85-2-2				1000 S 162-54-90-3-2		1200 S 162-97-90-3-2
I_{net}/I_g=0.85	1	-	-	-	800 S 200-43-85-3-1	-	1000 S 162-54-85-1-1	-	1200 S 162-97-85-1-1
					800 S 200-43-85-3-2		1000 S 162-54-85-1-2		1200 S 162-97-85-1-2
	2				-		1000 S 162-54-85-2-1		1200 S 162-97-85-2-1
							1000 S 162-54-85-2-2		1200 S 162-97-85-2-2
	3						1000 S 162-54-85-3-1		1200 S 162-97-85-3-1
							1000 S 162-54-85-3-2		1200 S 162-97-85-3-2

2.2 Cross-section measurements

The cross-section dimensions shown in Figure 2.3 were measured at the longitudinal mid length of each beam specimen. A digital level, digital calipers, reference steel plates and a radius gauge with 0.79 mm (0.03 in.) increments were used in the measurement process described in Figure 2.4 and Figure 2.5. Measured dimensions are provided in Table 2.2 through Table 2.5. The cross-section dimensions are measured out-to-out.

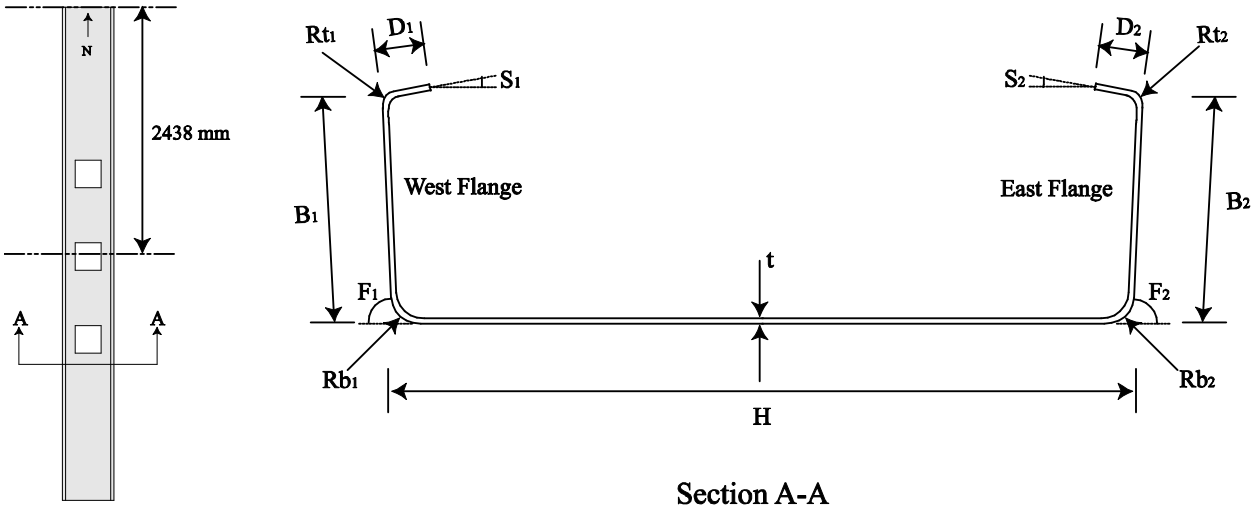

Figure 2.3. Measured cross-section dimensions

Clamp the steel plate to the flange. Using a digital caliper measure the distance between the outer face of the plate and the edge of the lip stiffener. Calculate the width of the lip stiffener by subtracting the width of the plate from the caliper measurment.

Clamp the steel plates to both flanges. Using a set of digital caliper measure the distance between the inner face of the two plates.

Clamp the steel plates to the lip-stiffener and the web. Using the extension on the digital caliper measure the distance between the inner face of the plate attached to the web and the outside of the plate attached to the lip. Subtract the thickness of the plate attached to the lip in order to find the width of the flange.

Figure 2.4 Cross-section measurment procedure (out-to-out dimensions)

Clamp the steel plate to the flange. Make sure the extension of the plate is touching the channel. Use a digital-level to find the angle between the flange and the web. (Note: the channel should be placed on a flat surface with zero initial angle before the measurements).

Clamp the steel plate to the lip-stiffener. Make sure the extension of the plate is touching the channel. Use a digital-level to find the angle between the flange and the lip-stiffener. (Note: the channel should be placed on a flat surface with zero initial

Figure 2.5 Cross-section measurments (flange and lip angles)

Table 2.2 Cross-section dimensions for 800S200-33 beams

800S200-33													
Section	H (mm)	B_1 (mm)	B_2 (mm)	D_1 (mm)	D_2 (mm)	F_1 (degrees)	F_2 (degrees)	S_1 (degrees)	S_2 (degrees)	Rb_1 (mm)	Rb_2 (mm)	Rt_1 (mm)	Rt_2 (mm)
800 S 200-33-100-1-1	203.38	49.05	47.83	11.71	11.66	87.7	88.3	1.8	2.1	3.57	3.57	4.37	3.57
800 S 200-33-100-1-2	203.61	49.00	47.83	11.66	11.51	89.1	89.7	2.7	3.1	3.18	3.57	4.37	3.18
800 S 200-33-100-2-1	203.61	48.77	47.65	11.53	11.13	84.8	83.6	0.9	6.2	3.57	2.78	2.78	3.18
800 S 200-33-100-2-2	203.53	49.17	47.65	11.86	11.18	86.5	90.1	2.2	2.8	3.18	3.57	4.37	3.57
800 S 200-33-95-1-1	204.62	48.16	48.95	11.84	12.22	88.4	85.4	3.1	2.6	3.57	3.57	4.37	3.57
800 S 200-33-95-1-2	203.96	49.12	47.57	11.35	11.79	88.5	84.3	4.2	5.6	3.57	2.78	3.97	3.18
800 S 200-33-95-2-1	203.86	48.90	47.45	11.56	11.56	88.9	84.3	0.5	2.7	3.57	3.18	4.37	3.18
800 S 200-33-95-2-2	203.71	49.30	47.22	11.46	11.81	87.7	85.2	-1.8	5.2	3.18	3.18	4.37	3.18
800 S 200-33-90-1-1	204.04	48.92	48.13	11.84	11.38	82.4	83.9	-1.5	6.8	3.57	3.18	4.37	3.18
800 S 200-33-90-1-2	203.86	49.43	47.63	11.61	11.63	85.0	88.1	4.2	4.5	3.57	3.18	4.37	3.18
800 S 200-33-90-2-1	203.84	48.84	47.96	11.84	11.40	87.8	85.1	0.9	6.1	3.57	3.18	4.37	3.57
800 S 200-33-90-2-2	203.89	48.82	47.65	11.63	11.66	87.6	89.2	4.7	3.5	3.57	2.78	3.57	3.18
800 S 200-33-85-1-1	203.40	49.10	47.73	11.66	11.76	88.9	89.3	2.4	1.7	3.57	3.18	4.37	3.18
800 S 200-33-85-1-2	203.56	49.33	47.57	11.63	11.46	87.6	88.9	3.4	2.8	3.57	3.18	4.37	3.18
800 S 200-33-85-2-1	203.38	48.79	47.73	11.79	11.61	89.6	87.3	5.2	3.3	3.57	3.18	4.37	3.18
800 S 200-33-85-2-2	203.48	49.05	47.65	11.79	11.99	87.3	89.6	3.1	2.6	3.97	3.57	3.57	3.18

Table 2.3 Cross-section dimensions for 800S200-43 beams

800S200-43													
Section	H (mm)	B_1 (mm)	B_2 (mm)	D_1 (mm)	D_2 (mm)	F_1 (degrees)	F_2 (degrees)	S_1 (degrees)	S_2 (degrees)	Rb_1 (mm)	Rb_2 (mm)	Rt_1 (mm)	Rt_2 (mm)
800 S 200-33-95-1-1	204.83	49.02	49.12	12.34	11.56	88.4	84.9	-4.6	-0.8	3.57	3.18	3.57	3.18
800 S 200-33-95-1-2	204.62	48.72	48.87	12.17	11.58	87.6	85.7	-3.8	-1.2	3.57	3.18	3.97	3.57
800 S 200-33-90-1-1	204.75	49.05	49.02	12.14	11.58	88.6	87.0	-3.9	-1.1	3.57	3.18	3.57	3.57
800 S 200-33-90-1-2	204.83	49.53	48.21	12.47	11.43	88.9	87.7	-4.1	-0.7	3.57	3.18	3.57	3.57
800 S 200-33-85-1-1	204.72	49.30	48.69	12.62	11.15	88.4	88.1	-1.4	4.1	3.18	3.57	4.37	3.57
800 S 200-33-85-1-2	206.68	48.84	48.39	11.13	11.10	87.6	87.1	2.5	3.4	3.18	3.57	4.37	3.18

Table 2.4 Cross-section dimensions for 1000S162-54 beams

1000S162-54													
Section	H (mm)	B_1 (mm)	B_2 (mm)	D_1 (mm)	D_2 (mm)	F_1 (degrees)	F_2 (degrees)	S_1 (degrees)	S_2 (degrees)	Rb_1 (mm)	Rb_2 (mm)	Rt_1 (mm)	Rt_2 (mm)
1000 S 162-54-100-1-1	255.30	41.43	38.33	11.25	10.24	86.6	87.1	-3.5	3.3	4.37	3.97	3.57	3.57
1000 S 162-54-100-1-2	255.12	41.43	38.46	11.20	10.29	86.6	87.5	-4.5	3.7	4.37	3.97	3.57	3.57
1000 S 162-54-100-2-1	255.32	40.97	38.99	11.13	10.39	88.0	87.0	-1.5	-0.5	4.37	3.97	3.57	3.57
1000 S 162-54-100-2-2	255.14	41.00	38.10	11.38	9.93	87.5	87.2	-1.2	4.1	4.37	3.97	4.37	3.57
1000 S 162-54-100-3-1	255.37	41.71	38.07	11.40	10.39	88.5	87.5	-3.0	2.6	4.37	3.97	3.57	3.57
1000 S 162-54-100-3-2	255.14	41.28	38.23	11.25	10.01	87.8	87.0	-3.8	4.2	4.37	3.97	3.57	3.57
1000 S 162-54-95-1-1	255.24	41.05	38.51	11.13	10.03	87.6	87.5	-2.4	2.1	4.37	3.97	3.57	3.57
1000 S 162-54-95-1-2	255.32	41.17	38.58	11.07	10.19	87.4	87.6	-2.1	2.2	4.37	3.97	3.57	3.57
1000 S 162-54-95-2-1	255.42	41.25	38.61	10.95	10.11	87.9	87.4	-2.2	2.5	4.37	3.97	3.57	3.57
1000 S 162-54-95-2-2	255.32	41.02	38.38	10.95	10.13	87.7	87.6	2.1	2.4	3.57	3.97	3.57	3.57
1000 S 162-54-95-3-1	255.45	41.17	38.63	11.23	10.19	88.1	87.8	2.6	3.1	3.57	3.97	3.57	3.57
1000 S 162-54-95-3-2	255.40	41.10	38.53	10.90	10.19	87.1	88.2	-3.1	1.6	3.57	3.97	3.57	3.57
1000 S 162-54-90-1-1	255.07	40.89	38.40	11.43	9.98	87.9	86.9	-1.6	1.5	4.37	3.57	3.57	3.57
1000 S 162-54-90-1-2	255.27	40.94	38.79	10.29	11.25	86.9	87.5	0.5	-3.7	4.37	3.97	3.57	3.57
1000 S 162-54-90-2-1	255.27	41.05	38.33	11.15	10.31	88.6	87.2	3.2	3.0	4.37	3.97	3.57	3.57
1000 S 162-54-90-2-2	255.22	41.10	38.84	11.28	10.08	88.2	86.8	-2.4	3.2	4.37	3.97	3.57	3.57
1000 S 162-54-90-3-1	255.30	41.55	38.89	11.46	10.01	87.7	86.6	3.1	3.0	4.37	3.97	3.97	3.57
1000 S 162-54-90-3-2	255.12	41.68	39.29	11.35	9.88	87.1	86.2	-3.4	0.9	4.37	3.97	3.57	3.57
1000 S 162-54-85-1-1	255.24	41.05	38.20	11.13	10.13	88.3	87.5	-3.2	2.3	4.37	3.97	3.57	3.57
1000 S 162-54-85-1-2	255.24	41.05	38.20	11.13	10.13	86.5	86.8	-4.6	5.2	4.76	3.57	3.57	3.57
1000 S 162-54-85-2-1	255.35	41.53	39.12	11.30	10.24	87.8	86.4	-1.9	-0.7	4.37	3.97	3.57	3.57
1000 S 162-54-85-2-2	255.14	41.45	38.38	10.85	11.51	88.0	86.7	-3.6	3.8	4.37	3.97	3.57	3.57
1000 S 162-54-85-3-1	255.04	41.68	38.23	11.28	10.16	87.7	87.1	-4.3	4.1	4.37	3.97	3.57	3.57
1000 S 162-54-85-3-2	255.40	41.63	38.05	11.40	10.21	87.3	86.6	-4.4	3.8	4.37	3.97	3.57	3.57

Table 2.5 Cross-section dimensions for 1200S162-97 beams

1200S162-97													
Section	H (mm)	B_1 (mm)	B_2 (mm)	D_1 (mm)	D_2 (mm)	F_1 (degrees)	F_2 (degrees)	S_1 (degrees)	S_2 (degrees)	Rb_1 (mm)	Rb_2 (mm)	Rt_1 (mm)	Rt_2 (mm)
1200 S 162-68-100-1-1	305.28	42.19	40.34	11.51	12.01	88.4	83.6	-6.2	1.0	5.16	5.16	5.56	5.95
1200 S 162-68-100-1-2	305.23	42.04	40.61	11.20	12.50	88.6	84.6	-5.6	0.5	5.16	5.16	5.56	5.56
1200 S 162-68-100-2-1	305.26	42.29	40.21	10.26	12.12	86.5	85.5	-7.8	4.2	5.16	5.16	5.56	5.95
1200 S 162-68-100-2-2	298.02	42.04	41.94	11.53	11.84	87.3	85.3	-5.1	-1.5	5.56	5.56	5.56	5.56
1200 S 162-68-100-3-1	305.10	42.90	40.87	10.85	12.27	87.1	85.3	-4.0	5.5	5.16	5.16	5.56	5.95
1200 S 162-68-100-3-2	301.47	41.73	43.61	10.92	11.96	87.2	85.7	-5.7	0.1	5.16	4.76	5.56	5.95
1200 S 162-68-95-1-1	305.13	43.05	41.55	12.42	12.83	86.5	84.5	-4.7	4.2	5.16	4.76	5.56	5.95
1200 S 162-68-95-1-2	305.21	42.34	42.01	12.47	12.50	84.7	86.3	-3.7	3.1	5.16	4.76	5.56	5.95
1200 S 162-68-95-2-1	305.59	42.42	43.51	12.83	11.38	88.6	83.6	-6.3	2.4	5.16	4.76	5.56	5.95
1200 S 162-68-95-2-2	305.36	42.14	43.08	11.66	10.29	89.3	87.8	-6.7	1.5	5.16	4.76	5.56	5.95
1200 S 162-68-95-3-1	305.97	42.55	41.53	12.50	10.59	86.9	89.3	-4.3	3.4	5.16	4.76	5.56	5.95
1200 S 162-68-95-3-2	305.28	42.77	42.19	12.83	12.65	88.4	84.6	-4.7	2.3	5.16	4.76	5.56	5.95
1200 S 162-68-90-1-1	305.18	42.85	40.59	12.17	11.25	86.0	83.1	-9.1	0.9	5.16	5.16	5.56	5.56
1200 S 162-68-90-1-2	305.33	42.27	40.84	11.28	12.29	87.6	82.3	-5.5	-2.2	5.16	5.16	5.16	5.56
1200 S 162-68-90-2-1	305.44	42.62	40.59	11.58	11.96	88.3	83.6	-7.6	1.9	4.76	4.76	6.35	5.56
1200 S 162-68-90-2-2	305.08	41.50	40.94	11.51	11.30	88.7	84.3	-4.2	-2.6	4.76	4.76	5.16	5.16
1200 S 162-68-90-3-1	305.10	42.09	40.77	11.02	12.01	87.7	84.6	-4.4	2.0	4.76	5.16	5.56	5.95
1200 S 162-68-90-3-2	304.80	41.78	40.13	11.13	12.09	87.7	84.8	-4.0	2.4	5.16	4.76	5.56	5.95
1200 S 162-68-85-1-1	305.08	41.94	40.77	11.23	11.96	87.5	85.8	-5.8	3.2	5.16	4.76	5.56	5.95
1200 S 162-68-85-1-2	305.49	44.32	40.46	11.51	11.13	88.6	85.9	-4.8	2.6	5.16	4.76	5.56	5.95
1200 S 162-68-85-2-1	305.61	41.35	42.70	11.35	11.76	87.5	86.4	-6.2	3.7	5.16	4.76	5.56	5.95
1200 S 162-68-85-2-2	304.98	40.69	42.11	10.87	12.83	88.3	85.2	-5.3	0.8	5.16	4.76	5.56	5.95
1200 S 162-68-85-3-1	305.18	41.86	41.76	11.53	12.47	87.9	87.3	-6.4	2.2	5.16	4.76	5.56	5.95
1200 S 162-68-85-3-2	305.05	42.04	42.16	11.40	11.10	87.6	88.5	-5.3	3.2	5.16	4.76	5.56	5.95

2.2.1 Specimen thickness

The cold-formed steel members used in this study were zinc-coated by the manufacturer, to provide galvanic corrosion protection. The thickness of the base metal and the thickness of the zinc coating on each side of steel sheet (see Figure 2.6) were measured from tensile coupons cut from the east flange, west flange and the web of each cross-section (Figure 2.3).

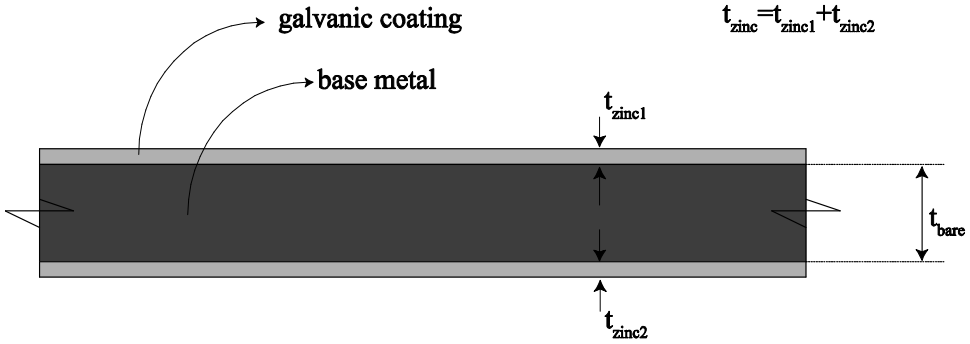

Figure 2.6. Base metal and galvanic coating

The galvanic coating was removed employing hydrochloric acid (ASTM 2009). Figure 2.7 shows the galvanic-coating removal process, which is fully described in Bowen (2009). The base steel sheet and the zinc coating thickness measured for each specimen at east flange (EF), west flange (WF) and the web (S) are presented in Table 2.6 through Table 2.9.

Figure 2.7. The zinc stripping process described in ASTM A90 – 07: (a) the reaction between the acid and the galvanic coating, (b) the coating has been removed exposing the base metal

Table 2.6 Base metal and zinc coating thicknesses of 800S200-33 beams

Name	t_{bare}	t_{zinc}	Name	t_{bare}	t_{zinc}	Name	t_{bare}	t_{zinc}	Name	t_{bare}	t_{zinc}
	mm	mm		mm	mm		mm	mm		mm	mm
800S200-33-100-1-1-EF	0.821	0.054	800S200-33-95-1-1-EF	0.815	0.046	800S200-33-90-1-1-EF	0.808	0.047	800S200-33-85-1-1-EF	0.814	0.040
800S200-33-100-1-1-S	0.824	0.043	800S200-33-95-1-1-S	0.818	0.036	800S200-33-90-1-1-S	0.812	0.044	800S200-33-85-1-1-S	0.817	0.046
800S200-33-100-1-1-WF	0.841	0.037	800S200-33-95-1-1-WF	0.825	0.038	800S200-33-90-1-1-WF	0.824	0.044	800S200-33-85-1-1-WF	0.827	0.059
800S200-33-100-1-2-EF	0.822	0.076	800S200-33-95-1-2-EF	0.826	0.040	800S200-33-90-1-2-EF	0.822	0.049	800S200-33-85-1-2-EF	0.820	0.042
800S200-33-100-1-2-S	0.827	0.043	800S200-33-95-1-2-S	0.830	0.056	800S200-33-90-1-2-S	0.828	0.047	800S200-33-85-1-2-S	0.823	0.063
800S200-33-100-1-2-WF	0.839	0.049	800S200-33-95-1-2-WF	0.838	0.044	800S200-33-90-1-2-WF	0.835	0.042	800S200-33-85-1-2-WF	0.828	0.049
800S200-33-100-2-1-EF	0.816	0.043	800S200-33-95-2-1-EF	0.821	0.032	800S200-33-90-2-1-EF	0.824	0.066	800S200-33-85-2-1-EF	0.829	0.041
800S200-33-100-2-1-S	0.820	0.085	800S200-33-95-2-1-S	0.825	0.035	800S200-33-90-2-1-S	0.830	0.040	800S200-33-85-2-1-S	0.831	0.049
800S200-33-100-2-1-WF	0.833	0.033	800S200-33-95-2-1-WF	0.833	0.040	800S200-33-90-2-1-WF	0.845	0.037	800S200-33-85-2-1-WF	0.839	0.052
800S200-33-100-2-2-EF	0.823	0.046	800S200-33-95-2-2-EF	0.816	0.029	800S200-33-90-2-2-EF	0.812	0.050	800S200-33-85-2-2-EF	0.812	0.045
800S200-33-100-2-2-S	0.827	0.043	800S200-33-95-2-2-S	0.820	0.042	800S200-33-90-2-2-S	0.817	0.046	800S200-33-85-2-2-S	0.813	0.044
800S200-33-100-2-2-WF	0.834	0.044	800S200-33-95-2-2-WF	0.829	0.029	800S200-33-90-2-2-WF	0.820	0.043	800S200-33-85-2-2-WF	0.829	0.040

Table 2.7 Base metal and zinc coating thicknesses of 800S200-43 beams

Name	t_{bare}	t_{zinc}	Name	t_{bare}	t_{zinc}	Name	t_{bare}	t_{zinc}	Name	t_{bare}	t_{zinc}
	mm	mm		mm	mm		mm	mm		mm	mm
800S200-43-100-1-1-EF	1.099	0.051	800S200-43-95-1-1-EF	1.095	0.035	800S200-43-90-1-1-EF	1.095	0.043	800S200-43-85-1-1-EF	1.089	0.051
800S200-43-100-1-1-S	1.099	0.041	800S200-43-95-1-1-S	1.090	0.037	800S200-43-90-1-1-S	1.093	0.051	800S200-43-85-1-1-S	1.090	0.054
800S200-43-100-1-1-WF	1.106	0.056	800S200-43-95-1-1-WF	1.099	0.028	800S200-43-90-1-1-WF	1.111	0.045	800S200-43-85-1-1-WF	1.105	0.030
800S200-43-100-1-2-EF	1.090	0.045	800S200-43-95-1-2-EF	1.095	0.045	800S200-43-90-1-2-EF	1.107	0.030	800S200-43-85-1-2-EF	1.104	0.044
800S200-43-100-1-2-S	1.088	0.056	800S200-43-95-1-2-S	1.093	0.045	800S200-43-90-1-2-S	1.096	0.044	800S200-43-85-1-2-S	1.106	0.045
800S200-43-100-1-2-WF	1.106	0.029	800S200-43-95-1-2-WF	1.102	0.044	800S200-43-90-1-2-WF	1.105	0.038	800S200-43-85-1-2-WF	1.131	0.031

Table 2.8 Base metal and zinc coating thicknesses of 1000S162-54 beams

Name	t_{bare}	t_{zinc}	Name	t_{bare}	t_{zinc}	Name	t_{bare}	t_{zinc}	Name	t_{bare}	t_{zinc}
	mm	mm		mm	mm		mm	mm		mm	mm
1000S162-54-100-1-1-EF	1.349	0.060	1000S162-54-95-1-1-EF	1.349	0.071	1000S162-54-90-1-1-EF	1.345	0.053	1000S162-54-85-1-1-EF	1.347	0.056
1000S162-54-100-1-1-S	1.340	0.054	1000S162-54-95-1-1-S	1.341	0.051	1000S162-54-90-1-1-S	1.338	0.041	1000S162-54-85-1-1-S	1.343	0.059
1000S162-54-100-1-1-WF	1.327	0.061	1000S162-54-95-1-1-WF	1.323	0.061	1000S162-54-90-1-1-WF	1.318	0.061	1000S162-54-85-1-1-WF	1.323	0.083
1000S162-54-100-1-2-EF	1.345	0.058	1000S162-54-95-1-2-EF	1.346	0.068	1000S162-54-90-1-2-EF	1.338	0.058	1000S162-54-85-1-2-EF	1.353	0.071
1000S162-54-100-1-2-S	1.336	0.043	1000S162-54-95-1-2-S	1.339	0.057	1000S162-54-90-1-2-S	1.330	0.044	1000S162-54-85-1-2-S	1.346	0.055
1000S162-54-100-1-2-WF	1.319	0.052	1000S162-54-95-1-2-WF	1.328	0.061	1000S162-54-90-1-2-WF	1.312	0.054	1000S162-54-85-1-2-WF	1.328	0.065
1000S162-54-100-2-1-EF	1.336	0.061	1000S162-54-95-2-1-EF	1.346	0.068	1000S162-54-90-2-1-EF	1.363	0.070	1000S162-54-85-2-1-EF	1.348	0.081
1000S162-54-100-2-1-S	1.328	0.066	1000S162-54-95-2-1-S	1.339	0.052	1000S162-54-90-2-1-S	1.350	0.062	1000S162-54-85-2-1-S	1.343	0.054
1000S162-54-100-2-1-WF	1.311	0.057	1000S162-54-95-2-1-WF	1.325	0.067	1000S162-54-90-2-1-WF	1.329	0.071	1000S162-54-85-2-1-WF	1.320	0.066
1000S162-54-100-2-2-EF	1.343	0.071	1000S162-54-95-2-2-EF	1.339	0.059	1000S162-54-90-2-2-EF	1.353	0.070	1000S162-54-85-2-2-EF	1.347	0.077
1000S162-54-100-2-2-S	1.332	0.054	1000S162-54-95-2-2-S	1.331	0.055	1000S162-54-90-2-2-S	1.340	0.056	1000S162-54-85-2-2-S	1.338	0.063
1000S162-54-100-2-2-WF	1.315	0.061	1000S162-54-95-2-2-WF	1.315	0.064	1000S162-54-90-2-2-WF	1.319	0.080	1000S162-54-85-2-2-WF	1.318	0.070
1000S162-54-100-3-1-EF	1.347	0.062	1000S162-54-95-3-1-EF	1.348	0.061	1000S162-54-90-3-1-EF	1.354	0.072	1000S162-54-85-3-1-EF	1.348	0.088
1000S162-54-100-3-1-S	1.339	0.053	1000S162-54-95-3-1-S	1.337	0.061	1000S162-54-90-3-1-S	1.343	0.064	1000S162-54-85-3-1-S	1.342	0.066
1000S162-54-100-3-1-WF	1.318	0.062	1000S162-54-95-3-1-WF	1.326	0.054	1000S162-54-90-3-1-WF	1.327	0.088	1000S162-54-85-3-1-WF	1.325	0.077
1000S162-54-100-3-2-EF	1.347	0.053	1000S162-54-95-3-2-EF	1.347	0.055	1000S162-54-90-3-2-EF	1.356	0.069	1000S162-54-85-3-2-EF	1.354	0.056
1000S162-54-100-3-2-S	1.335	0.045	1000S162-54-95-3-2-S	1.334	0.051	1000S162-54-90-3-2-S	1.345	0.063	1000S162-54-85-3-2-S	1.347	0.055
1000S162-54-100-3-2-WF	1.313	0.062	1000S162-54-95-3-2-WF	1.318	0.058	1000S162-54-90-3-2-WF	1.326	0.076	1000S162-54-85-3-2-WF	1.326	0.105

Table 2.9 Base metal and zinc coating thicknesses of 1200S162-97 beams

Name	t_{bare}	t_{zinc}	Name	t_{bare}	t_{zinc}	Name	t_{bare}	t_{zinc}	Name	t_{bare}	t_{zinc}
	mm	mm		mm	mm		mm	mm		mm	mm
1200S162-97-100-1-1-EF	2.552	0.045	1200S162-97-95-1-1-EF	2.536	0.052	1200S162-97-90-1-1-EF	2.555	0.038	1200S162-97-85-1-1-EF	2.540	0.054
1200S162-97-100-1-1-S	2.556	0.059	1200S162-97-95-1-1-S	2.542	0.061	1200S162-97-90-1-1-S	2.552	0.050	1200S162-97-85-1-1-S	2.548	0.051
1200S162-97-100-1-1-WF	2.555	0.050	1200S162-97-95-1-1-WF	2.542	0.048	1200S162-97-90-1-1-WF	2.548	0.049	1200S162-97-85-1-1-WF	2.541	0.065
1200S162-97-100-1-2-EF	2.552	0.051	1200S162-97-95-1-2-EF	2.532	0.045	1200S162-97-90-1-2-EF	2.557	0.047	1200S162-97-85-1-2-EF	2.556	0.051
1200S162-97-100-1-2-S	2.558	0.057	1200S162-97-95-1-2-S	2.533	0.055	1200S162-97-90-1-2-S	2.559	0.055	1200S162-97-85-1-2-S	2.564	0.052
1200S162-97-100-1-2-WF	2.557	0.054	1200S162-97-95-1-2-WF	2.534	0.054	1200S162-97-90-1-2-WF	2.555	0.050	1200S162-97-85-1-2-WF	2.556	0.048
1200S162-97-100-2-1-EF	2.539	0.055	1200S162-97-95-2-1-EF	2.529	0.047	1200S162-97-90-2-1-EF	2.575	0.051	1200S162-97-85-2-1-EF	2.542	0.046
1200S162-97-100-2-1-S	2.538	0.054	1200S162-97-95-2-1-S	2.532	0.053	1200S162-97-90-2-1-S	2.600	0.034	1200S162-97-85-2-1-S	2.549	0.056
1200S162-97-100-2-1-WF	2.540	0.047	1200S162-97-95-2-1-WF	2.531	0.053	1200S162-97-90-2-1-WF	2.585	0.048	1200S162-97-85-2-1-WF	2.552	0.058
1200S162-97-100-2-2-EF	2.562	0.053	1200S162-97-95-2-2-EF	2.536	0.047	1200S162-97-90-2-2-EF	2.583	0.050	1200S162-97-85-2-2-EF	2.526	0.053
1200S162-97-100-2-2-S	2.565	0.052	1200S162-97-95-2-2-S	2.543	0.047	1200S162-97-90-2-2-S	2.583	0.056	1200S162-97-85-2-2-S	2.531	0.054
1200S162-97-100-2-2-WF	2.561	0.051	1200S162-97-95-2-2-WF	2.543	0.044	1200S162-97-90-2-2-WF	2.581	0.052	1200S162-97-85-2-2-WF	2.535	0.046
1200S162-97-100-3-1-EF	2.524	0.056	1200S162-97-95-3-1-EF	2.550	0.053	1200S162-97-90-3-1-EF	2.554	0.041	1200S162-97-85-3-1-EF	2.564	0.056
1200S162-97-100-3-1-S	2.535	0.050	1200S162-97-95-3-1-S	2.558	0.053	1200S162-97-90-3-1-S	2.557	0.048	1200S162-97-85-3-1-S	2.576	0.048
1200S162-97-100-3-1-WF	2.530	0.059	1200S162-97-95-3-1-WF	2.548	0.055	1200S162-97-90-3-1-WF	2.557	0.043	1200S162-97-85-3-1-WF	2.579	0.042
1200S162-97-100-3-2-EF	2.567	0.046	1200S162-97-95-3-2-EF	2.550	0.053	1200S162-97-90-3-2-EF	2.561	0.054	1200S162-97-85-3-2-EF	2.575	0.040
1200S162-97-100-3-2-S	2.563	0.054	1200S162-97-95-3-2-S	2.554	0.057	1200S162-97-90-3-2-S	2.565	0.047	1200S162-97-85-3-2-S	2.579	0.055
1200S162-97-100-3-2-WF	2.559	0.054	1200S162-97-95-3-2-WF	2.551	0.056	1200S162-97-90-3-2-WF	2.566	0.045	1200S162-97-85-3-2-WF	2.580	0.054

2.3 Pre-punched web-hole dimensions and locations

Three holes were cut into the web of each beam specimen. The first hole was cut at the longitudinal midpoint of the beam and the two other holes were located 457 mm (18 in.) center to center from the first hole as shown in Figure 2.8.

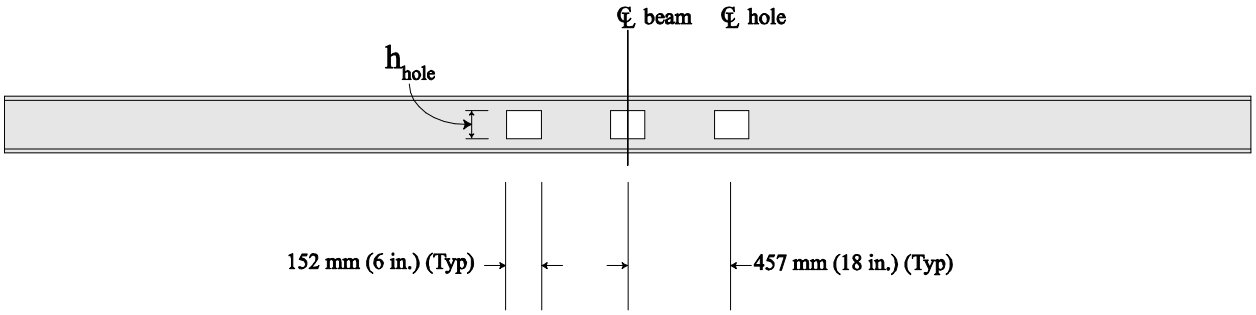

Figure 2.8. Hole dimensions and location

The typical length of a hole, $L_{hole,}$ is 152.4 mm (6 in.). The length of the holes and the distance between the holes were purposely chosen to observe the effects of local buckling in the unstiffened strip above the hole and the gross cross-section between holes. The I_{net}/I_g ratios of 1.00, 0.95, 0.90 and 0.85 were employed as a criterion to determine the depth of the slotted holes (h_{hole}).

Holes were cut into the beam web using water jet cutting technology at Valley Precision company in Waynesboro, Virginia. A computer-controlled water-jet cutting machine was used in the hole cutting procedure. Since there is no heat incorporated with the water-jet cutting approach, mechanical properties of the cross-section are assumed to remain unchanged. Moreover, a higher precision was obtained through this method rather than laser or plasma cutting. The measured hole depths, as well as the relative net and gross moment of inertias are presented in Table 2.10.

Table 2.10 Measured hole size

Beam Name	I_g	I_{net}	I_{net}/I_g	h_{hole}	Beam Name	I_g	I_{net}	I_{net}/I_g	h_{hole}	Beam Name	I_g	I_{net}	I_{net}/I_g	h_{hole}
	mm^4	mm^4		mm		mm^4	mm^4		mm		mm^4	mm^4		mm
800 S 200-33-95-1-1	1544135	1466909	0.95	104.2	1000 S 162-54-95-1-1	3774345	3578400	0.95	119.1	1200 S 162-97-95-1-1	11379809	10798828	0.95	139.1
800 S 200-33-95-1-2	1553334	1475642	0.95	103.9	1000 S 162-54-95-1-2	3785167	3587840	0.95	119.3	1200 S 162-97-95-1-2	11453357	10868988	0.95	138.9
800 S 200-33-95-2-1	1529151	1452692	0.95	103.6	1000 S 162-54-95-2-1	3778341	3582109	0.95	119.2	1200 S 162-97-95-2-1	11457269	10872397	0.95	139.0
800 S 200-33-95-2-2	1522075	1445951	0.95	103.7	1000 S 162-54-95-2-2	3759319	3563625	0.95	119.2	1200 S 162-97-95-2-2	11197874	10625414	0.95	138.0
800 S 200-33-90-2-1	1550629	1395564	0.90	131.9	1000 S 162-54-95-3-1	3797987	3599433	0.95	119.5	1200 S 162-97-95-3-1	11249653	10675936	0.95	138.4
800 S 200-33-90-2-2	1545259	1390722	0.90	130.9	1000 S 162-54-95-3-2	3771057	3575417	0.95	119.3	1200 S 162-97-95-3-2	11460391	10875778	0.95	138.9
800 S 200-33-90-1-1	1549963	1394951	0.90	130.9	1000 S 162-54-90-1-1	3759277	3371741	0.90	150.1	1200 S 162-97-95-1-1	11119165	9985329	0.90	174.0
800 S 200-33-90-1-2	1506466	1355826	0.90	130.3	1000 S 162-54-90-1-2	3751827	3364057	0.90	150.1	1200 S 162-97-95-1-2	11282327	10130318	0.90	173.6
800 S 200-33-85-1-1	1496102	1271700	0.85	148.8	1000 S 162-54-90-2-1	3803564	3405609	0.90	150.0	1200 S 162-97-95-2-1	11200996	10058809	0.90	173.9
800 S 200-33-85-1-2	1510962	1284351	0.85	148.9	1000 S 162-54-90-2-2	3780297	3386581	0.90	150.1	1200 S 162-97-95-2-2	11155918	10016512	0.90	174.1
800 S 200-33-85-2-1	1524781	1296119	0.85	148.9	1000 S 162-54-90-3-1	3817716	3417761	0.90	150.5	1200 S 162-97-95-3-1	11154919	10015007	0.90	173.8
800 S 200-33-85-2-2	1502804	1277358	0.85	149.3	1000 S 162-54-90-3-2	3816051	3416617	0.90	150.4	1200 S 162-97-95-3-2	11008905	9884481	0.90	173.5
800 S 200-43-95-1-1	2065840	1962548	0.95	104.4	1000 S 162-54-85-1-1	3763107	3173948	0.84	171.5	1200 S 162-97-95-1-1	11104222	9399140	0.85	198.8
800 S 200-43-95-1-2	2051688	1949104	0.95	104.1	1000 S 162-54-85-1-2	3795656	3202824	0.84	171.9	1200 S 162-97-95-1-2	11190174	9475006	0.85	199.6
800 S 200-43-90-1-1	2054935	1849441	0.90	131.1	1000 S 162-54-85-2-1	3803065	3209759	0.84	172.1	1200 S 162-97-95-2-1	11417228	9682245	0.85	199.2
800 S 200-43-90-1-2	2053228	1847905	0.90	131.0	1000 S 162-54-85-2-2	3787706	3192721	0.84	172.1	1200 S 162-97-95-2-2	11288821	9558288	0.85	198.9
800 S 200-43-85-1-1	2039118	1733250	0.85	149.9	1000 S 162-54-85-3-1	3779922	3185148	0.84	171.8	1200 S 162-97-95-3-1	11311963	9583339	0.85	199.2
800 S 200-43-85-1-2	2039534	1733604	0.85	146.8	1000 S 162-54-85-3-2	3810640	3215751	0.84	172.0	1200 S 162-97-95-3-2	11282536	9554347	0.85	199.0

2.4 Specimen imperfections

Local damage and global imperfections were observed in the beam specimens as shown in Figure 2.9 and Figure 2.10. The dominant specimen imperfection was a nonorthogonal web/flange angle, F_1 (see Table 2.2 to Table 2.5 and Figure 2.3), which imposes a web deviation from the vertical alignment when a beam was placed upon a horizontal surface. A graphical explanation of this imperfection is presented in Figure 2.11. A digital level was used to measure the inclined web angle caused by the cross-section imperfection after assembling the specimen and before loading of the beam specimens. The sign convention employed is shown in Figure 2.12. A summary of the imperfection angles is provided in Table 2.11. Note that F_1 was always measured less than 90 degrees and therefore the web inclined consistently as shown in Figure 2.11

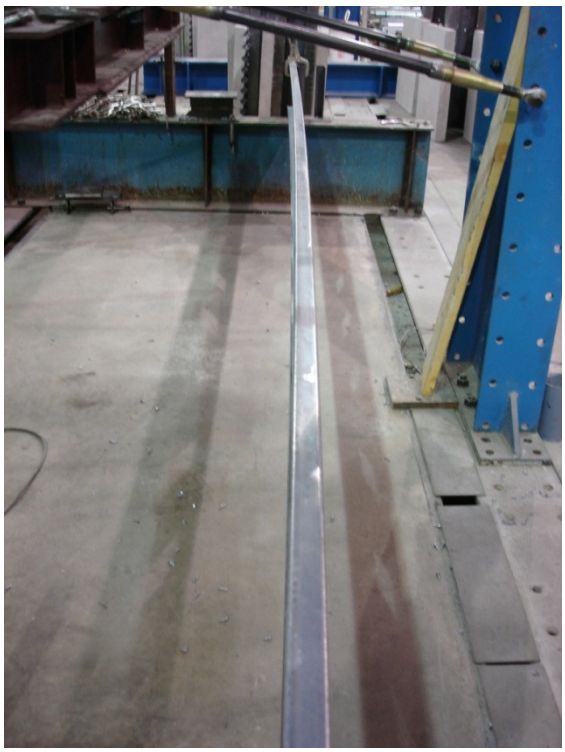

Figure 2.9. Member out-of-plumbness

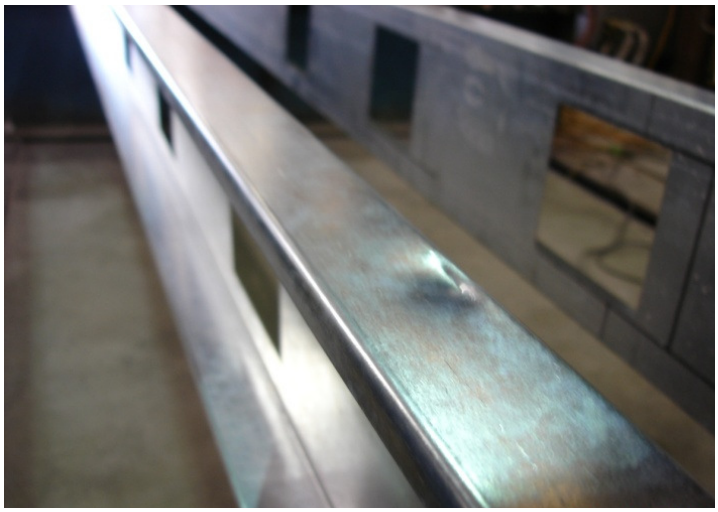

Figure 2.10. Member indentation

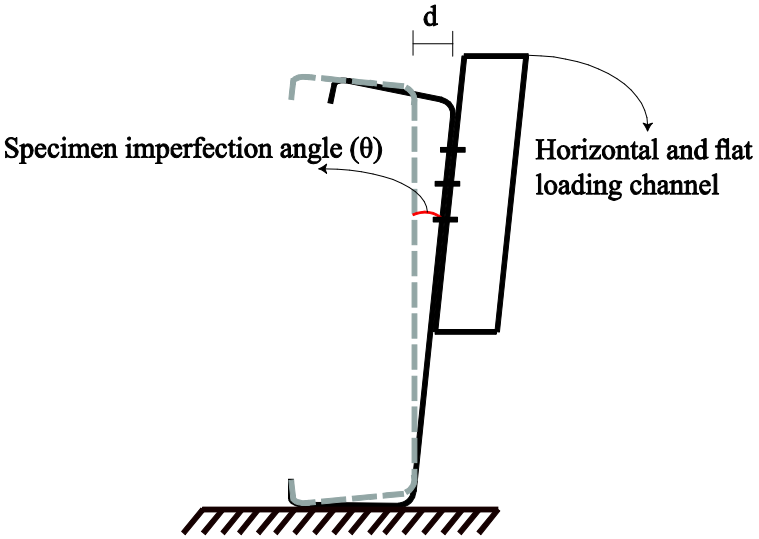

Figure 2.11. Top flange tilt

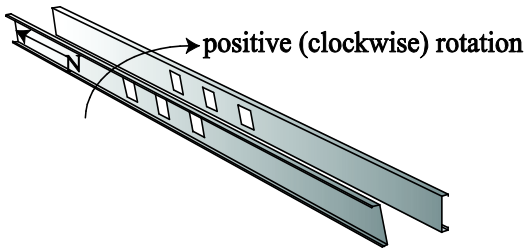

Figure 2.12. Rotations sign convention

Table 2.11 Beam specimen imperfection angle

Beam	θ degrees	Beam	θ degrees	Beam	θ degrees
800S200-33		1000S162-54		1200S162-97	
800 S 200-33-100-1-1	1.1	1000 S 162-54-100-1-1	4.1	1200 S 162-97-100-1-1	4.3
800 S 200-33-100-1-2	1.3	1000 S 162-54-100-1-2	4.3	1200 S 162-97-100-1-2	3.6
800 S 200-33-100-2-1	2.0	1000 S 162-54-100-2-1	2.7	1200 S 162-97-100-2-1	3.2
800 S 200-33-100-2-2	2.1	1000 S 162-54-100-2-2	3.0	1200 S 162-97-100-2-2	3.7
800 S 200-33-95-1-1	2.6	1000 S 162-54-100-3-1	3.2	1200 S 162-97-100-3-1	4.0
800 S 200-33-95-1-2	2.0	1000 S 162-54-100-3-2	4.2	1200 S 162-97-100-3-2	4.2
800 S 200-33-95-2-1	2.2	1000 S 162-54-95-1-1	3.9	1200 S 162-97-95-1-1	4.2
800 S 200-33-95-2-2	2.6	1000 S 162-54-95-1-2	3.5	1200 S 162-97-95-1-2	4.5
800 S 200-33-90-1-1	1.5	1000 S 162-54-95-2-1	4.4	1200 S 162-97-95-2-1	3.9
800 S 200-33-90-1-2	1.9	1000 S 162-54-95-2-2	4.2	1200 S 162-97-95-2-2	4.2
800 S 200-33-90-2-1	2.7	1000 S 162-54-95-3-1	4.2	1200 S 162-97-95-3-1	4.2
800 S 200-33-90-2-2	2.1	1000 S 162-54-95-3-2	3.8	1200 S 162-97-95-3-2	4.7
800 S 200-33-85-1-1	1.8	1000 S 162-54-90-1-1	4.6	1200 S 162-97-90-1-1	4.7
800 S 200-33-85-1-2	1.8	1000 S 162-54-90-1-2	3.9	1200 S 162-97-90-1-2	4.6
800 S 200-33-85-2-1	1.5	1000 S 162-54-90-2-1	4.0	1200 S 162-97-90-2-1	4.5
800 S 200-33-85-2-2	1.4	1000 S 162-54-90-2-2	3.6	1200 S 162-97-90-2-2	5.0
800S200-43		1000 S 162-54-90-3-1	4.3	1200 S 162-97-90-3-1	4.4
		1000 S 162-54-90-3-2	4.7	1200 S 162-97-90-3-2	4.9
800 S 200-33-95-3-1	0.6	1000 S 162-54-85-1-1	3.7	1200 S 162-97-85-1-1	4.8
800 S 200-33-95-3-2	1.1	1000 S 162-54-85-1-2	4.0	1200 S 162-97-85-1-2	5.0
800 S 200-33-90-3-1	0.5	1000 S 162-54-85-2-1	4.2	1200 S 162-97-85-2-1	3.8
800 S 200-33-90-3-2	0.5	1000 S 162-54-85-2-2	4.3	1200 S 162-97-85-2-2	3.7
800 S 200-33-85-3-1	1.5	1000 S 162-54-85-3-1	4.6	1200 S 162-97-85-3-1	3.5
800 S 200-33-85-3-2	1	1000 S 162-54-85-3-2	4.6	1200 S 162-97-85-3-2	3.3

2.5 Test configuration

The specimen used in this study consisted of a pair of 4877 mm (192 in.) beams oriented web to web and loaded in four point bending. To limit the distortional buckling and global buckling deformations outside the constant moment region, the top and bottom flanges of the beams were linked to each other using small hot-rolled steel angles 19.05×19.05×3.175 mm (3/4×3/4×1/8 in.) at 304.8 mm (12 in.) increments as shown in Figure 2.1. To simplify the

specimen setup procedure, steel clamps were used to attach the angles to the beam flanges as shown in Figure 2.15. Two pairs of cold-formed steel channels served as the loading points. The channels were installed at 813 mm (32 in.) from the midpoint of the beams and were fixed to the beam webs using self-drilling screws. Vertical loads were applied at the bearing plates (Figure 2.14), which in turn introduced the load to the beam webs through loading channels, minimizing the effects of web crippling. The loading channels were tied together using a cold-formed steel sheet at each flange plane to prevent the rotation in the webs at the loading point (Figure 2.14). The top surface of the loading channels were leveled and flattened to horizontal using a sanding machine so that flat bearing with the load spreader beam was assured (see Figure 2.14).

The beams were supported on a roller support at one end and a pinned support on the other end as shown in Figure 2.1. These supports restrained the beam in direction 1 and 2 as illustrated in Figure 2.15, providing a free-to-warp condition at the supports. The beams were also restrained in the 2 direction at the loading points using lateral braces (Figure 2.15). The lateral braces were comprised of adjustable scissor braces with the ability to change length as the actuator head moved vertically. To ensure the beams buckled globally together a cold-formed steel strap was placed at the longitudinal mid-line of the beams as shown in Figure 2.13.

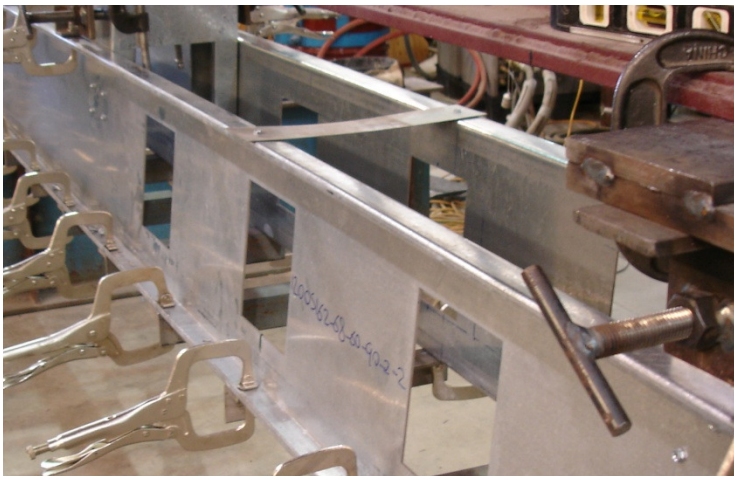

Figure 2.13 Cold-formed steel strap connecting two beams at mid-length

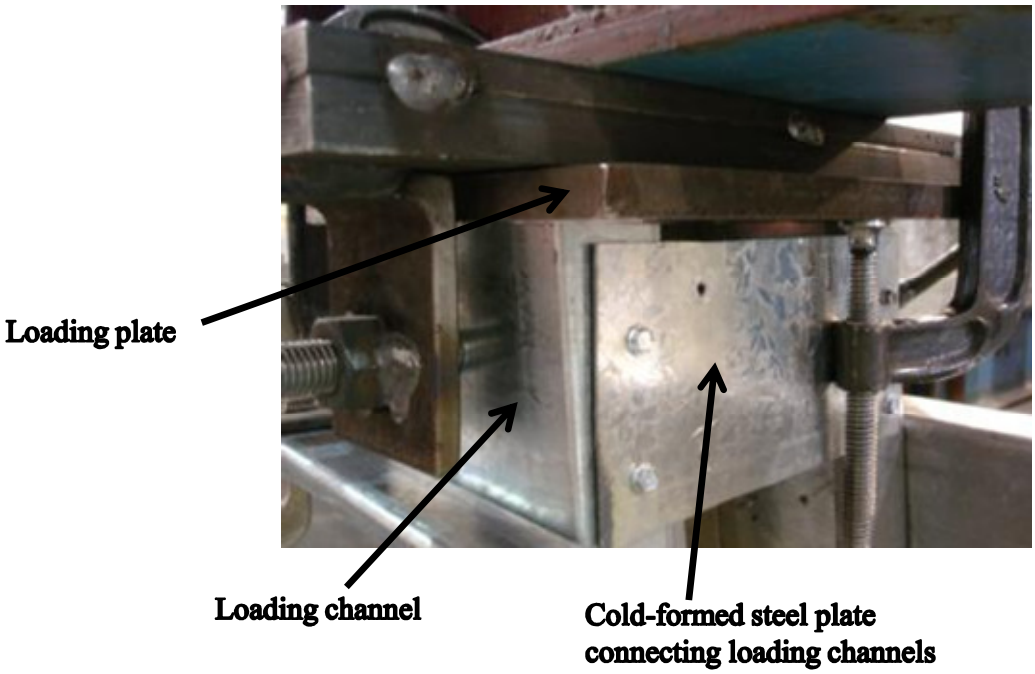

Figure 2.14. Loading details

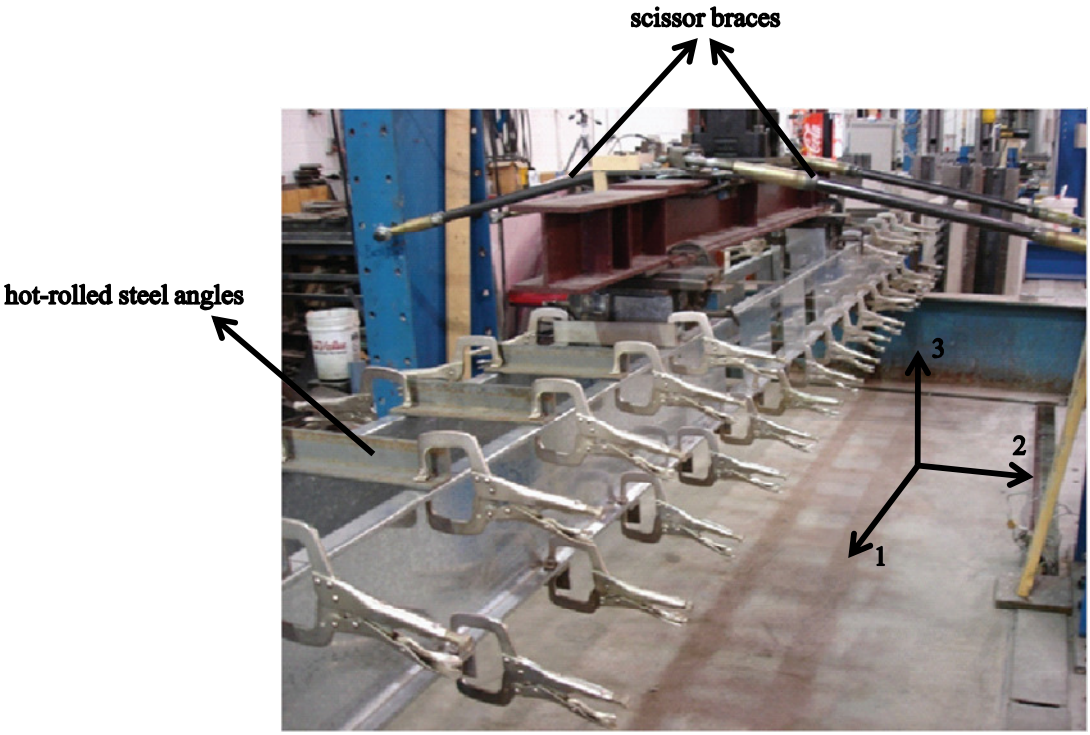

Figure 2.15. Scissor braces employed to control beam rotations

2.6 Materials testing

Tensile tests were performed on coupons cut from each beam specimen (Bowen 2009). The coupons were cut from the flanges and web of each beam, providing three data points per beam, which were tested to obtain the yield stress, f_y. The yield strength of each specimen was taken as the mean value of the data obtained from the three coupon tests.

2.6.1 Tensile coupon preparation

A 305 mm (12 in.) rough section was cut from the north end of the beams employing a plasma cutter as shown in Figure 2.16. Using a band saw, the section was further cut into 25.4×254 mm (1×10 in.) coupons and labeled using an etching grinder. These coupons were then machined into ASTM A370-07a (ASTM 2008) specified dimensions utilizing a computer numerical-controlled (CNC) milling-machine in association with a custom jig. The tensile coupon preparation procedure is graphically illustrated in Figure 2.16 and Figure 2.17.

Figure 2.16. Rough cutting of the coupons using plasma cutter (Bowen 2009)

Figure 2.17. Rough cutting of coupons using band saw (Bowen 2009)

2.6.2 Tensile test results

The results from tensile coupon tests were recorded and are presented in Table 2.12 through Table 2.15.

Table 2.12 Yield strength of the 800S200-33 beams

Name	f_y	f_{yavg}	Name	f_y	f_{yavg}	Name	f_y	f_{yavg}	Name	f_y	f_{yavg}
	MPa	MPa		MPa	MPa		MPa	MPa		MPa	MPa
800S200-33-100-1-1-EF	362		800S200-33-95-1-1-EF	364		800S200-33-90-1-1-EF	368		800S200-33-85-1-1-EF	358	
800S200-33-100-1-1-S	362	360	800S200-33-95-1-1-S	364	363	800S200-33-90-1-1-S	369	365	800S200-33-85-1-1-S	364	359
800S200-33-100-1-1-WF	356		800S200-33-95-1-1-WF	361		800S200-33-90-1-1-WF	358		800S200-33-85-1-1-WF	355	
800S200-33-100-1-2-EF	367		800S200-33-95-1-2-EF	371		800S200-33-90-1-2-EF	367		800S200-33-85-1-2-EF	360	
800S200-33-100-1-2-S	362	361	800S200-33-95-1-2-S	367	365	800S200-33-90-1-2-S	369	366	800S200-33-85-1-2-S	362	360
800S200-33-100-1-2-WF	355		800S200-33-95-1-2-WF	358		800S200-33-90-1-2-WF	361		800S200-33-85-1-2-WF	358	
800S200-33-100-2-1-EF	389		800S200-33-95-2-1-EF	369		800S200-33-90-2-1-EF	373		800S200-33-85-2-1-EF	369	
800S200-33-100-2-1-S	366	369	800S200-33-95-2-1-S	356	364	800S200-33-90-2-1-S	369	365	800S200-33-85-2-1-S	363	366
800S200-33-100-2-1-WF	353		800S200-33-95-2-1-WF	366		800S200-33-90-2-1-WF	352		800S200-33-85-2-1-WF	367	
800S200-33-100-2-2-EF	375		800S200-33-95-2-2-EF	373		800S200-33-90-2-2-EF	371		800S200-33-85-2-2-EF	366	
800S200-33-100-2-2-S	367	365	800S200-33-95-2-2-S	360	367	800S200-33-90-2-2-S	367	368	800S200-33-85-2-2-S	367	360
800S200-33-100-2-2-WF	353		800S200-33-95-2-2-WF	367		800S200-33-90-2-2-WF	365		800S200-33-85-2-2-WF	349	

Table 2.13 Yield strength of the 800S200-43 beams

Name	f_y	f_{yavg}	Name	f_y	f_{yavg}	Name	f_y	f_{yavg}	Name	f_y	f_{yavg}
	MPa	MPa		MPa	MPa		MPa	MPa		MPa	MPa
800S200-43-100-1-1-EF	326		800S200-43-95-1-1-EF	322		800S200-43-90-1-1-EF	326		800S200-43-85-3-1-EF	319	
800S200-43-100-1-1-S	320	322	800S200-43-95-1-1-S	325	322	800S200-43-90-1-1-S	322	323	800S200-43-85-3-1-S	320	319
800S200-43-100-1-1-WF	320		800S200-43-95-1-1-WF	320		800S200-43-90-1-1-WF	322		800S200-43-85-3-1-WF	318	
800S200-43-100-1-2-EF	323		800S200-43-95-1-2-EF	325		800S200-43-90-1-2-EF	323		800S200-43-85-3-2-EF	326	
800S200-43-100-1-2-S	327	323	800S200-43-95-1-2-S	325	319	800S200-43-90-1-2-S	322	323	800S200-43-85-3-2-S	325	323
800S200-43-100-1-2-WF	320		800S200-43-95-1-2-WF	309		800S200-43-90-1-2-WF	322		800S200-33-85-3-2-WF	319	

Table 2.14 Yield strength of the 1000S162-54 beams

Name	f_y	f_{yavg}	Name	f_y	f_{yavg}	Name	f_y	f_{yavg}	Name	f_y	f_{yavg}
	MPa	MPa		MPa	MPa		MPa	MPa		MPa	MPa
1000S162-54-100-1-1-EF	375	373	1000S162-54-95-1-1-EF	360	359	1000S162-54-90-1-1-EF	351	356	1000S162-54-85-1-1-EF	356	356
1000S162-54-100-1-1-S	368		1000S162-54-95-1-1-S	355		1000S162-54-90-1-1-S	352		1000S162-54-85-1-1-S	353	
1000S162-54-100-1-1-WF	377		1000S162-54-95-1-1-WF	362		1000S162-54-90-1-1-WF	364		1000S162-54-85-1-1-WF	359	
1000S162-54-100-1-2-EF	374	373	1000S162-54-95-1-2-EF	361	382	1000S162-54-90-1-2-EF	356	360	1000S162-54-85-1-2-EF	354	376
1000S162-54-100-1-2-S	371		1000S162-54-95-1-2-S	395		1000S162-54-90-1-2-S	356		1000S162-54-85-1-2-S	408	
1000S162-54-100-1-2-WF	373		1000S162-54-95-1-2-WF	391		1000S162-54-90-1-2-WF	368		1000S162-54-85-1-2-WF	367	
1000S162-54-100-2-1-EF	378	374	1000S162-54-95-2-1-EF	357	357	1000S162-54-90-2-1-EF	353	356	1000S162-54-85-2-1-EF	364	371
1000S162-54-100-2-1-S	369		1000S162-54-95-2-1-S	354		1000S162-54-90-2-1-S	351		1000S162-54-85-2-1-S	362	
1000S162-54-100-2-1-WF	375		1000S162-54-95-2-1-WF	359		1000S162-54-90-2-1-WF	364		1000S162-54-85-2-1-WF	387	
1000S162-54-100-2-2-EF	376	373	1000S162-54-95-2-2-EF	362	362	1000S162-54-90-2-2-EF	353	357	1000S162-54-85-2-2-EF	370	366
1000S162-54-100-2-2-S	369		1000S162-54-95-2-2-S	363		1000S162-54-90-2-2-S	356		1000S162-54-85-2-2-S	358	
1000S162-54-100-2-2-WF	376		1000S162-54-95-2-2-WF	360		1000S162-54-90-2-2-WF	362		1000S162-54-85-2-2-WF	371	
1000S162-54-100-3-1-EF	355	358	1000S162-54-95-3-1-EF	368	369	1000S162-54-90-3-1-EF	338	346	1000S162-54-85-3-1-EF	363	364
1000S162-54-100-3-1-S	358		1000S162-54-95-3-1-S	369		1000S162-54-90-3-1-S	348		1000S162-54-85-3-1-S	360	
1000S162-54-100-3-1-WF	362		1000S162-54-95-3-1-WF	371		1000S162-54-90-3-1-WF	353		1000S162-54-85-3-1-WF	368	
1000S162-54-100-3-2-EF	356	359	1000S162-54-95-3-2-EF	371	369	1000S162-54-90-3-2-EF	352	354	1000S162-54-85-3-2-EF	358	363
1000S162-54-100-3-2-S	358		1000S162-54-95-3-2-S	364		1000S162-54-90-3-2-S	348		1000S162-54-85-3-2-S	363	
1000S162-54-100-3-2-WF	363		1000S162-54-95-3-2-WF	372		1000S162-54-90-3-2-WF	362		1000S162-54-85-3-2-WF	367	

Table 2.15 Yield strength of 1200S162-97 beams

Name	f_y	f_{yavg}	Name	f_y	f_{yavg}	Name	f_y	f_{yavg}	Name	f_y	f_{yavg}
	Mpa	Mpa		MPa	MPa		MPa	MPa		MPa	MPa
1200S162-97-100-1-1-EF	386	373	1200S162-97-95-1-1-EF	388	371	1200S162-97-90-1-1-EF	387	365	1200S162-97-85-1-1-EF	403	390
1200S162-97-100-1-1-S	367		1200S162-97-95-1-1-S	364		1200S162-97-90-1-1-S	359		1200S162-97-85-1-1-S	387	
1200S162-97-100-1-1-WF	365		1200S162-97-95-1-1-WF	361		1200S162-97-90-1-1-WF	351		1200S162-97-85-1-1-WF	381	
1200S162-97-100-1-2-EF	389	376	1200S162-97-95-1-2-EF	378	373	1200S162-97-90-1-2-EF	395	376	1200S162-97-85-1-2-EF	404	389
1200S162-97-100-1-2-S	370		1200S162-97-95-1-2-S	379		1200S162-97-90-1-2-S	367		1200S162-97-85-1-2-S	391	
1200S162-97-100-1-2-WF	369		1200S162-97-95-1-2-WF	361		1200S162-97-90-1-2-WF	367		1200S162-97-85-1-2-WF	371	
1200S162-97-100-2-1-EF	383	367	1200S162-97-95-2-1-EF	396	377	1200S162-97-90-2-1-EF	397	381	1200S162-97-85-2-1-EF	383	380
1200S162-97-100-2-1-S	363		1200S162-97-95-2-1-S	369		1200S162-97-90-2-1-S	376		1200S162-97-85-2-1-S	383	
1200S162-97-100-2-1-WF	356		1200S162-97-95-2-1-WF	367		1200S162-97-90-2-1-WF	369		1200S162-97-85-2-1-WF	375	
1200S162-97-100-2-2-EF	384	367	1200S162-97-95-2-2-EF	367	367	1200S162-97-90-2-2-EF	376	373	1200S162-97-85-2-2-EF	384	385
1200S162-97-100-2-2-S	359		1200S162-97-95-2-2-S	369		1200S162-97-90-2-2-S	375		1200S162-97-85-2-2-S	388	
1200S162-97-100-2-2-WF	358		1200S162-97-95-2-2-WF	365		1200S162-97-90-2-2-WF	367		1200S162-97-85-2-2-WF	383	
1200S162-97-100-3-1-EF	384	372	1200S162-97-95-3-1-EF	388	374	1200S162-97-90-3-1-EF	379	373	1200S162-97-85-3-1-EF	402	396
1200S162-97-100-3-1-S	369		1200S162-97-95-3-1-S	372		1200S162-97-90-3-1-S	375		1200S162-97-85-3-1-S	400	
1200S162-97-100-3-1-WF	361		1200S162-97-95-3-1-WF	362		1200S162-97-90-3-1-WF	364		1200S162-97-85-3-1-WF	385	
1200S162-97-100-3-2-EF	387	372	1200S162-97-95-3-2-EF	402	395	1200S162-97-90-3-2-EF	393	381	1200S162-97-85-3-2-EF	395	386
1200S162-97-100-3-2-S	369		1200S162-97-95-3-2-S	381		1200S162-97-90-3-2-S	380		1200S162-97-85-3-2-S	384	
1200S162-97-100-3-2-WF	360		1200S162-97-95-3-2-WF	401		1200S162-97-90-3-2-WF	369		1200S162-97-85-3-2-WF	378	

2.7 Specimen loading

Beams were loaded using a 223 kN (50 Kip) MTS hydraulic actuator with a maximum stroke of 152 mm (6 in.) as shown in Figure 2.19. Results were recorded with a National Instruments (NI) PXI data acquisition system and monitored and archived using a custom LABVIEW code (LABVIEW 2009) as shown in Figure 2.18. All tests was performed in displacement control at a rate of 0.089 mm/sec (0.0035 in./sec) based on the experiences of Yu and Schafer (2006). The load and the displacements measured in the experiments include the frame displacements as well as the system effects. Plate columns and plate girder with the dimensions provided in Figure 2.20 were used to assemble the test frame.

Figure 2.18. MTS 407 controller and NI data acquisition system

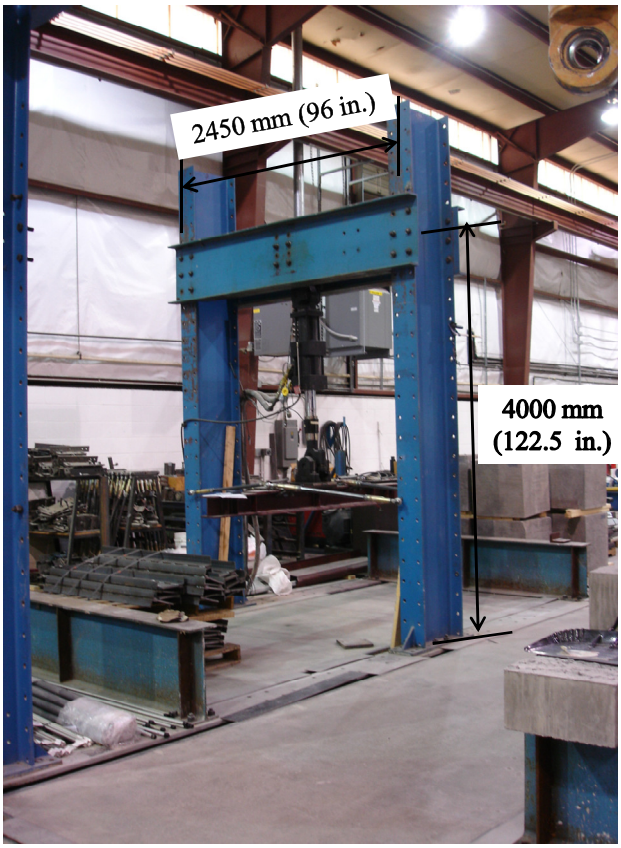

Figure 2.19. MTS actuator and loading frame

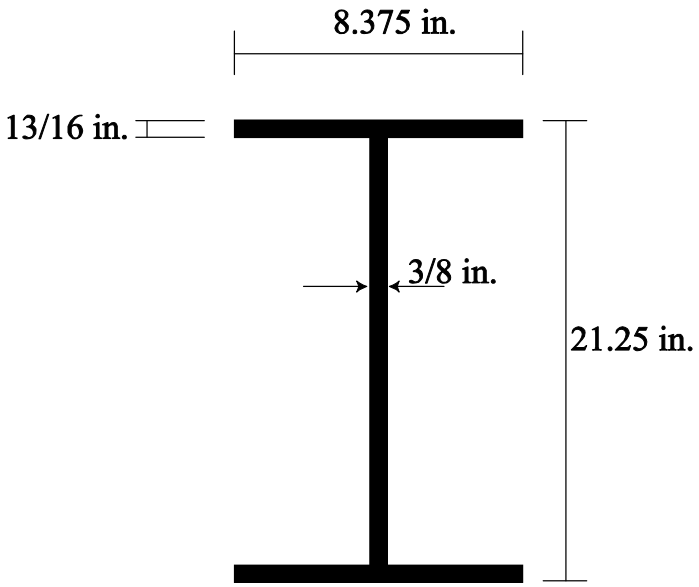

Figure 2.20 Cross-section used to build the test frame

Chapter 3. Finite element elastic buckling of beams with holes

Finite element eigen-buckling analyses were performed in ABAQUS to determine the elastic buckling properties of each test specimen including the influence of holes and boundary conditions. The characteristics of the finite element model as well as the analysis considerations and results are detailed in this chapter. The critical elastic buckling moments ($M_{cr\ell}$, M_{crd}, M_{cre}) for each beam specimen are determined for use with the AISI Direct Strength Method discussed in Chapter 5.

3.1 Model characteristics

The eigen-buckling analyses of the beam specimens were performed in ABAQUS with the S9R5 thin shell element (ABAQUS 2009). The S9R5 element has 9 nodes and 5 degrees of freedom per node (three translational and two rotational). At each node, the rotational degree of freedom around the axis normal to the mid-plane of the shell is removed for computational efficiency purposes. The S9R5 element employs a quadratic interpolation to compute the deformations between the nodes. The letter R in S9R5 implies that a reduced integration was used throughout the analysis. This means that the number of Gaussian integration points was reduced to avoid shear locking in addition to increasing the efficiency of the analysis. The S9R5 element was chosen due to higher accuracy achieved while performing the eigen-buckling analysis of a stiffened and an unstiffened plate (Moen 2008). The zinc thickness, $t_{zinc,}$ was used to calculate the centerline cross-section dimensions from the out-to-out measurements to be used in the finite element model. This was performed by subtracting $t_{zinc}/2$ value from all out-to-out dimensions. A typical element aspect ratio of 1:1 and a maximum aspect ratio of 8:1 were used

in the model. Element meshing is carried out using a custom built Matlab (Mathworks 2009) program. A modulus of elasticity of E=29500 ksi and the Poisson's ratio ν=0.3 are assumed in the finite element models.

In order to study the effect of holes in the strength of the beams, an accurate simulation of holes in the model is necessary. In this study, a custom Matlab code was used to generate the finite element mesh of a hole (Mathworks 2009). The code creates four layers of S9R5 elements around each hole as shown in Figure 3.1. Observations show that the elements at the bisection of the 90-degree plate corners possess the sharpest isoparametric element angles. In order to have an accurate integration of the element stiffness matrix, ABAQUS suggests that the element angles remain between 45 and 135 degrees (ABAQUS 2009). A complete discussion of the hole modeling process as well as the detailed mesh generating program is provided in Moen (2008).

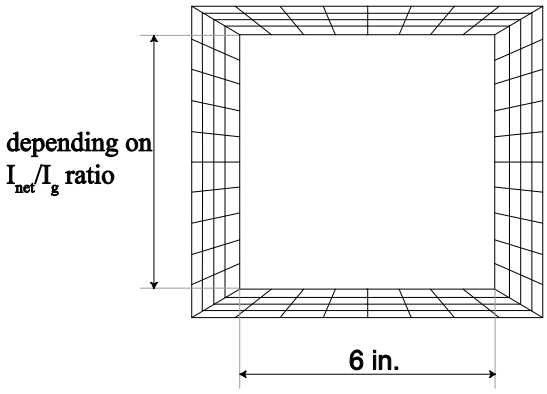

Figure 3.1. S9R5 elements layout around the rectangular hole

3.2 Loads and boundary conditions in ABAQUS

The boundary conditions applied in the finite element model as well as the location and the magnitude of the loads are presented in Figure 3.2. The loads and the boundary conditions employed were intended to match the experimental set up discussed in Section 2.4. A unit load was applied on each beam (half of unit load at each loading point). The loads were applied as

point loads on a set of 27 nodes on the web of the beam in order to properly simulate the experimental loading conditions (Figure 3.2).

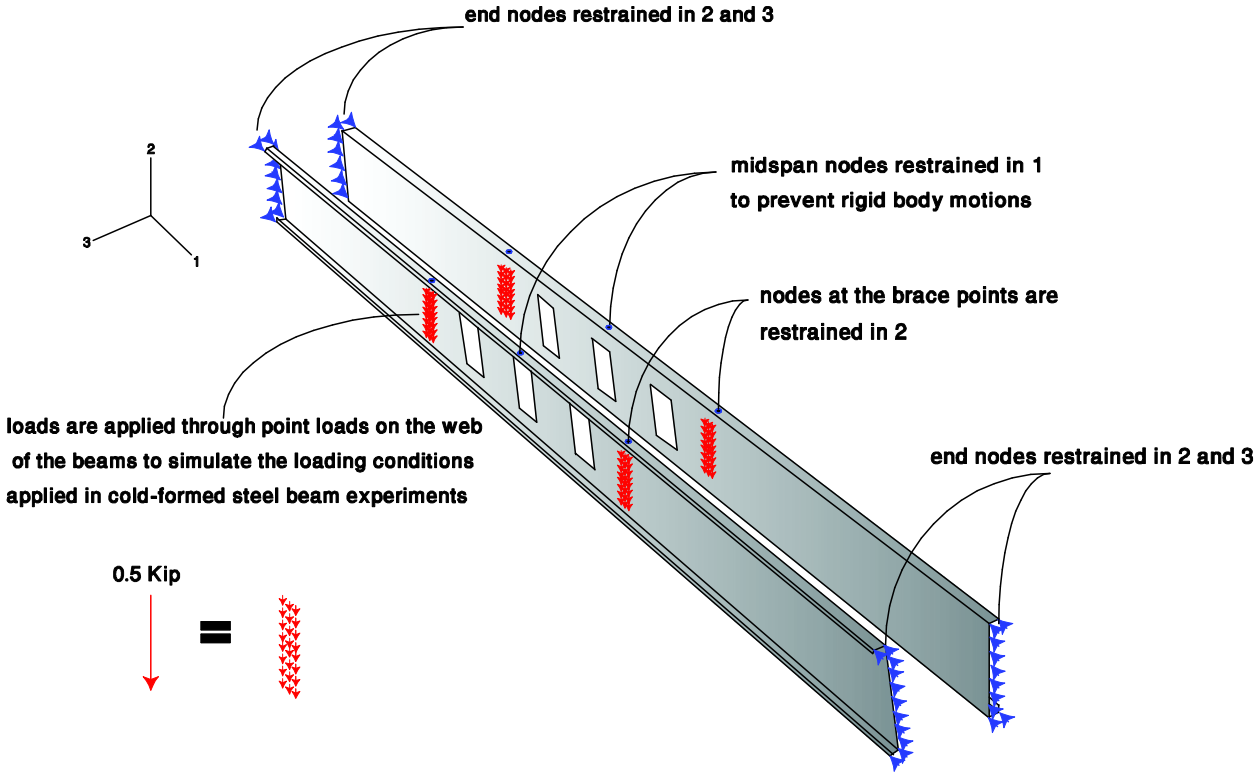

Figure 3.2. loading and boundary conditions in finite element model

Both beams were restrained vertically and transversely at the supports (restrained in directions 2 and 3 in Figure 3.2). Additionally in order to prevent the rigid body motions in the model both beams were restrained in direction 1 at the mid-span. The lateral-bracing restraint enforced by the loading points was also applied in direction 2.

3.3 Eigen-buckling analysis using Lanczos eigensolver

To calculate the critical buckling loads, ABAQUS solves the eigen-problem presented in Eq (3.1) where K_e and K_g represent the elastic and geometrical stiffness of the model respectively and λ and φ stand for the buckling load (eigen value) and the mode shape (eigen vector) corresponding to the eigen-problem.

$$([K_e] - \lambda[K_g]) \times \{\phi\} = \{0\} \quad (3.1)$$

ABAQUS implements two solvers to approach an eigen-problem: Lanczos and Subspace. Lanczos is a fast method when a large number of eigen-modes are required but Subspace may be faster if only a few (less than 20) eigen-modes are needed (ABAQUS 2009). In this study since the number of targeted eigen-modes were more than 100, the Lanczos eigen-solver was selected for the analysis procedure.

3.4 Elastic buckling results

The eigen-buckling analysis of the beams was carried out using ABAQUS. The analysis results have been meticulously examined and the specific elastic buckling moments were differentiated manually by the author. The description of different buckling modes captured through the eigen-buckling analysis follows. In order to simplify the procedure to capture the critical elastic buckling moments a pre-analysis was performed employing finite strip method software, CUFSM (Schafer and Adány 2006).

3.4.1 Finite strip pre-analysis

The finite strip method was used as a tool for pre-analyzing the beam specimens. Since the finite strip method is based on a boundary conditions different than the formation used throughout the experiments, the buckling values captured through finite strip analysis were only used to provide an upper and lower bounds for the critical local, distortional and lateral-torsional buckling moments. Therefore, the search for the critical buckling modes was reduced to the modes with buckling moments (eigen-values) in between the upper and lower boundaries provided. The pre-analysis results are tabulated in Table 3.1 through Table 3.4.

Table 3.1 Critical buckling moments for 800S200-33 using finite strip method

800S200-33							
Name	$M_{cr\ell}$	$L_{cr\ell}$	M_{crd}	L_{crd}	M_{cre}	L_{cre}	M_y
	kN.m	mm	kN.m	mm	kN.m	mm	kN.m
800 S 200-33-100-1-1	1.50	109	2.40	498	5.45	1626	5.45
800 S 200-33-100-1-2	1.80	112	2.77	498	5.73	1626	5.38
800 S 200-33-100-2-1	1.49	112	2.38	498	5.20	1626	5.64
800 S 200-33-100-2-2	1.64	109	2.55	498	5.45	1626	5.44
800 S 200-33-95-1-1	1.43	112	2.39	498	5.35	1626	5.48
800 S 200-33-95-1-2	1.85	112	2.81	498	4.75	1626	5.57
800 S 200-33-95-2-1	1.48	112	2.31	498	5.53	1626	5.46
800 S 200-33-95-2-2	1.69	112	2.68	498	5.31	1626	5.48
800 S 200-33-90-1-1	1.47	112	2.37	498	5.04	1626	5.55
800 S 200-33-90-1-2	1.66	112	2.64	498	5.51	1626	5.55
800 S 200-33-90-2-1	1.53	112	2.48	498	5.48	1626	5.55
800 S 200-33-90-2-2	1.66	112	2.61	498	5.52	1626	5.44
800 S 200-33-85-1-1	1.45	109	2.33	498	5.44	1626	5.28
800 S 200-33-85-1-2	1.65	112	2.62	498	5.45	1626	5.35
800 S 200-33-85-2-1	1.52	109	2.42	498	5.58	1626	5.50
800 S 200-33-85-2-2	1.66	109	2.66	498	5.57	1626	5.33

Table 3.2 Critical buckling moments for 800S200-43 using finite strip method

800S200-43							
Name	$M_{cr\ell}$	$L_{cr\ell}$	M_{crd}	L_{crd}	M_{cre}	L_{cre}	M_y
	kN.m	mm	kN.m	mm	kN.m	mm	kN.m
800 S 200-43-95-1-1	3.43	112	4.65	414	7.79	1626	6.51
800 S 200-43-95-1-2	3.91	112	4.74	414	7.85	1626	6.41
800 S 200-43-90-1-1	3.47	112	4.57	414	7.78	1626	6.50
800 S 200-43-90-1-2	3.85	112	4.70	394	7.73	1626	6.47
800 S 200-43-85-1-1	3.47	112	4.70	414	7.92	1626	6.36
800 S 200-43-85-1-2	3.84	112	4.57	394	7.80	1626	6.39

Table 3.3 Critical buckling moments for 1000S162-54 using finite strip method

1000S162-54							
Name	$M_{cr\ell}$	$L_{cr\ell}$	M_{crd}	L_{crd}	M_{cre}	L_{cre}	M_y
	kN.m	mm	kN.m	mm	kN.m	mm	kN.m
1000 S 162-54-100-1-1	5.18	140	5.84	318	6.78	1626	11.11
1000 S 162-54-100-1-2	4.76	152	5.08	305	6.78	1626	11.04
1000 S 162-54-100-2-1	4.96	140	5.55	318	7.68	1626	10.50
1000 S 162-54-100-2-2	4.68	152	4.92	295	6.52	1626	10.60
1000 S 162-54-100-3-1	5.17	140	5.93	330	8.15	1626	10.26
1000 S 162-54-100-3-2	4.69	152	4.93	295	6.55	1626	10.42
1000 S 162-54-95-1-1	5.13	140	5.69	305	7.75	1626	11.06
1000 S 162-54-95-1-2	4.83	152	5.14	305	6.76	1626	11.08
1000 S 162-54-95-2-1	5.05	140	5.56	318	7.78	1626	10.93
1000 S 162-54-95-2-2	4.69	152	4.98	295	6.61	1626	10.88
1000 S 162-54-95-3-1	5.10	140	5.73	318	8.07	1626	10.59
1000 S 162-54-95-3-2	4.78	152	5.06	295	6.72	1626	11.12
1000 S 162-54-90-1-1	5.10	140	5.81	318	5.99	1626	10.56
1000 S 162-54-90-1-2	4.79	140	5.36	318	6.79	1626	10.56
1000 S 162-54-90-2-1	5.25	140	5.87	318	8.15	1626	10.62
1000 S 162-54-90-2-2	4.80	152	5.09	305	6.81	1626	10.67
1000 S 162-54-90-3-1	5.23	140	5.97	318	8.32	1626	11.10
1000 S 162-54-90-3-2	4.85	152	5.07	295	6.81	1626	10.97
1000 S 162-54-85-1-1	5.12	140	5.70	318	7.75	1626	10.60
1000 S 162-54-85-1-2	4.85	152	5.09	295	6.69	1626	11.38
1000 S 162-54-85-2-1	5.12	140	5.80	318	8.00	1626	10.61
1000 S 162-54-85-2-2	4.92	140	5.47	318	6.96	1626	10.61
1000 S 162-54-85-3-1	5.13	140	5.74	318	7.95	1626	10.78
1000 S 162-54-85-3-2	4.82	152	5.08	295	6.62	1626	10.84

Table 3.4 Critical buckling moments for 1200S162-97 using finite strip method

1200S162-97							
Name	$M_{cr\ell}$	$L_{cr\ell}$	M_{crd}	L_{crd}	M_{cre}	L_{cre}	M_y
	kN.m	mm	kN.m	mm	kN.m	mm	kN.m
1200 S 162-97-100-1-1	31.18	140	26.22	267	20.91	1626	27.29
1200 S 162-97-100-1-2	31.49	140	26.72	267	20.15	1626	27.55
1200 S 162-97-100-2-1	29.27	140	24.61	267	19.56	1626	27.66
1200 S 162-97-100-2-2	30.75	140	26.27	267	20.49	1626	25.90
1200 S 162-97-100-3-1	30.91	140	25.86	267	21.15	1626	27.55
1200 S 162-97-100-3-2	32.87	140	28.01	267	22.95	1626	27.79
1200 S 162-97-95-1-1	31.34	140	26.68	267	22.17	1626	27.41
1200 S 162-97-95-1-2	32.60	140	27.61	267	22.48	1626	27.58
1200 S 162-97-95-2-1	31.71	140	27.15	267	22.29	1626	28.05
1200 S 162-97-95-2-2	30.72	140	25.64	267	21.55	1626	28.96
1200 S 162-97-95-3-1	31.14	140	26.42	267	21.56	1626	28.73
1200 S 162-97-95-3-2	32.56	140	27.67	267	22.36	1626	29.21
1200 S 162-97-90-1-1	30.71	140	26.01	267	21.02	1626	27.10
1200 S 162-97-90-1-2	31.57	140	26.81	267	19.75	1626	27.50
1200 S 162-97-90-2-1	31.08	140	26.13	267	21.10	1626	26.82
1200 S 162-97-90-2-2	30.59	140	25.87	267	19.39	1626	27.53
1200 S 162-97-90-3-1	30.81	140	25.98	267	20.62	1626	27.83
1200 S 162-97-90-3-2	30.31	140	25.71	267	19.46	1626	27.84
1200 S 162-97-85-1-1	29.90	140	25.50	267	20.26	1626	27.03
1200 S 162-97-85-1-2	29.25	140	24.62	267	19.25	1626	27.33
1200 S 162-97-85-2-1	31.56	140	26.41	267	20.02	1626	28.47
1200 S 162-97-85-2-2	33.82	140	28.96	267	22.37	1626	27.61
1200 S 162-97-85-3-1	31.63	140	26.63	267	20.62	1626	29.35
1200 S 162-97-85-3-2	31.60	140	26.42	267	21.61	1626	28.56

3.4.2 Finite element results

3.4.2.1 Local buckling

The local buckling modes for the 800S200-33 beams are shown in Figure 3.3 through Figure 3.6. Investigation of the critical local buckling moment for the no-hole beam indicates that the critical buckling moment ($M_{cr\ell}$=1.52 kN. m) and the half-wave length ($L_{cr\ell}$ =109 mm) are in good agreement with the results obtained from the finite strip analysis of the beams (see Section 3.4.1)

.

Figure 3.5 and Figure 3.6 show the local buckling modes captured in 800S200-33-95-1 and 800S200-33-90-1 beams. Three unique local buckling modes, LH, LH2 and L were observed. The LH and LH2 mode are characterized by single and double half-waves along the unstiffened strip above a web hole while the pure local buckling mode (L) occurs in between the web holes. Figure 3.3 provides a baseline view of local buckling, note that the critical local buckling mode forms at $L_{cr\ell}$=139.7 mm (5.5 in.) Comparison of the critical buckling moments corresponding to LH, LH2 and L modes for each cross-section denotes that the LH mode has the lowest buckling load. This suggests that this mode (LH) is likely to appear before the two other modes in the experiments. A mixing of the local and distortional buckling modes is also observed in the behavior of the beams with holes. The local buckling mode captured for the 800S200-33-85-1 beam is shown in Figure 3.4. The critical modes exhibit a mixture of local and distortional buckling modes, i.e. the distortional buckling effects were noticeably increased while the local buckling modes (LH and LH2) were restrained due to the reduced width of the unstiffened element.

Evaluation of the critical moments for 800S200-33-100-1, 800S200-33-95-1, 800S200-33-90-1 and 800S200-33-85-1 beams indicate an increase in the critical buckling load with an increasing hole depth (i.e. the critical buckling moment causing the local buckling modes increases for beams with larger slotted web-holes). This is due to the wave-length stiffening effects of the strip above the hole which damps the local buckling mode in the unstiffened strip and forces the local half-waves to form in between the holes (Moen and Schafer 2009).

The local buckling modes observed in the 800S200-43 beams were similar to the local buckling modes for the 800S200-33-85-1 beam. As shown in Figure 3.7. It is observed that with an increase in the web-holes depth, the critical local buckling moment of the beams increases.

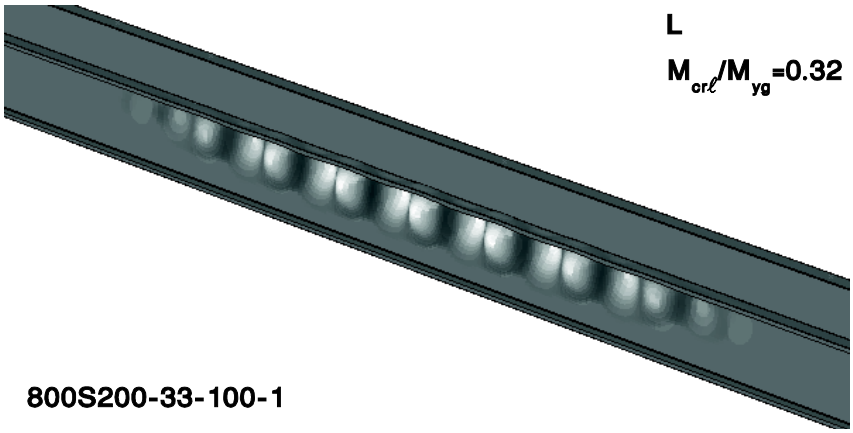

Figure 3.3. Local buckling mode in 800S200-33-100-1 beam

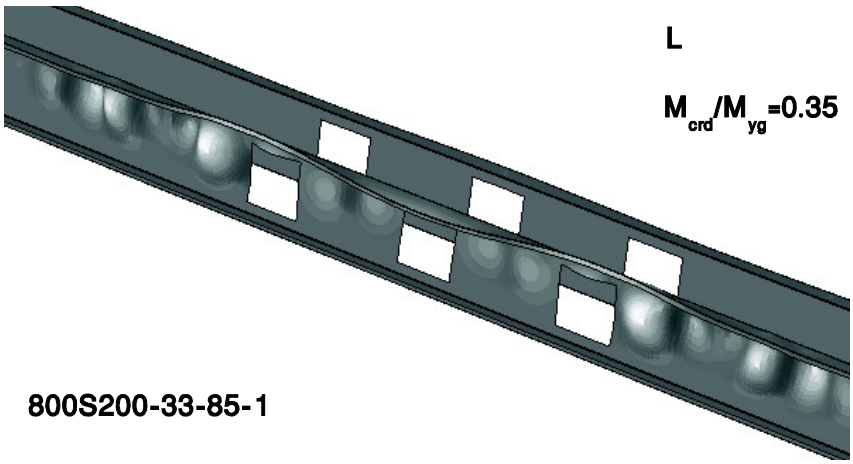

Figure 3.4. Local buckling mode in the 800S200-33-85-1 beam

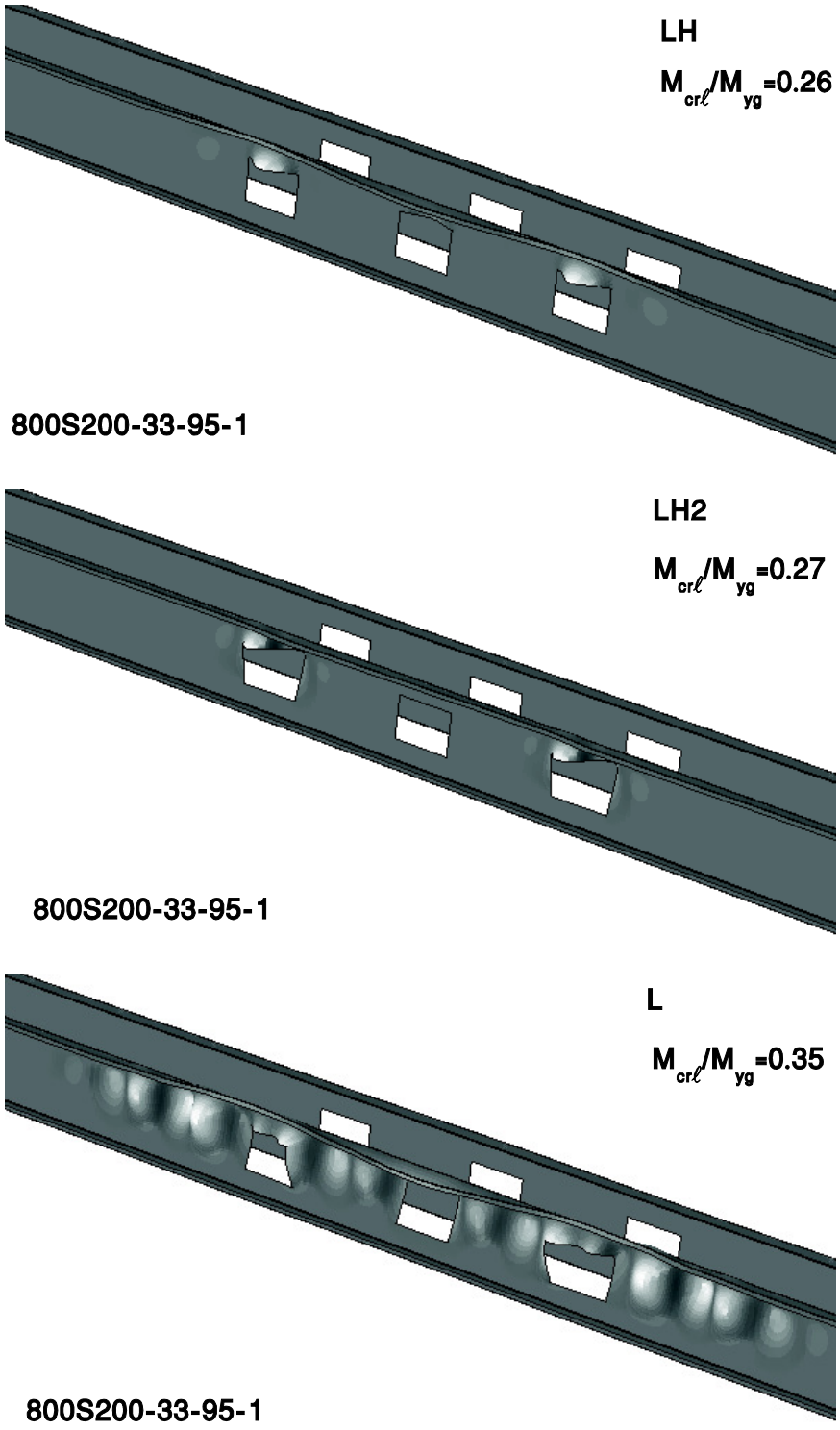

Figure 3.5. Local buckling modes in 800S200-33-95-1 beam

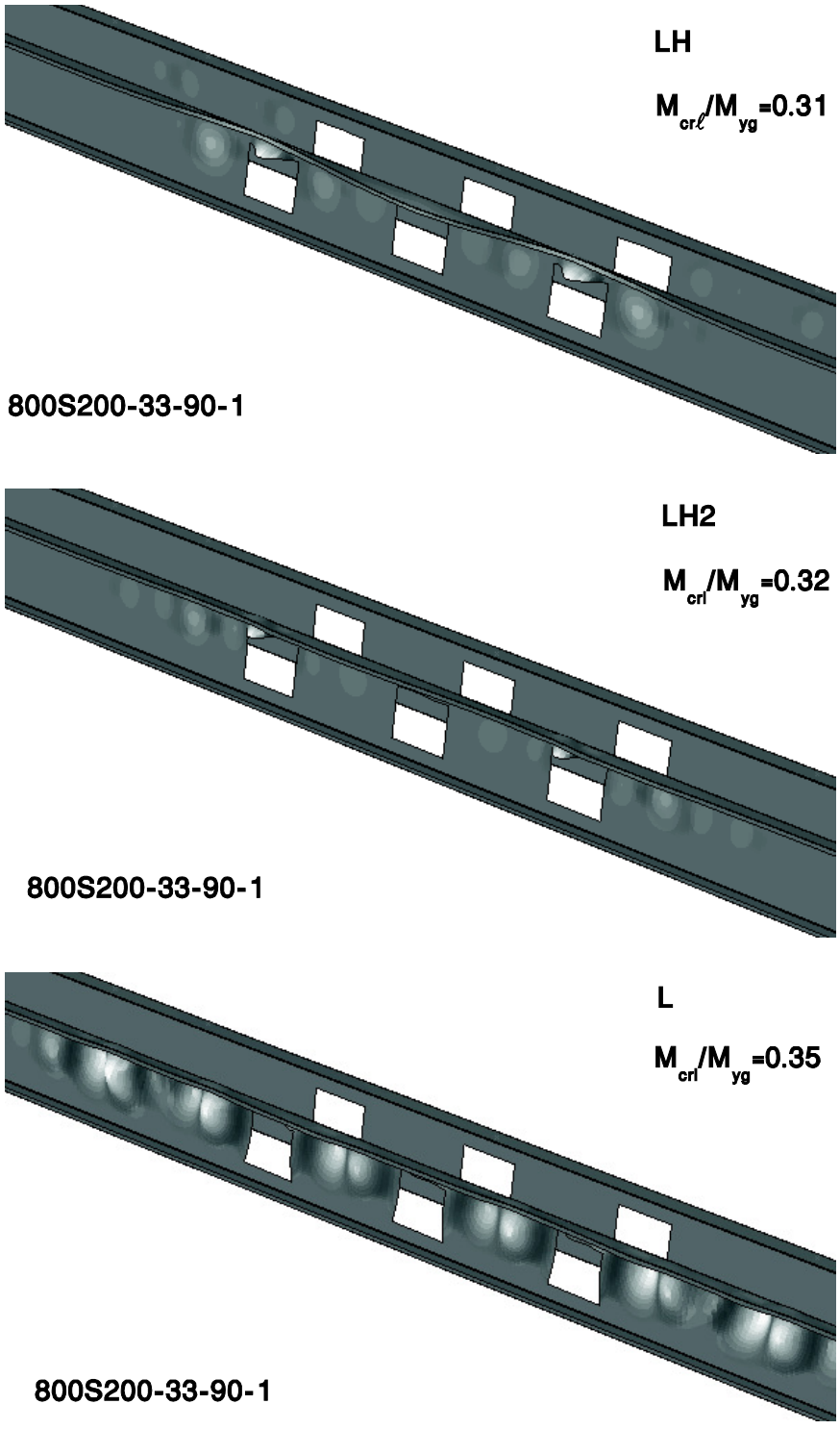

Figure 3.6. Local buckling modes in 800S200-33-90-1 beam

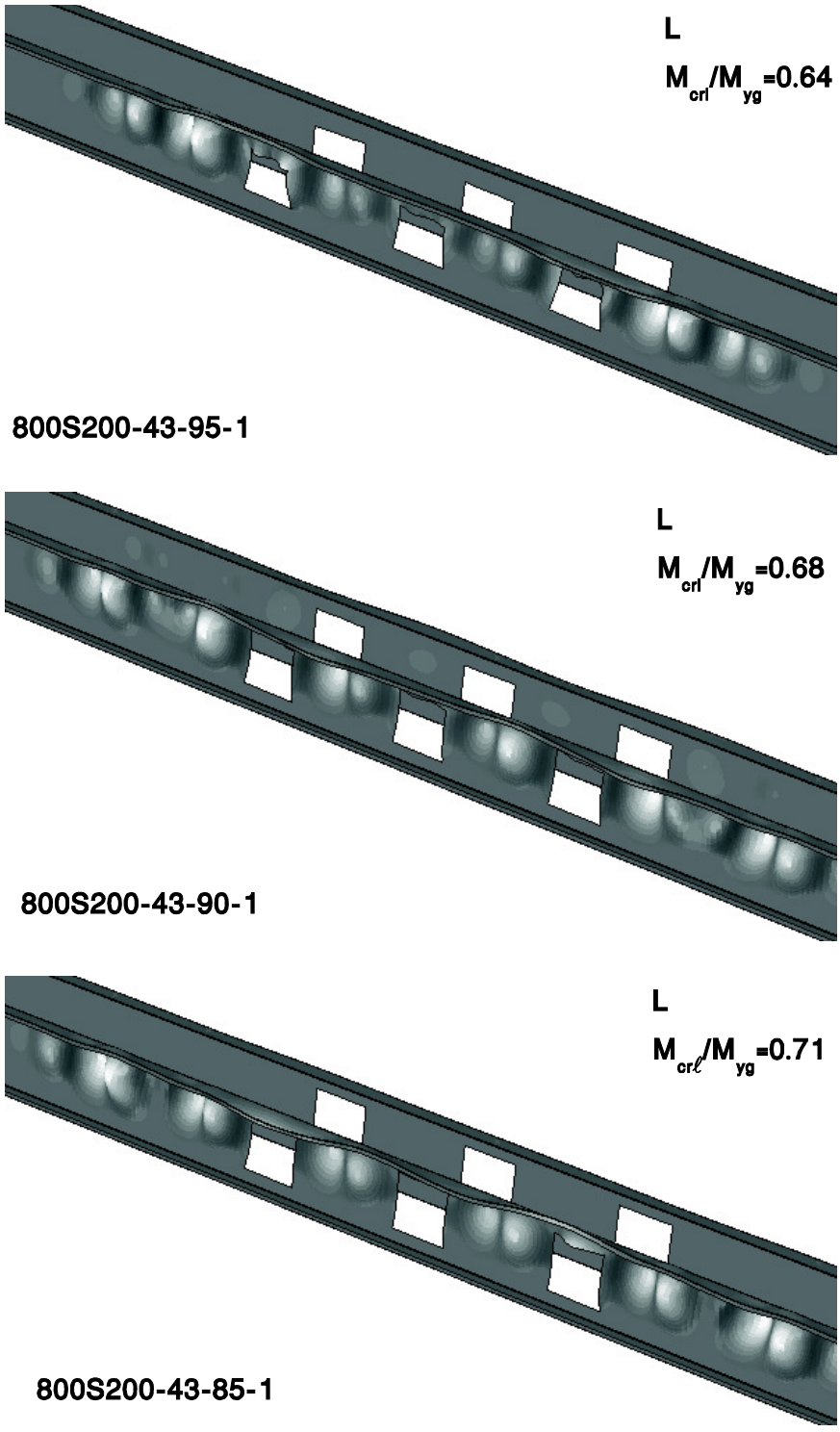

Figure 3.7. Comparison of local buckling modes in 800S200-43-95-1, 800S200-43-90-1 and 800S200-43-85-1

The local buckling behavior of the hole and no-hole 1000S162-54 beams are shown in Figure 3.8 through Figure 3.11. The local buckling modes (LH, LH2 and L) captured for the 1000S162-54 beams are similar to the modes that appeared in 800S200-33 beams with the exception that the critical buckling moments associated with the buckling modes are higher for the 1000S162-54 case.

Investigation of Figure 3.9 through Figure 3.11 suggests that the LH mode is the first local buckling mode to appear in the 1000S162-54 hole beams. The critical buckling moment associated with the LH mode is 19 percent less than the pure local mode (L) for the 1000S162-54-95-1 beam. This large difference is due to the low axial stiffness of the unstiffened strip.

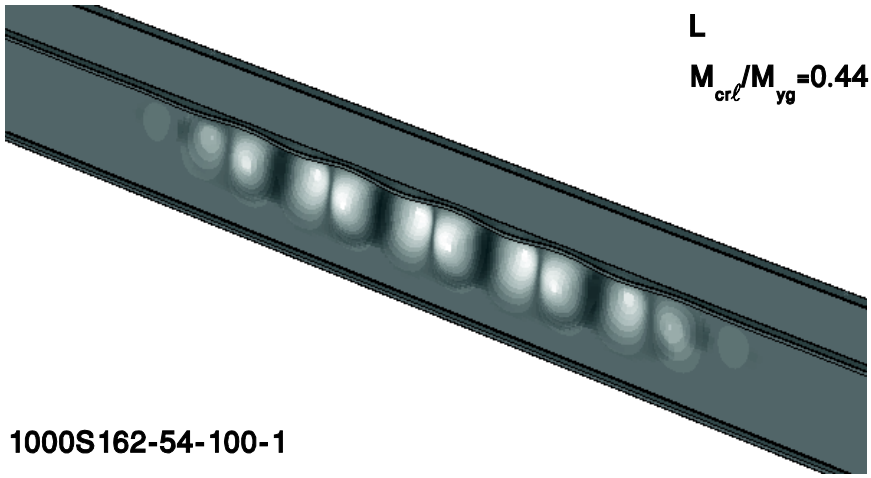

Figure 3.8. Local buckling modes in 1000S162-54-100-1

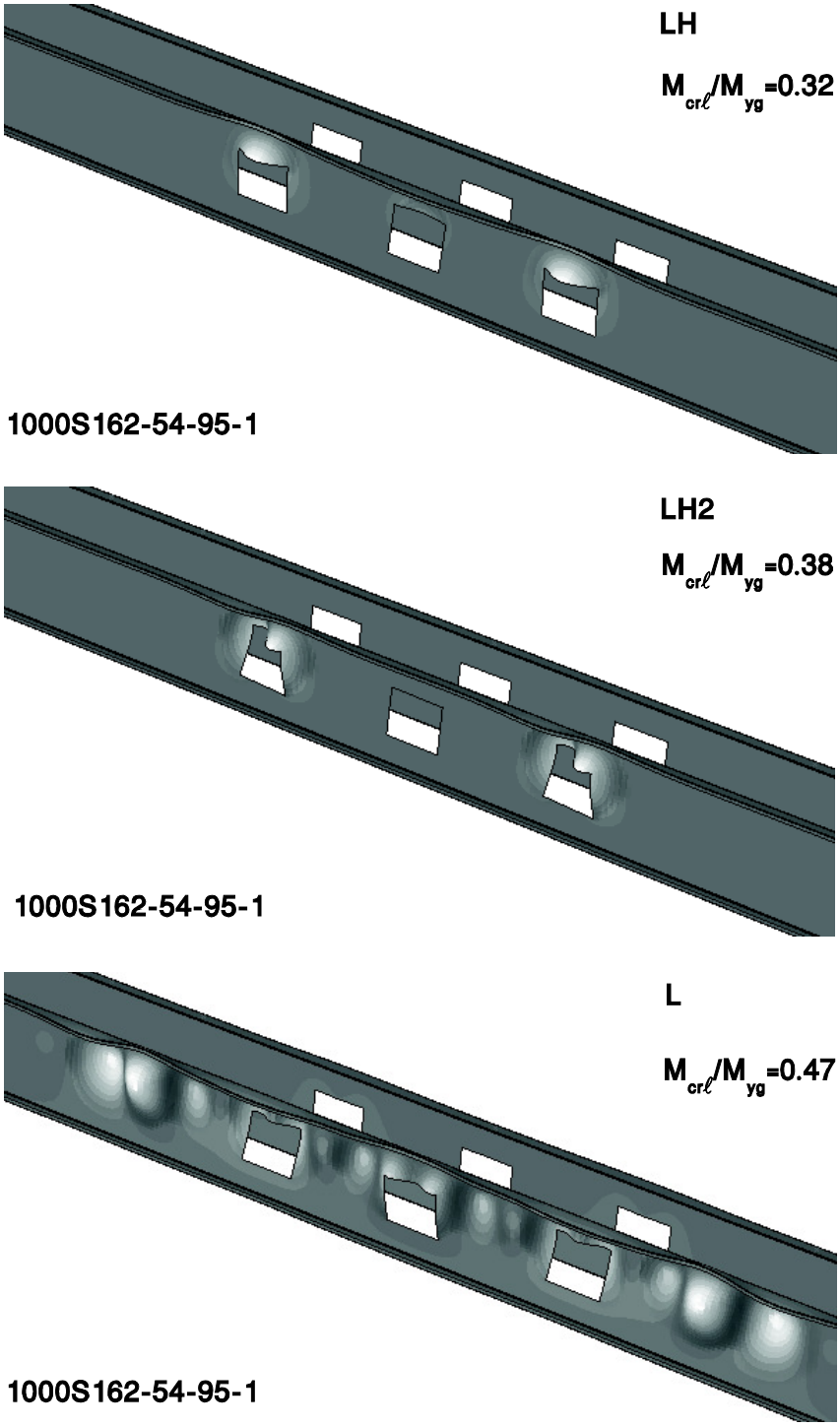

Figure 3.9. Local buckling modes in 1000S162-54-95-1

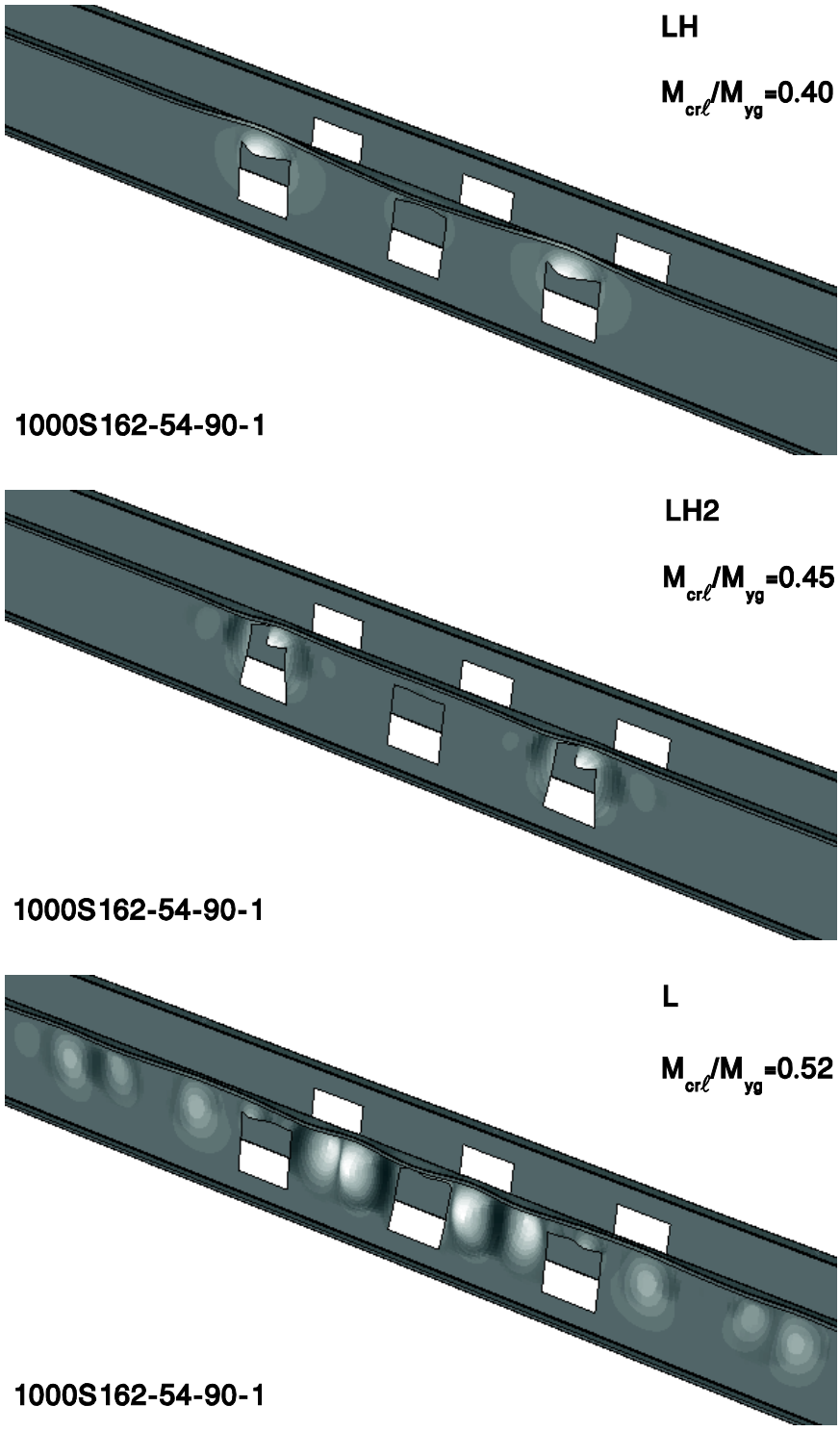

Figure 3.10. Local buckling modes in 1000S162-54-90-1

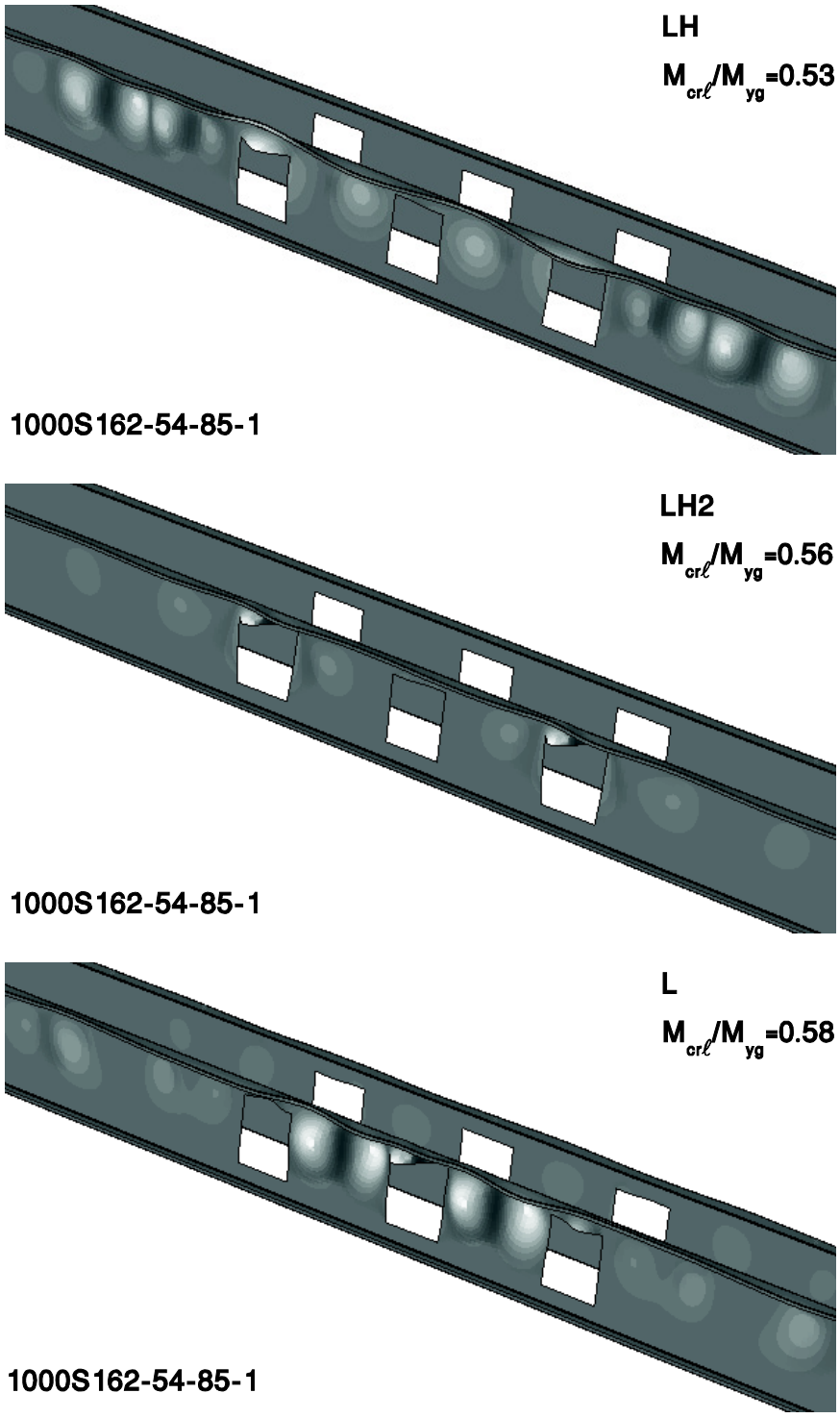

Figure 3.11. Local buckling modes in 1000S162-54-85-1

The local buckling modes captured in 1200S162-97 beams are shown in Figure 3.14. Since the local half-wave length exceeds the hole length, the LH2 mode was not observed. The LH mode is captured at a critical buckling moment about 42, 36 and 23 percent lower than the pure local buckling mode for the 1200S162-97-95-1, 1200S162-97-90-1 and 1200S162-97-85-1 beams respectively. Evaluation of $M_{cr\ell}$ for the 1200S162-97 hole beams demonstrates that the critical buckling moment increases with increasing hole depth.

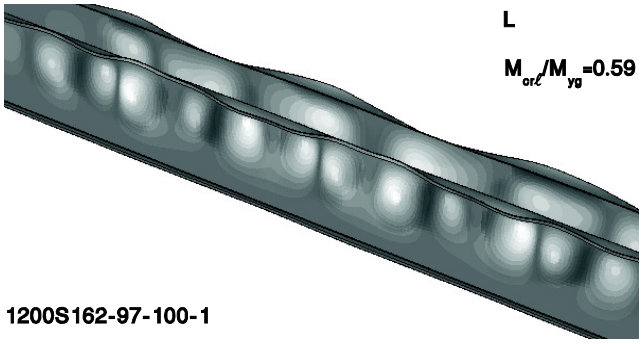

Figure 3.12. Local buckling modes in 1200S162-97-100-1

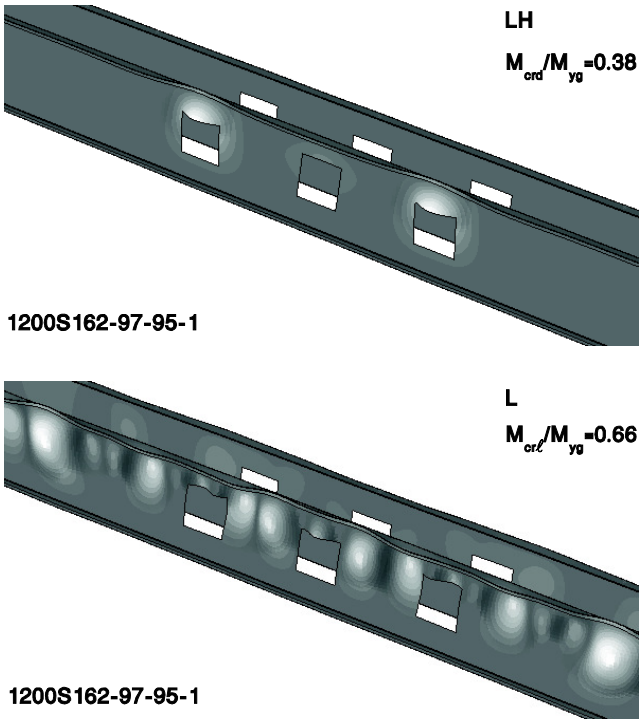

Figure 3.13. Local buckling modes in 1200S162-97-95-1

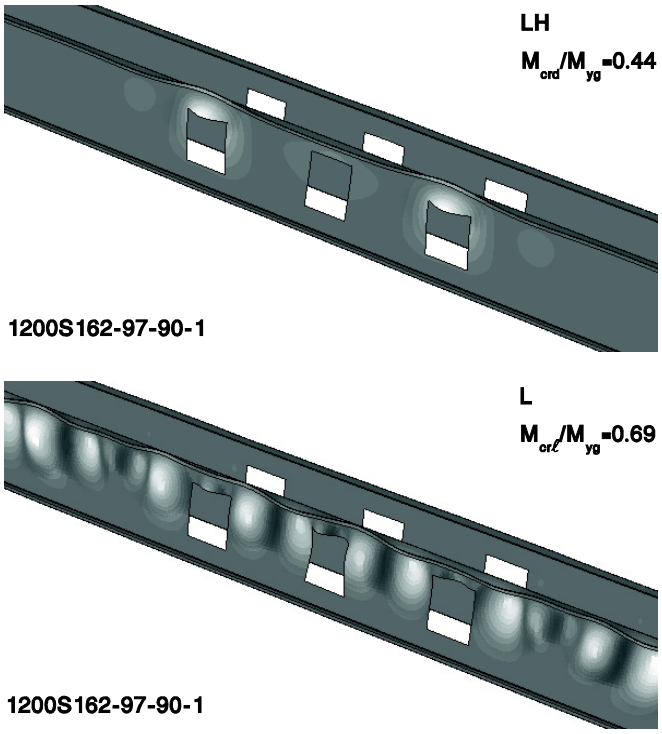

Figure 3.14. Local buckling modes in 1200S162-97-90-1

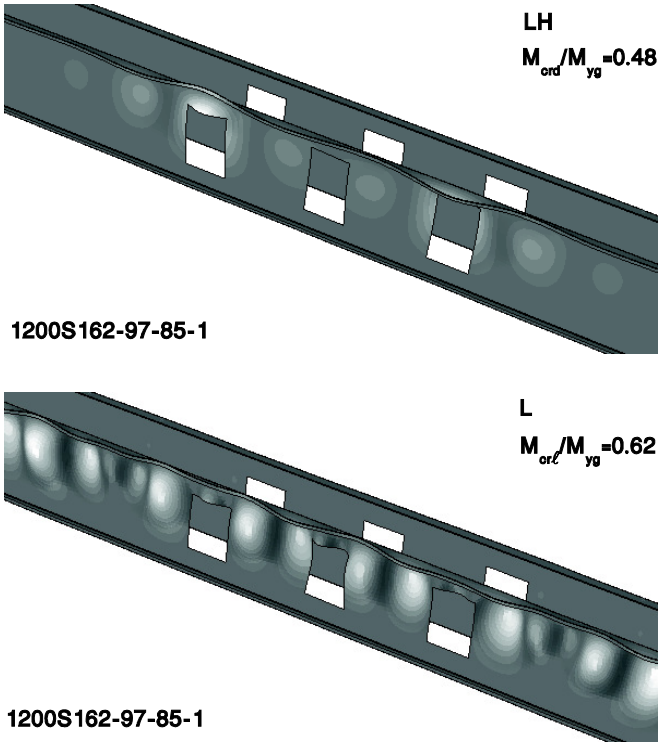

Figure 3.15. Local buckling modes in 1200S162-97-85-1

The trend in local buckling moments with respect to the hole sizes is provided in Figure 3.16. An increase in the local buckling capacity of the beams is observed with an increasing hole size. The small web holes are observed to decrease the critical buckling moments comparing to the critical buckling moments for the no hole beams while either an increase or decrease in the critical buckling moments is observed when larger web holes are present.

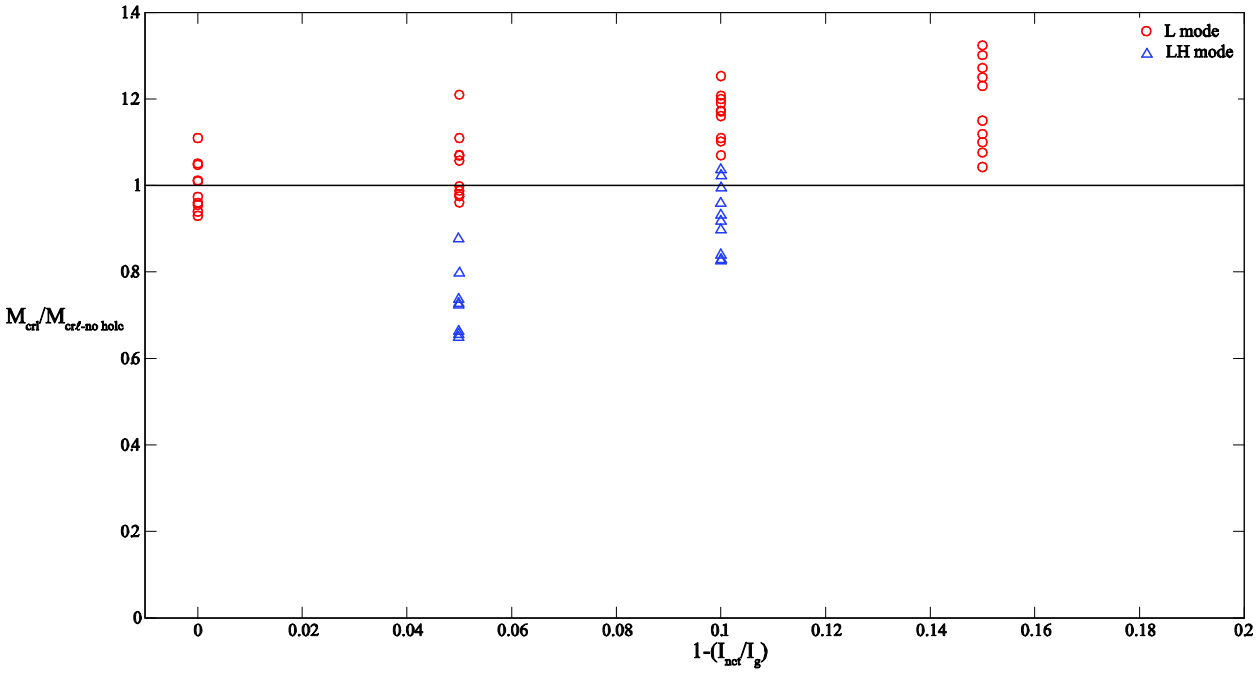

Figure 3.16. Local buckling moments with respect to the hole size

3.4.2.2 Distortional buckling

The distortional buckling modes identified for hole and no-hole 800S200-33 beams is shown in Figure 3.17. The common buckling mode obtained for 800S200-33 hole beams is the DH+L mode, which suggests a mixing between the distortional half-waves appearing in the compression flange and the local half-waves emerging in the web of the beam. The DH+L mode is similar to the LH mode (see Section 3.5.1) with an exception of longer half-waves, which extends beyond the hole length. The strategy employed to differentiate between the DH+L and LH mode was through tracking the extent of deformations in the compression flange as well as the web (i.e. the LH mode is characterized by larger deformations in the unstiffened strip while the DH+L mode is distinguished by large compression flange deformations). Comparison of the M_{crd} values for the 800S200-33-100-1 and 800S200-33-95-1 indicates that the critical distortional buckling moments decrease by as much as 22 percent when incorporating web holes into the beams. Additionally it is observed that with an increase in the size of the hole the critical distortional buckling moment decreases significantly.

Figure 3.18 illustrates the influence of web holes on distortional buckling of the 800S200-43 beams. Distortional buckling mode (D) was captured which is characterized by a single distortional half-wave in the compression flange above the hole. Due to the larger thickness of the cross-section, the D mode was not accompanied with the local half-waves in the 800S200-43 beams. Comparison of the distortional buckling modes of Figure 3.18 denotes that the distortional buckling effects are pronounced to a greater extent in the beams with larger holes (800S200-43-85-1).

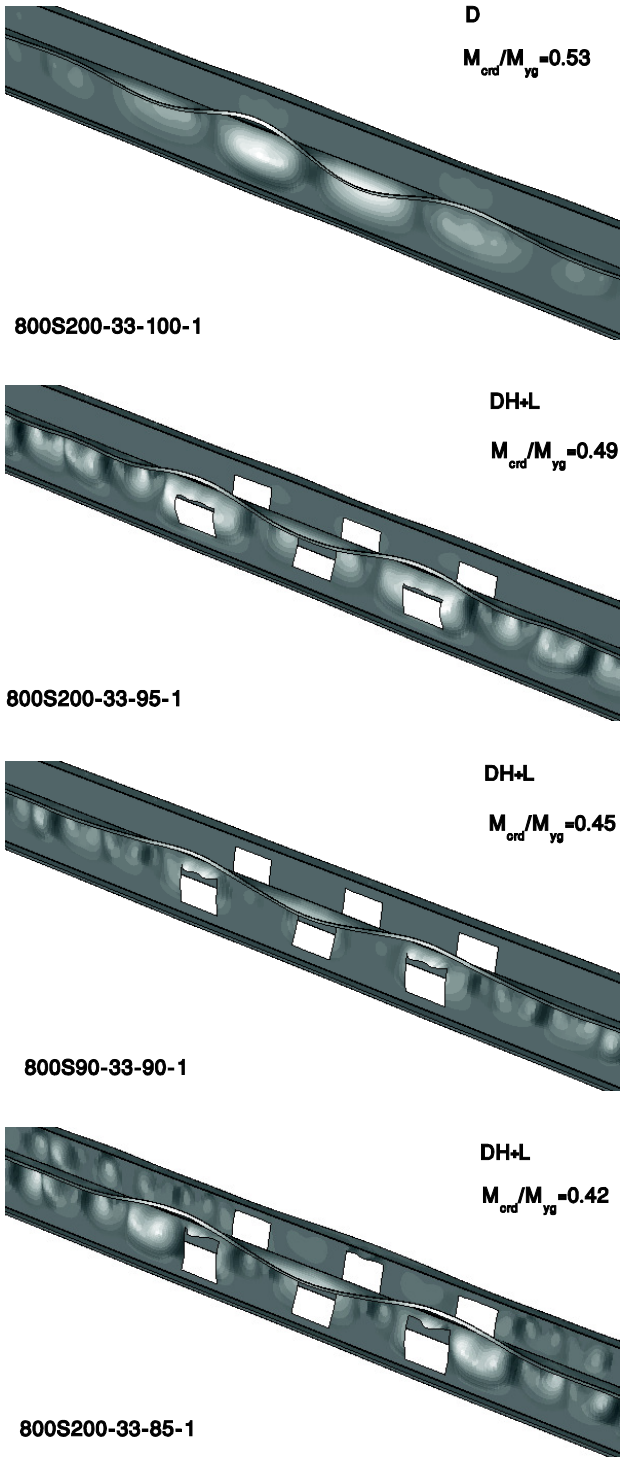

Figure 3.17. Comparison of distortional buckling modes in 800S200-33-100-1, 800S200-33-95-1, 800S200-33-90-1 and 800S200-33-85-1

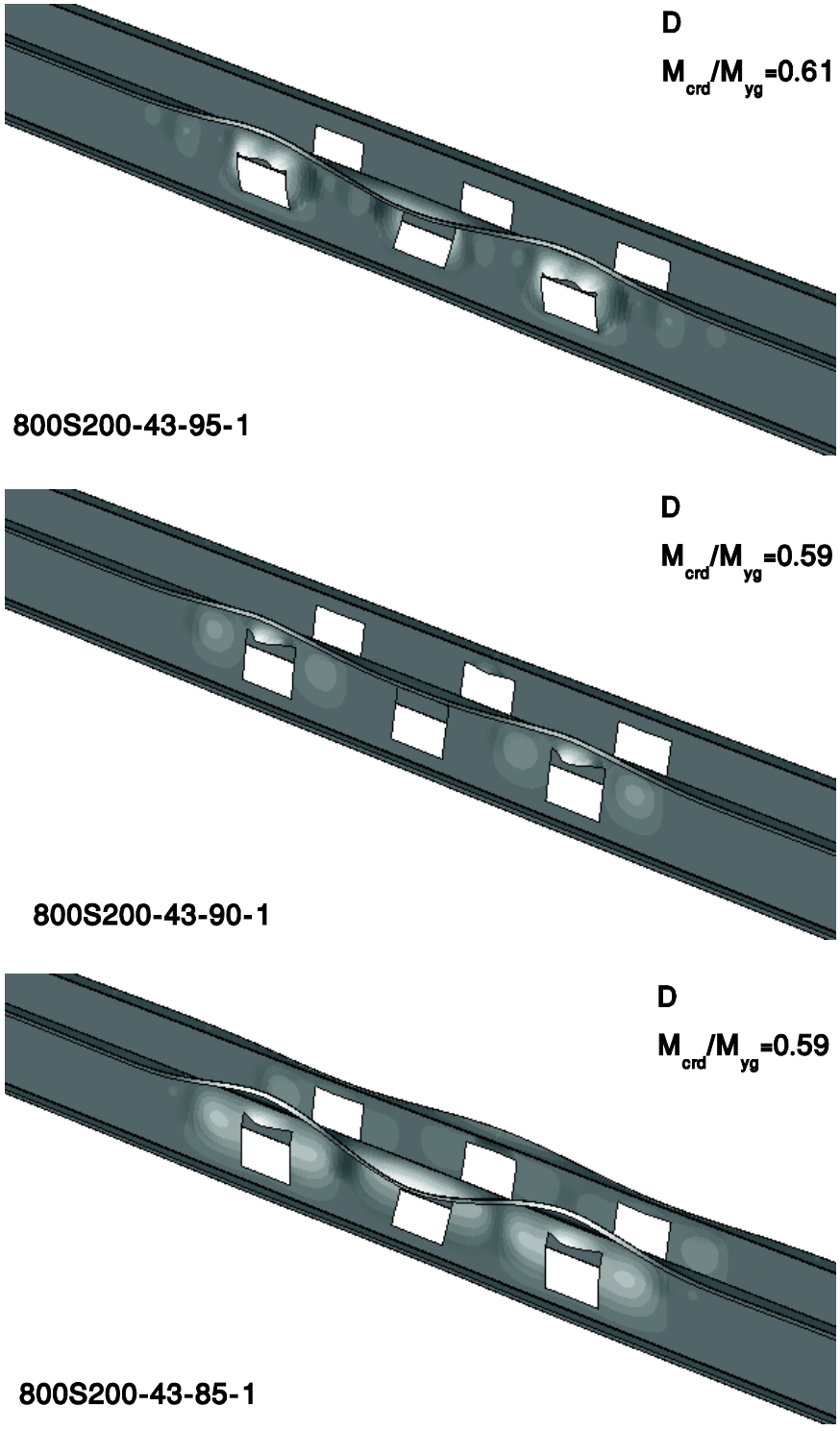

Figure 3.18. Distortional buckling modes for 800S200-43-95, 800S200-43-90 and 800S200-43-85

The distortional buckling modes captured for the hole and no-hole 1000S162-54 beams are shown in Figure 3.19. The primary distortional buckling mode observed in the no-hole 1000S162-54 beams indicates a mixing of distortional and local buckling modes (D+L). This mode is replaced with the DH+L mode for the beams with rectangular web holes. The DH+L mode is identified as distortional mode, since the buckling deformations occur primarily in the compression flange rather than the web. Investigation of the influence of holes on the critical buckling moment indicates a somewhat irregular trend in the M_{crd} values. This is due to the wavelength stiffening effects in the unstiffened strip of 1000S162-54-90-1 and 1000S162-54-85-1, which restrains the local buckling in the strip above the holes.

Figure 3.20 through Figure 3.23 illustrate the influence of web holes in the distortional buckling of the 1200S162-97 beams. A mixing of local and distortional buckling modes was observed in the behavior of the no-hole and hole beams. Three buckling modes (DH, DH2 and D+L) were identified for beams with holes. The DH2 mode is a unique distortional buckling mode, which is characterized by two local buckling half-waves in the compression flange and the unstiffened strip of the web. It is observed that The DH mode has the lowest distortional buckling moment, which implies that this mode is more likely to be observed in the experiments. Additionally it is observed that with an increase in the size of the hole, the distortional buckling moments increase substantially. This is due to the wavelength stiffening effects in the unstiffened strip above the holes.

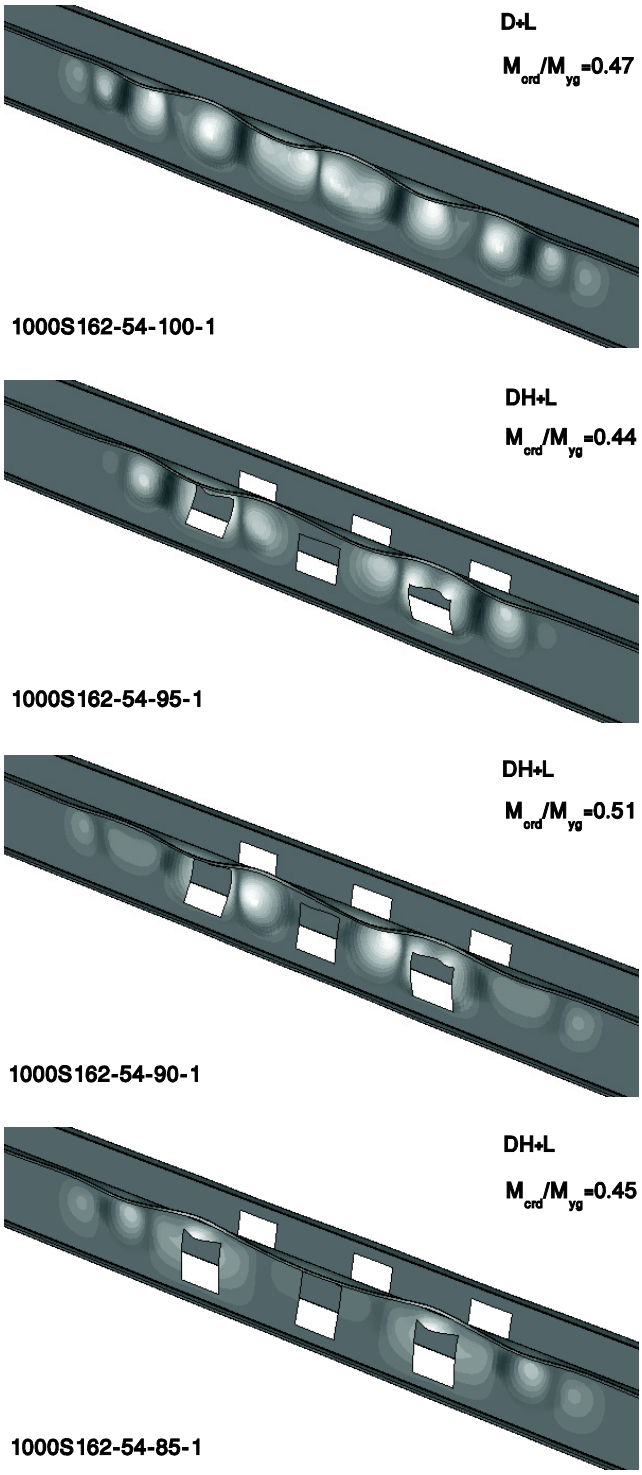

Figure 3.19. Distortional buckling modes in 1000S162-54-100-1, 1000S162-54-95-1, 1000S162-54-90-1 and 1000S162-54-85-1

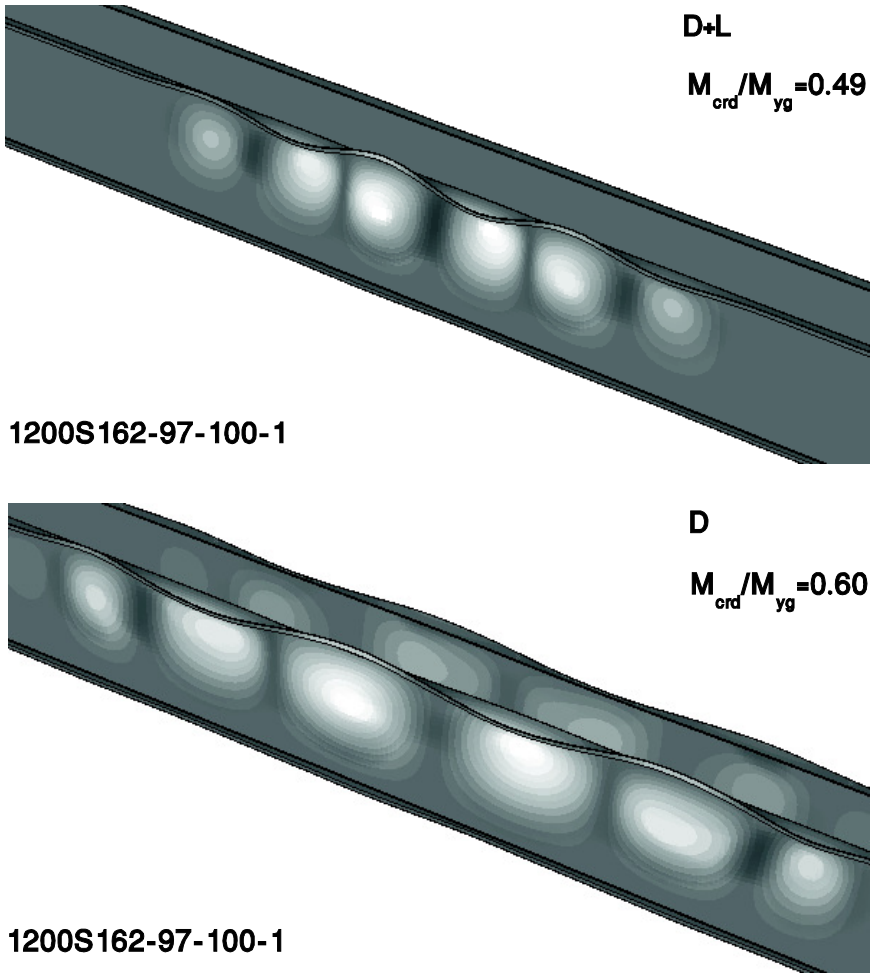

Figure 3.20. Distortional buckling modes in 1200S162-97-100-1

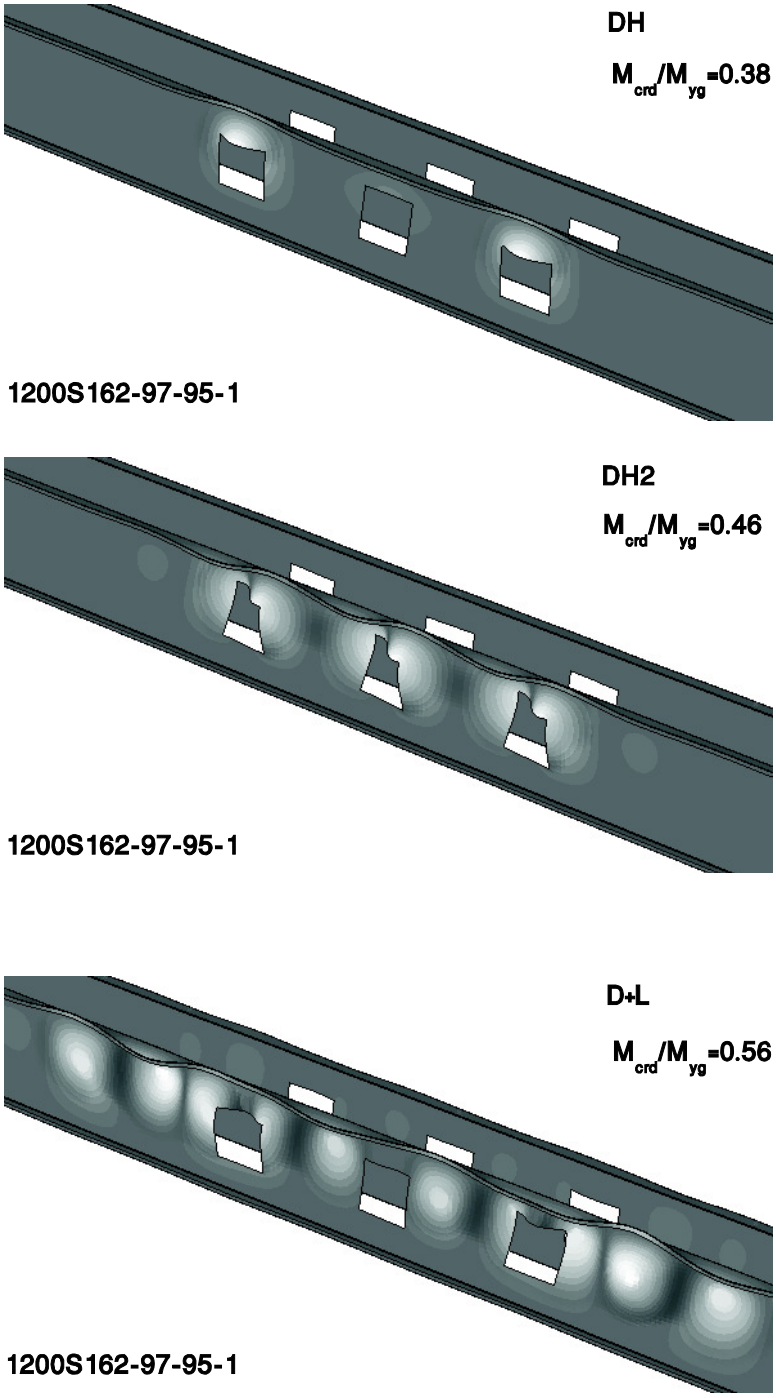

Figure 3.21. Distortional buckling modes in 1200S162-97-95-1

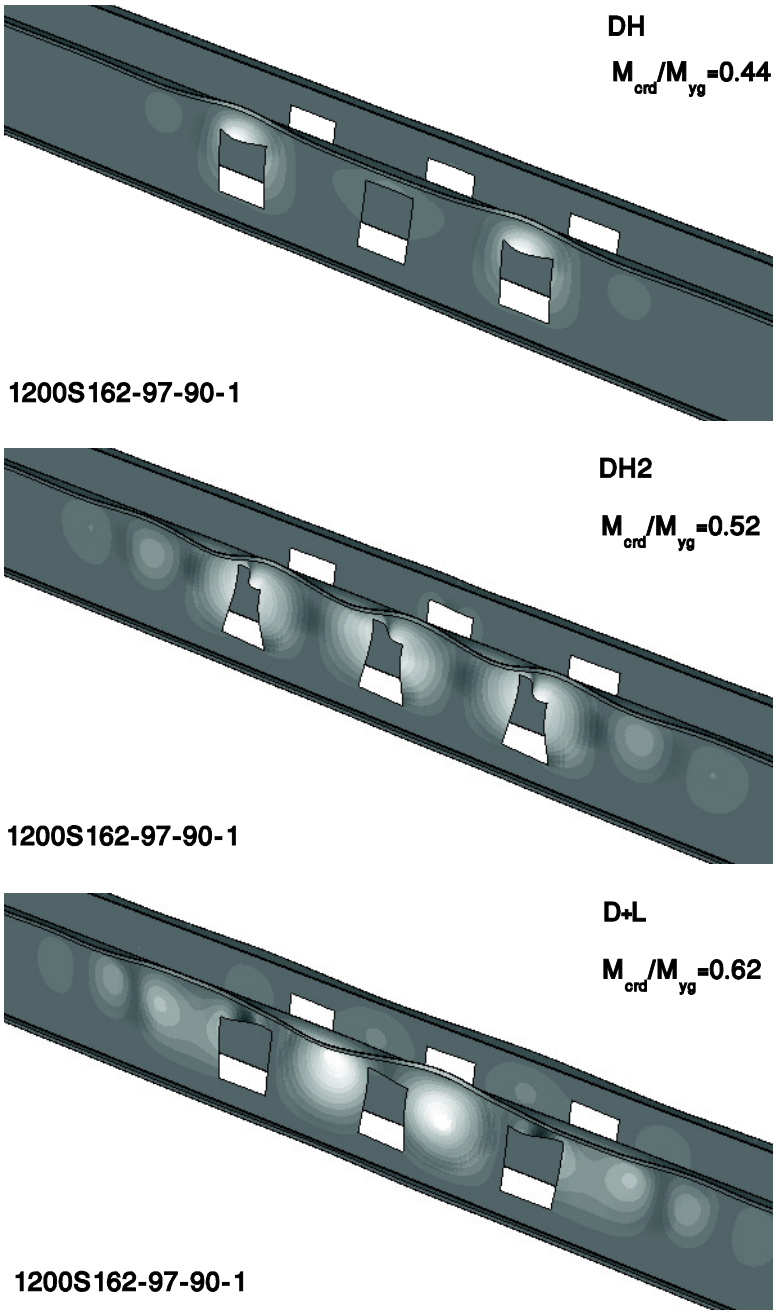

Figure 3.22. Distortional buckling modes in 1200S162-97-90-1

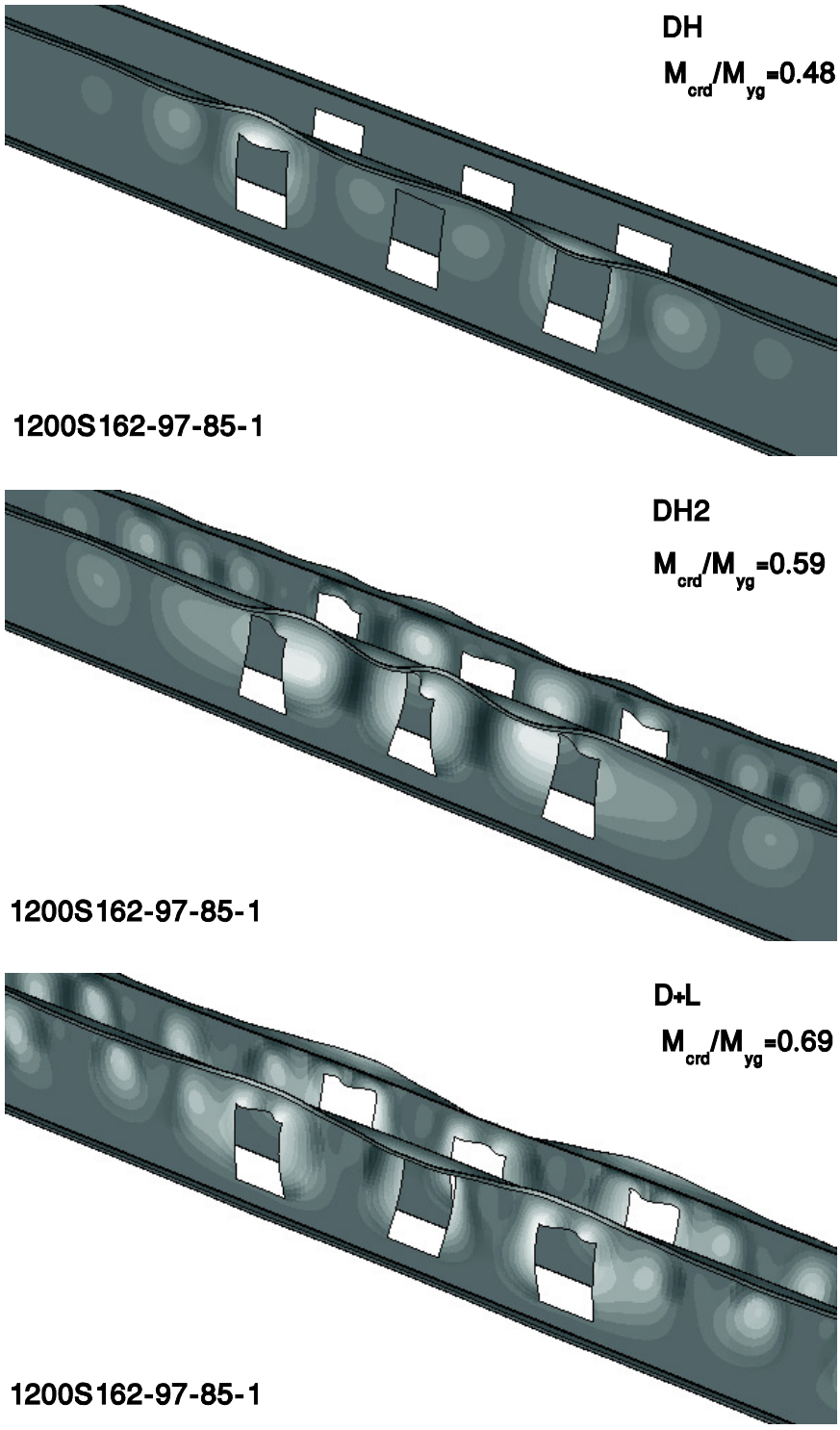

Figure 3.23. Distortional buckling modes in 1200S162-97-85-1

Investigation of the trends in the critical distortional buckling moments implies that the distortional buckling moment of 800S200-33 beams decrease with an increase in the size of the holes. A somewhat different trend is observed in the behavior of 10 in. and 12 in. beams. It is observed that for beams with small holes (I_{net}/I_g=0.95) the critical distortional buckling moments increase with an increase in the size of the holes. This is due to the interaction of local and distortional buckling modes and the wavelength stiffening effects in the unstiffened strip, which forces the local buckling half waves to appear between the holes. Investigation of the distortional buckling moments corresponding to the DH modes in 12 in. beams demonstrates that the buckling moment for beams with I_{net}/I_g=0.95 decrease comparing to the buckling moments for no hole beams while for beams with I_{net}/I_g=0.90 and I_{net}/I_g=0.85 the distortional buckling moments either increase or decrease comparing to the moments for the no hole beams.

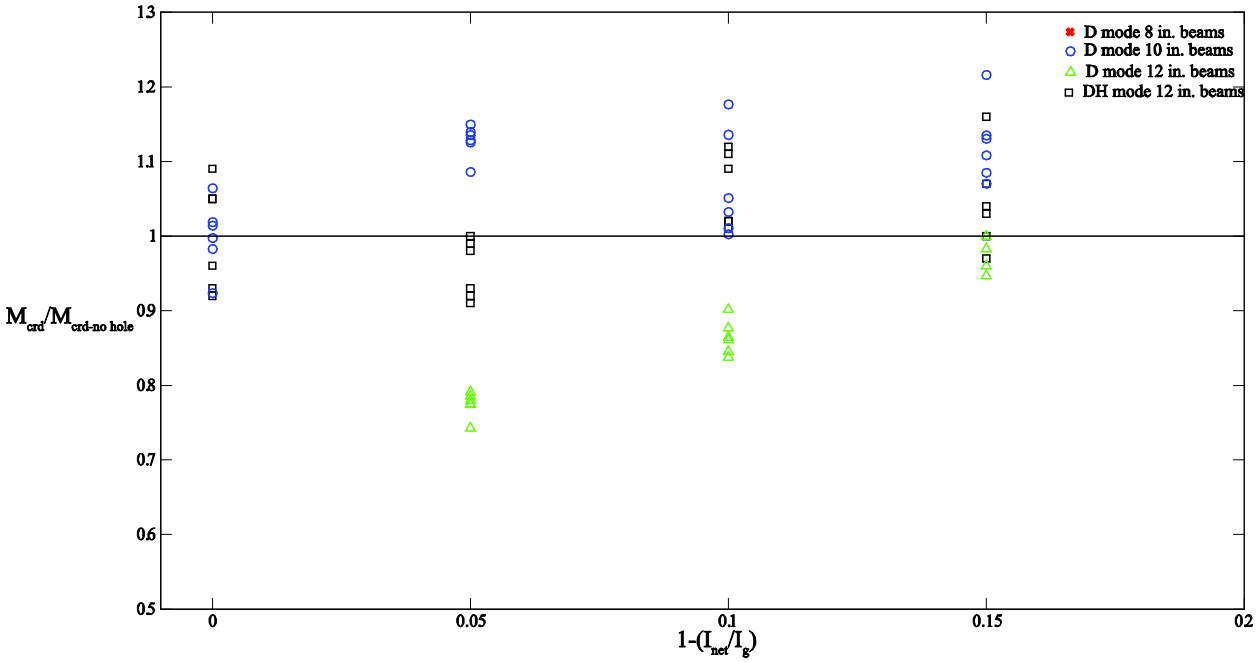

Figure 3.24. Distortional buckling moments with respect to the hole size

3.4.2.3 Lateral-torsional buckling

The lateral-torsional buckling mode often controls the capacity of the laterally unbraced beams. In this study, since the lateral-torsional buckling mode was restrained outside the constant moment region, the effects of this buckling mode was only observed in the mid-region of the beams, between the loading points (see Figure 2.8). Figure 3.25 through Figure 3.31 illustrate the influence of web holes in the lateral-torsional buckling capacity of the 800S200-33 and 800S200-43 beams. It is observed that the M_{cre} value decreases with an increasing hole depth which is consistent with recent observations by other researchers (Moen and Schafer 2009). Moreover, due to the slender cross-section, an interaction of the local and the lateral-torsional buckling mode is observed in the behavior of the 800S200-33 and 800S200-43 beams.

The lateral-torsional buckling modes for the 1000S162-54 and 1200S162-97 beams are presented in Figure 3.32 through Figure 3.39. Due to the high thickness of the cross-section, the lateral-torsional buckling mode of the 1000S162-54 and 1200S162-97 beams are less influenced by local buckling effects. A decreasing trend in the critical lateral-torsional buckling moments of all of the beams is observed with an increase in the size of the holes.

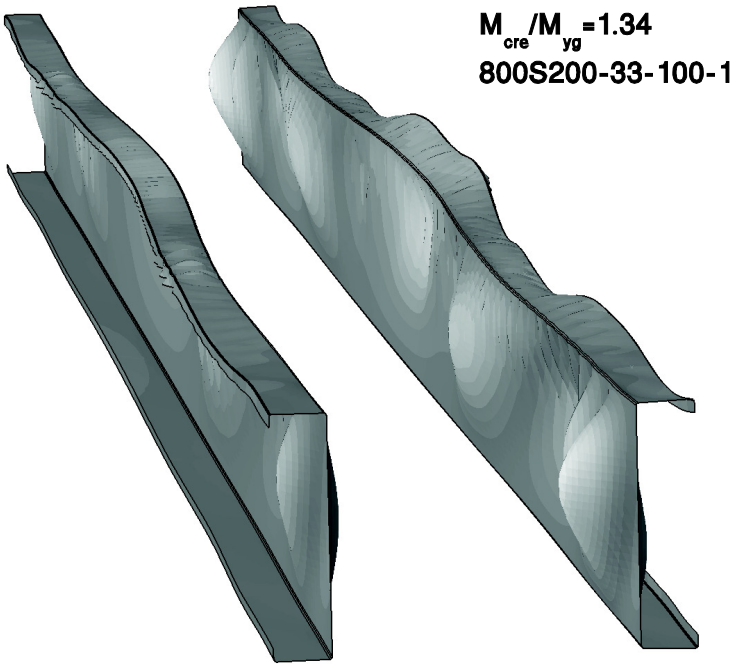

Figure 3.25. Lateral-torsional buckling in 800S200-33-100-1

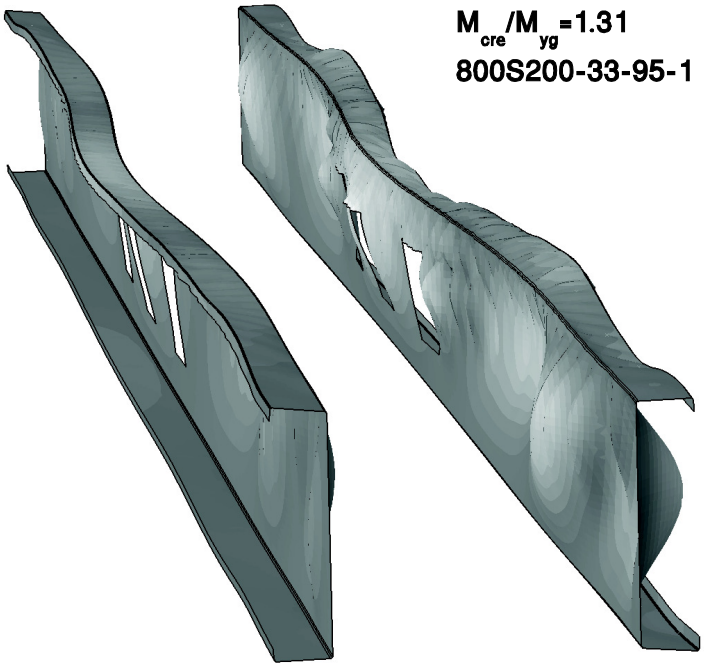

Figure 3.26. Lateral-torsional buckling in 800S200-33-95-1

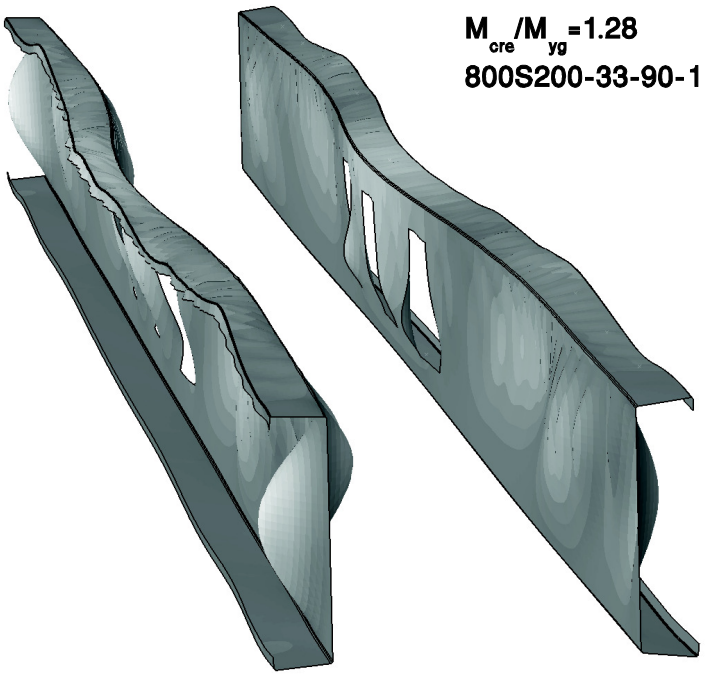

Figure 3.27. Lateral-torsional buckling in 800S200-33-90-1

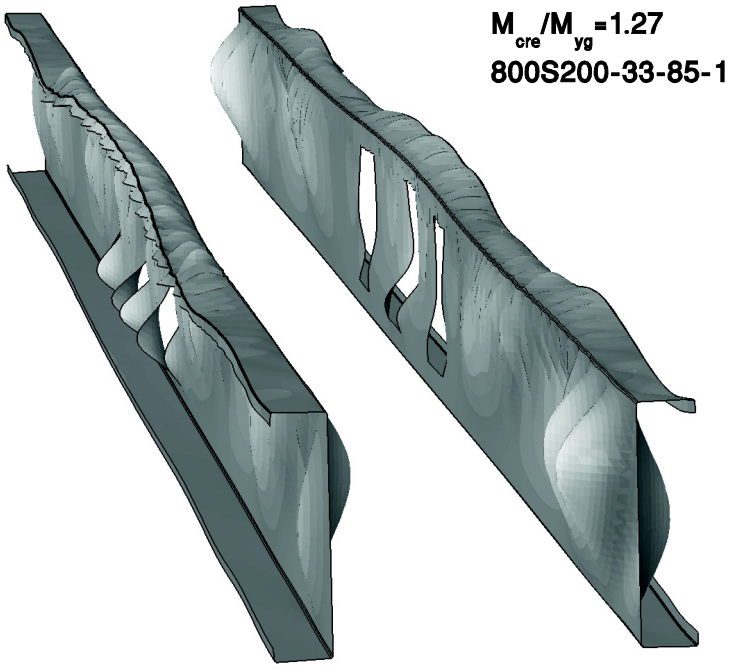

Figure 3.28. Lateral-torsional buckling in 800S200-33-85-1

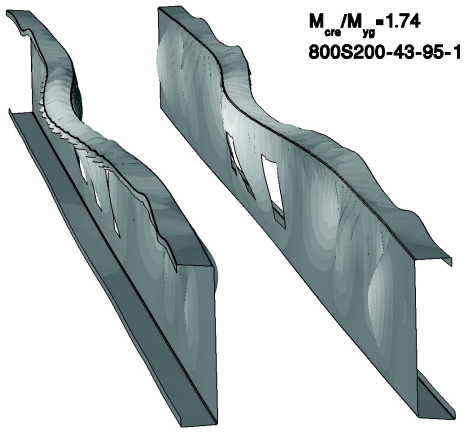

Figure 3.29. Lateral-torsional buckling in 800S200-43-95-1

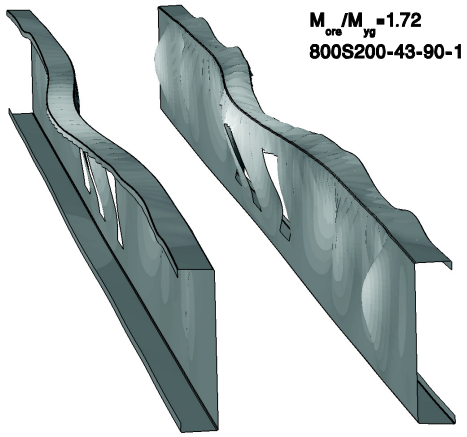

Figure 3.30. Lateral-torsional buckling in 800S200-43-90-1

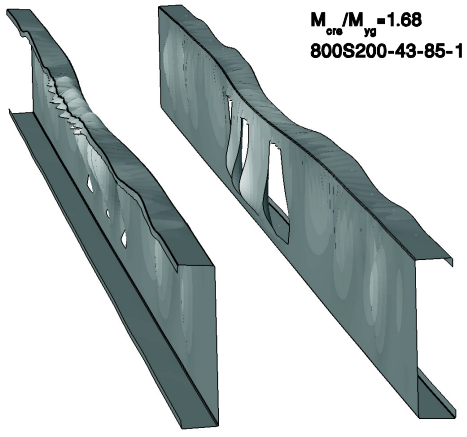

Figure 3.31. Lateral-torsional buckling in 800S200-43-85-1

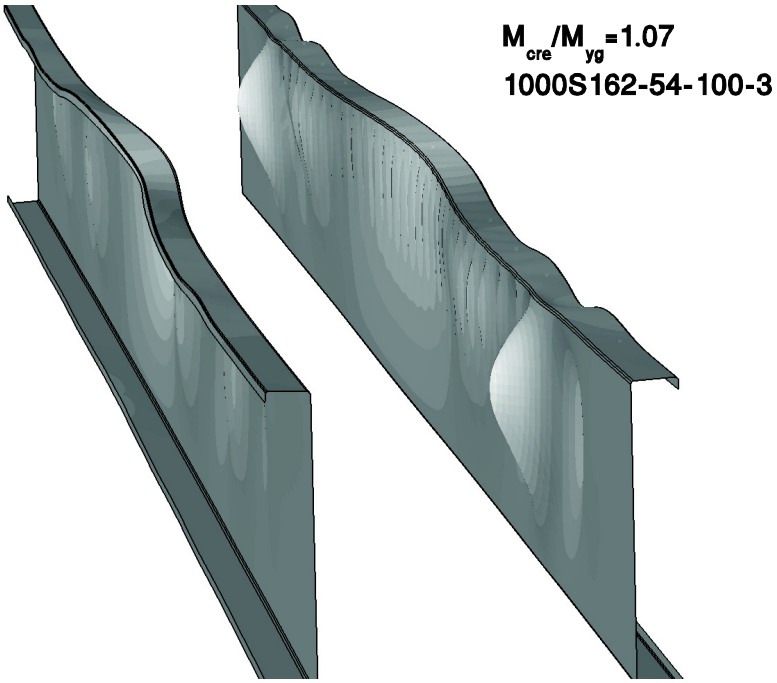

Figure 3.32. Lateral-torsional buckling in 1000S162-54-100-3

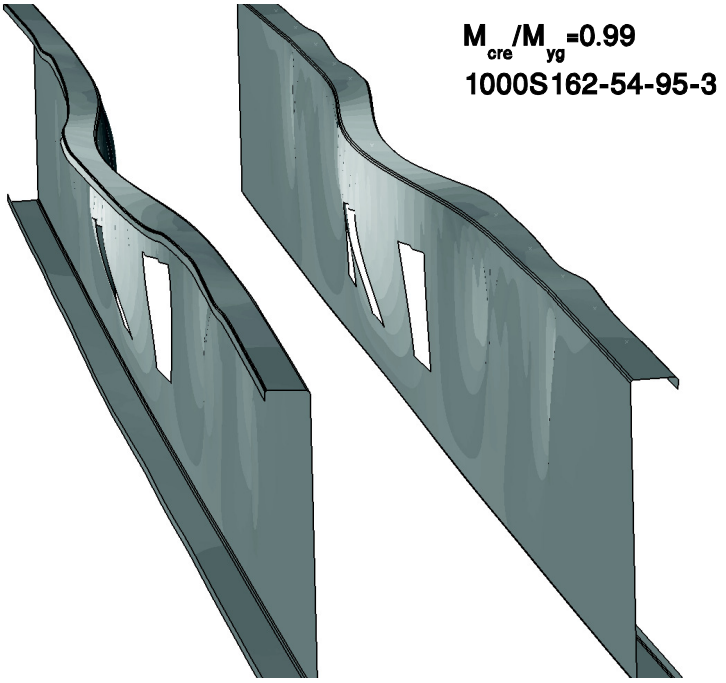

Figure 3.33. Lateral-torsional buckling in 1000S162-54-95-3

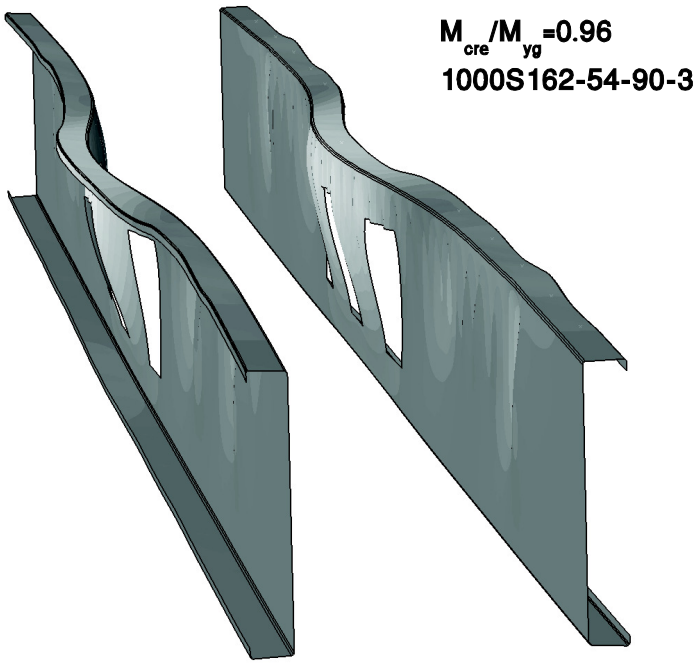

Figure 3.34. Lateral-torsional buckling in 1000S162-54-90-3

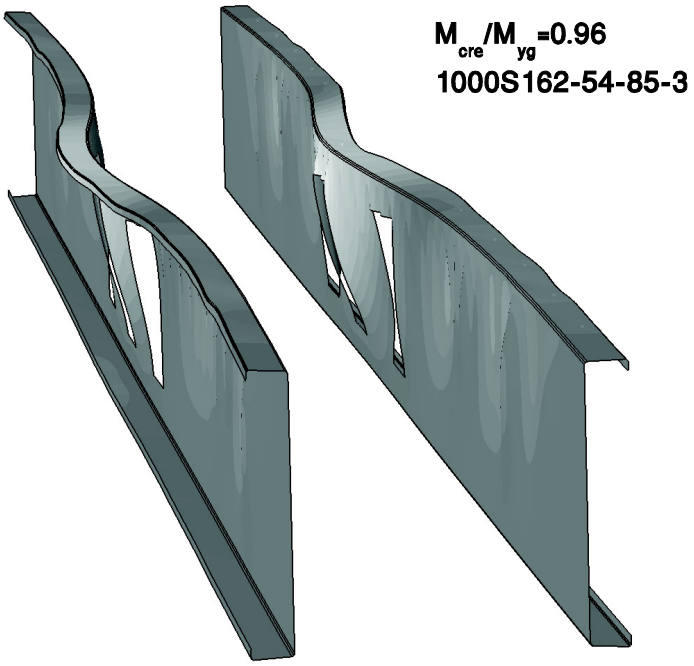

Figure 3.35. Lateral-torsional buckling in 1000S162-54-85-3

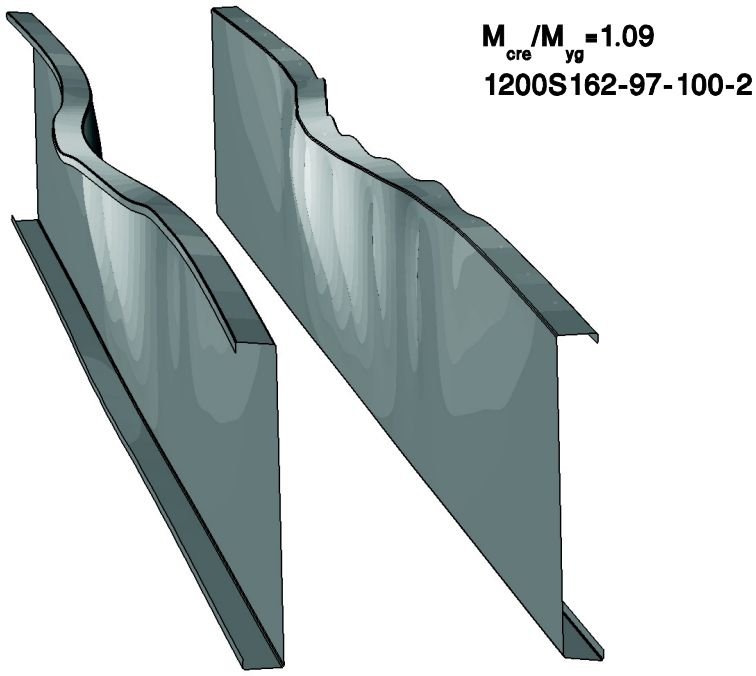

Figure 3.36. Lateral-torsional buckling in 1200S162-97-100-2

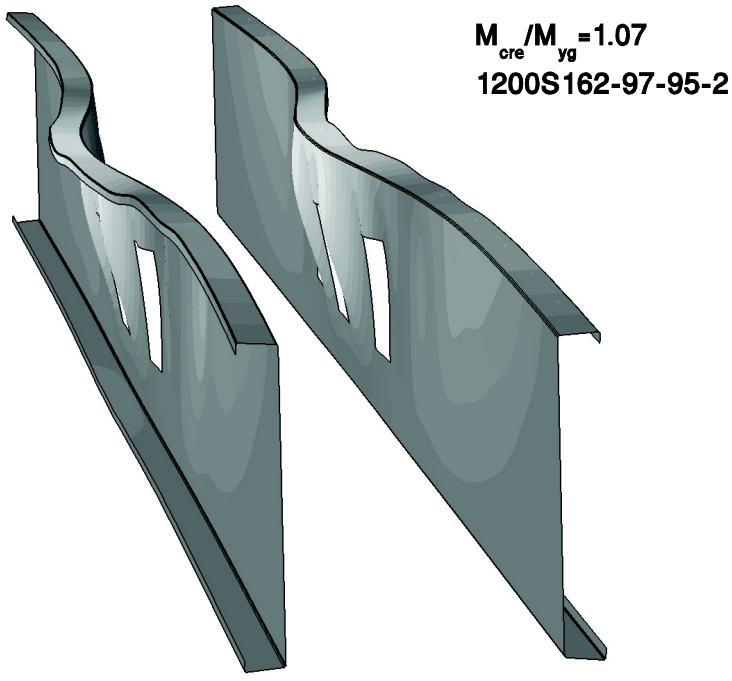

Figure 3.37. Lateral-torsional buckling in 1200S162-97-95-2

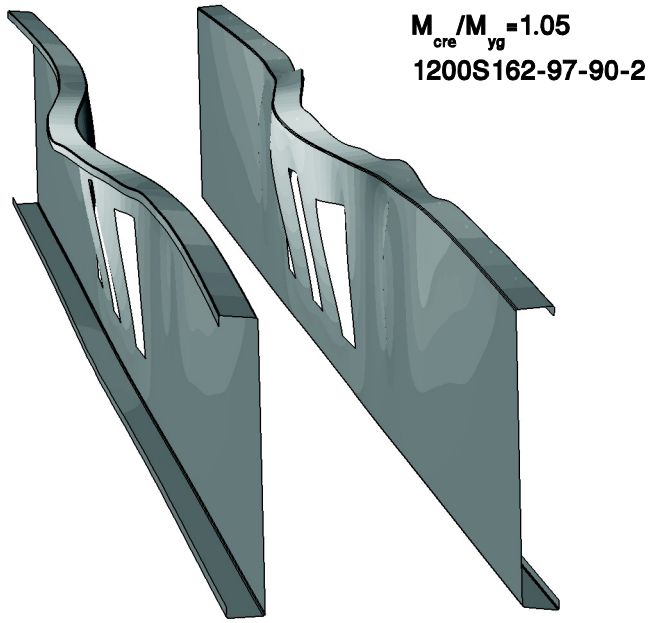

Figure 3.38. Lateral-torsional buckling in 1200S162-97-90-2

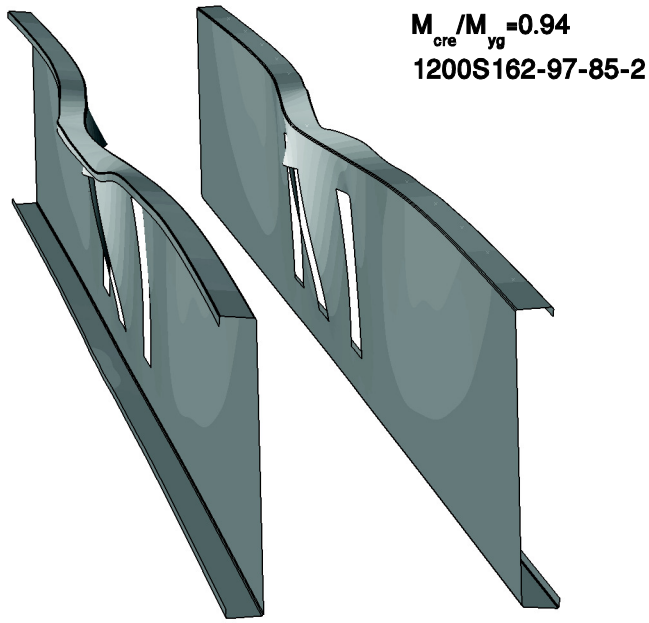

Figure 3.39. Lateral-torsional buckling in 1200S162-97-85-2

The buckling mode shapes and the corresponding moments identified and observed in this chapter are used and discussed in the next chapter summarizing the experimental results.

Chapter 4. Experimental results

In this chapter experimental results achieved through the testing program are presented. The critical buckling modes are identified for each set of beams and the corresponding mode shapes and the applied loads are compared to the elastic buckling results presented in Chapter 3.

4.1 800S200-33 cross-sections

Local buckling was the first mode that appeared as a single half sine wave in the unstiffened strips above the holes (LH mode) at the load of about 0.45 kN (0.1 kips). As the load increased to 0.31 kN (0.7 kips) half sine waves formed between the holes as well (L mode). The 800S200-33 local half waves are shown in Figure 4.1. It is observed that the local buckling modes emerged in the beams are similar to the local buckling modes captured in the elastic buckling study of the beams shown in Figure 3.5.

Figure 4.1. Local buckling in the unstiffened strip and between holes

When the applied load reached 0.62 kN (1.4 kips), distortional buckling half-waves appeared in the compression flange of the beam, causing the flange to rotate around the

flange/web junction as shown in Figure 4.2. Comparing the local and distortional buckling modes, it is observed that the distortional half-waves exhibit a visibly longer wavelength than the local buckling half-waves, which is consistent with the results achieved from eigen-buckling analysis. The rotation of the compression flange is accompanied by an increase in the outermost compressive fiber stresses in the C-section lip until failure occurs in the middle-region of the beam. The buckling modes and their interaction appearing at the failure instant are shown in Figure 4.3. It is observed that distortional buckling is the dominant mode, causing the failure of the 800S200-33 beams. Investigation of the influence of web holes on the behavior of the 800S200-33 beams suggests that the specimens with deeper holes do not exhibit the unstiffened strip local buckling mode (LH). This trend is caused by the reduced size of the unstiffened strip above the hole, which in turn increases the critical local buckling stress of the unstiffened strip above the hole (wavelength stiffening) as was investigated by Moen and Schafer (2009).

Figure 4.2. Distortional buckling of the compression flange (beam 800S200-33-95-3-2)

Figure 4.3. Distortional buckling failure

The load-displacement behavior of a typical group of 800S200-33 beams are provided in Figure 4.4. Analysis of plots indicates a sudden failure of the specimen cross-sections. This is due to the fact that the weaker beam in each specimen initiated the failure causing a significant loss in the capacity of the specimen, followed by the failure of the second beam in the pair. The trend observed in the behavior of beams with different hole depths indicate that the general capacity of C-section beams reduce with an increase in the web-hole dimensions. Knowing that the distortional buckling mode is the dominant mode triggering the failure of the 800S200-33 beams, it is observed that the influence of the holes in the experiments is identical to the effects seen in the distortional buckling modes in the eigen-buckling analysis. The tested capacity of 800S200-33 beams are provided in Table 4.1. The strength of the beam specimens is observed to decrease with respect to the no hole beams by about 1, 6 and 9 percent for beams with I_{net}/I_g equal to 0.95, 0.90 and 0.85 respectively.

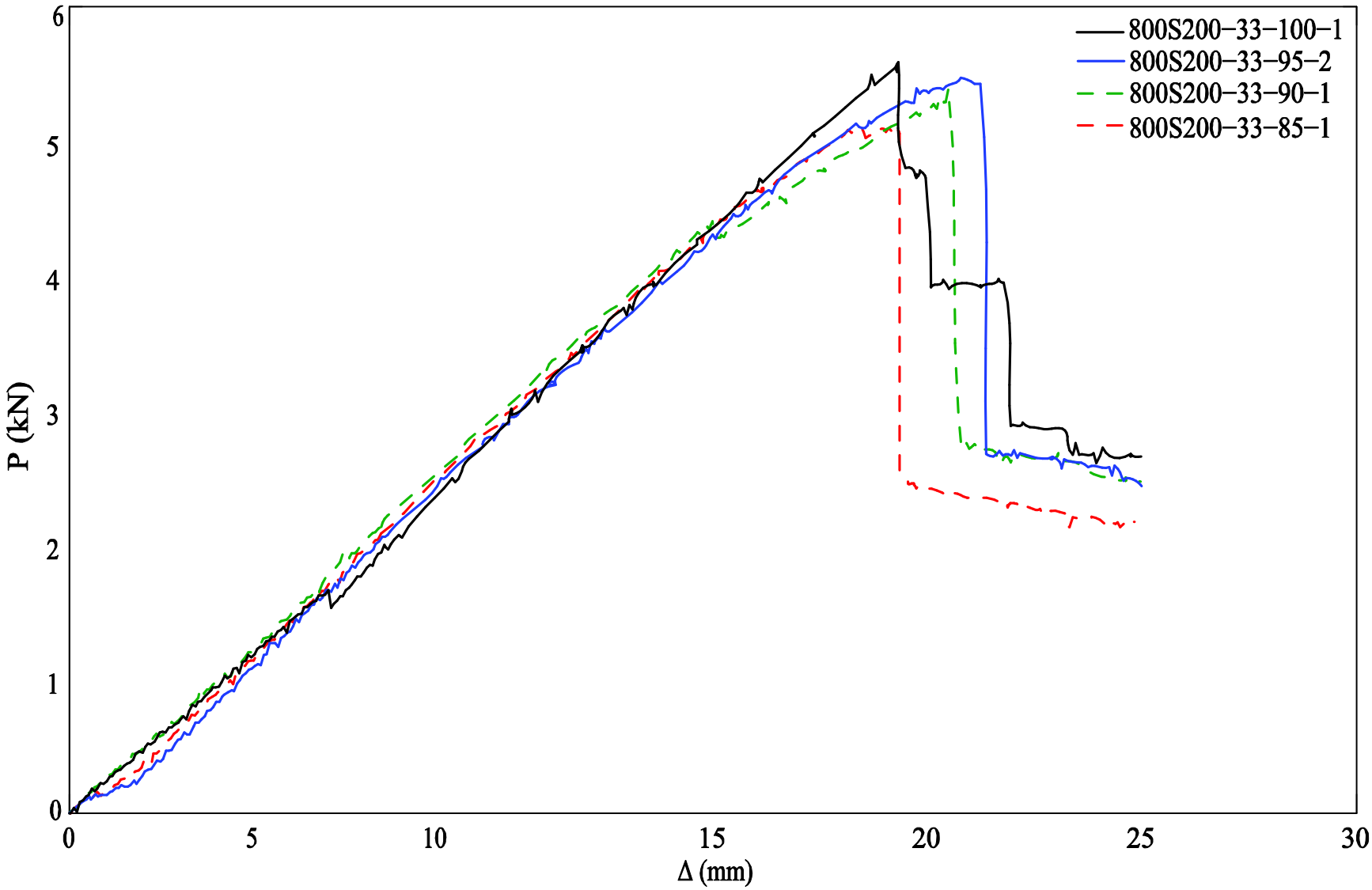

Figure 4.4. Load-displacement response of the 800S200-33 beams

Table 4.1 Tested capacities of the 800S200-33 beams

Beam Name	M_{test}	M_{test} avg	SD	COV
	(kN-m)	(kN-m)	(kN-m)	%
800 S 200-33-100-1-1	6.01	5.85	0.15	2.63
800 S 200-33-100-1-2				
800 S 200-33-100-2-1	5.70			
800 S 200-33-100-2-2				
800 S 200-33-95-1-1	5.63	5.79	0.15	2.62
800 S 200-33-95-1-2				
800 S 200-33-95-2-1	5.94			
800 S 200-33-95-2-2				
800 S 200-33-90-1-1	5.77	5.49	0.28	5.07
800 S 200-33-90-1-2				
800 S 200-33-90-2-1	5.22			
800 S 200-33-90-2-2				
800 S 200-33-85-1-1	5.59	5.35	0.24	4.43
800 S 200-33-85-1-2				
800 S 200-33-85-2-1	5.11			
800 S 200-33-85-2-2				

4.2 800S200-43 cross-sections

The buckling modes observed in the 800S200-43 beams were similar to the modes that appeared in 800S200-33 beams with an exception of less local half-waves due to the higher thickness of the cross section. The load-displacement response of the 800S200-43 beams (Figure 4.5) indicates that the strength of the beam specimens increase with an increasing hole depth, but the small number of specimens disallows definitive conclusions. The tested capacity of the 800S200-43 beams are presented in Table 4.2.

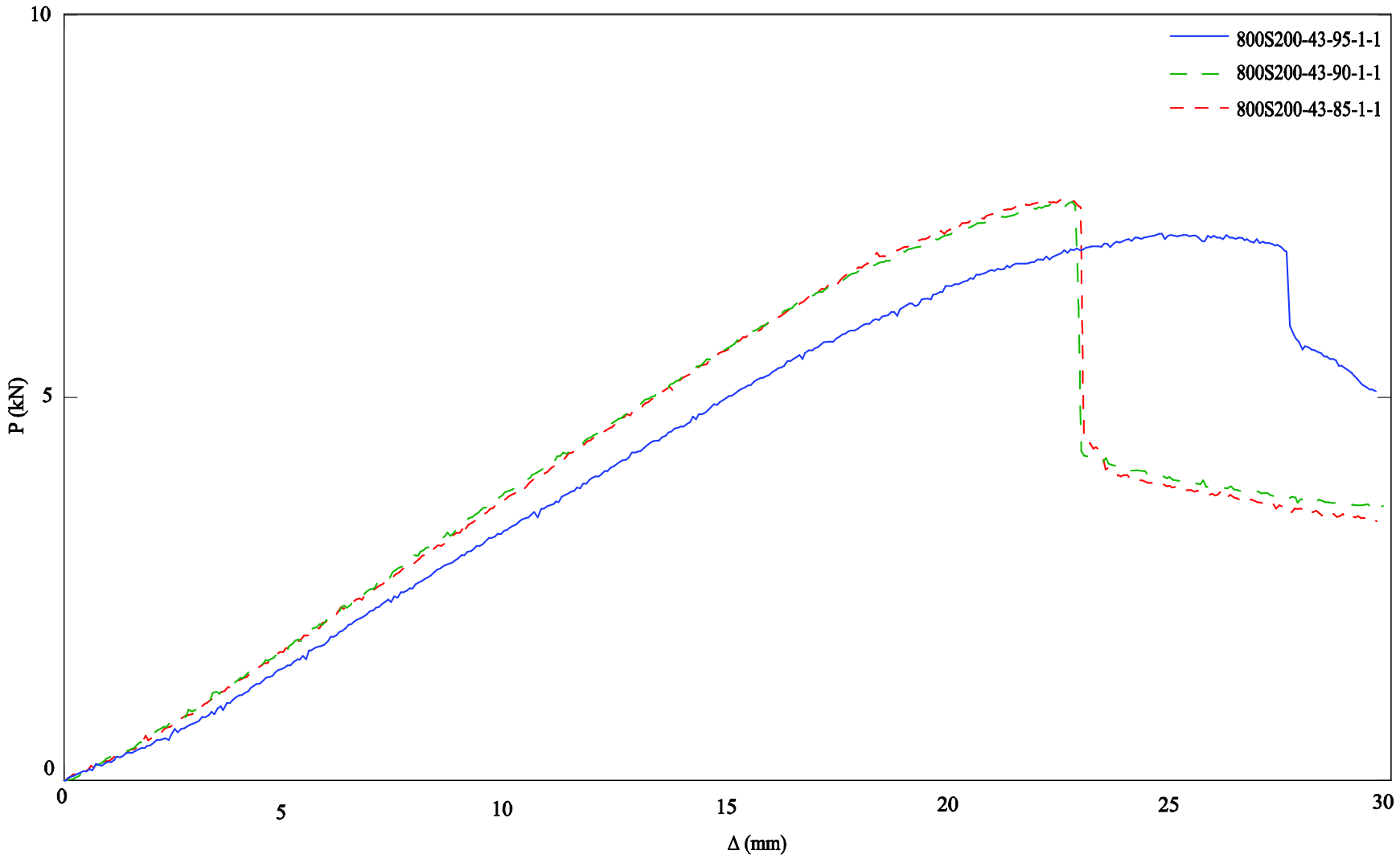

Figure 4.5. Load-displacement of the 800S200-43 beams

Table 4.2 Tested capacities of the 800S200-43 beams

Beam Name	M_{test} (kN.m)
800 S 200-43-95-1-1	8.19
800 S 200-43-95-1-2	
800 S 200-43-90-1-1	8.57
800 S 200-43-90-1-2	
800 S 200-43-85-1-1	8.60
800 S 200-43-85-1-2	

4.3 1000S162-54 cross-sections

The buckling modes captured in the 1000S162-54 beams were dependent upon the size of the holes as well as the thickness of the cross-section. Local half-waves were the first buckling modes observed in the unstiffened strip above the hole of the 1000S162-54-95 beams with relatively small web holes as shown in Figure 4.6. This was followed by a series of distortional half-waves appearing in the compression flange of the beam. Observations show that the failure mechanism of the no hole and the 1000S162-54-95 beams are similar to the behavior of the 800S200-33 and 800S200-43 beams (see Section 2.8.1 and 2.8.2). This means that the failure was triggered by local buckling of the unstiffened strip followed by the distortional half-waves appearing in the compression flange, above the hole, leading the beams to failure. This behavior is graphically illustrated in Figure 4.7.

Figure 4.6. Unstiffened strip local buckling in 1000S162-54-95-1

Figure 4.7. Distortional buckling in 1000S162-54-95-1

A somewhat different behavior was observed in the 1000S162-54-90 and 1000S162-54-85 beams, where the failure mode was comprised solely of distortional buckling half-waves in the compression flange of the beams. This takes place due to the reduced size of the unstiffened strip, which restrains the local buckling modes. This behavior is illustrated in Figure 4.8. It is observed that at about 85 percent of the peak moment, distortional half-waves appear in the compression flange which lead the specimen to failure at about M_{test}=5.95 kN.m.

M_{test}=1.30 kN.m
$M_{cr\ell}$=6.27 kN.m

M_{test}=4.20 kN.m
M_{crd}=5.68 kN.m

M_{test}=5.95 kN.m
M_{cre}=10.37 kN.m

Figure 4.8. Load-displacement progression of 1000S162-54-85-1 beam with I_{net}/I_g=0.85

The load-displacement response of a typical group of 1000S162-54 beams with varying I_{net}/I_g is presented in Figure 4.9. A reduction in the tested capacity of the beams is observed with an increase in the size of the holes. This is in a good agreement with the elastic distortional buckling behavior of the 1000S162-54 beams (see Section 3.4.2.2) since the distortional buckling mode was observed to be the failure mode in the experiments. Additionally the post-peak ductility is observed to reduce with an increase in the size of the holes.

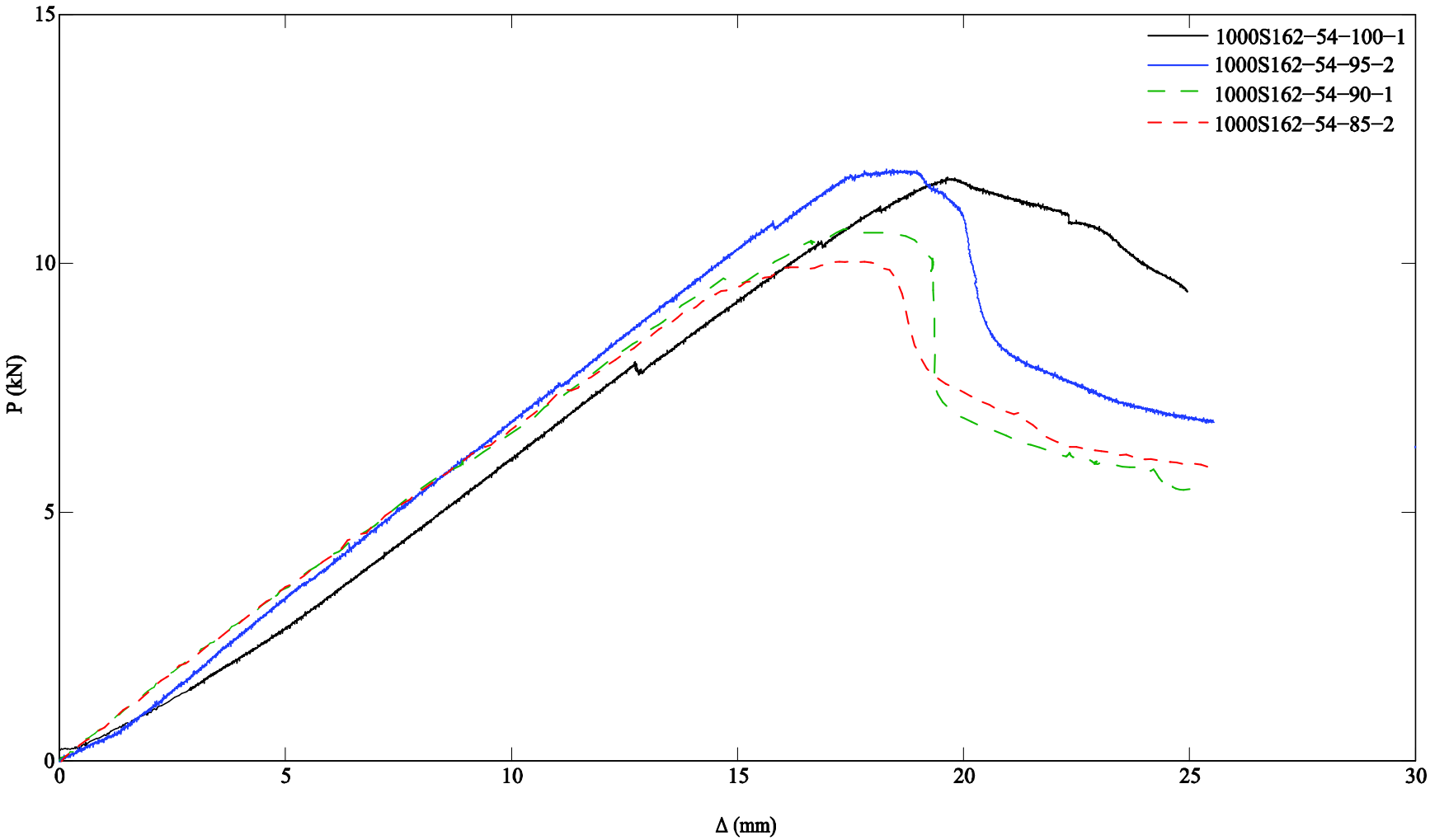

Figure 4.9. Typical load-displacement response of 1000S162-54 beams

Table 4.3 Tested Capacities of the 1000S162-54 beams

Beam Name	M_{test}	M_{test} avg	SD	COV
	(kN-m)	(kN-m)	(kN-m)	%
1000 S 162-54-100-1-1	10.69	10.00	0.51	5.14
1000 S 162-54-100-1-2				
1000 S 162-54-100-2-1	9.46			
1000 S 162-54-100-2-2				
1000 S 162-54-100-3-1	9.84			
1000 S 162-54-100-3-2				
1000 S 162-54-95-1-1	12.78	11.88	0.72	6.07
1000 S 162-54-95-1-2				
1000 S 162-54-95-2-1	11.02			
1000 S 162-54-95-2-2				
1000 S 162-54-95-3-1	11.82			
1000 S 162-54-95-3-2				
1000 S 162-54-90-1-1	10.06	10.24	0.32	3.08
1000 S 162-54-90-1-2				
1000 S 162-54-90-2-1	10.68			
1000 S 162-54-90-2-2				
1000 S 162-54-90-3-1	9.98			
1000 S 162-54-90-3-2				
1000 S 162-54-85-1-1	11.25	10.26	0.71	6.94
1000 S 162-54-85-1-2				
1000 S 162-54-85-2-1	9.59			
1000 S 162-54-85-2-2				
1000 S 162-54-85-3-1	9.94			
1000 S 162-54-85-3-2				

4.4 1200S162-97 cross-sections

The buckling behavior of the 1200S162-97 beams was different from the 1000S162-54, 800S200-33 and 800S200-43 beams and was characterized by a minor distortional buckling in the compression flange accompanied by the lateral-torsional buckling of the beams. The load-displacement progression of a perforated 1200S162-97 beam is shown in Figure 4.10. It is observed that the local buckling mode is limited due to the low local buckling slenderness of the cross-section. The lateral-torsional buckling was the first mode, which became noticeable at about 0.75 of the peak moment. This was followed by a series of distortional half-waves, which emerged preceding the failure of the beam. The tested capacities of the 1200S162-97 beams are presented in Table 4.4. The highest and lowest variation in the tested capacity of the beams is observed in the beams with I_{net}/I_g=0.90 and I_{net}/I_g=0.95 respectively.

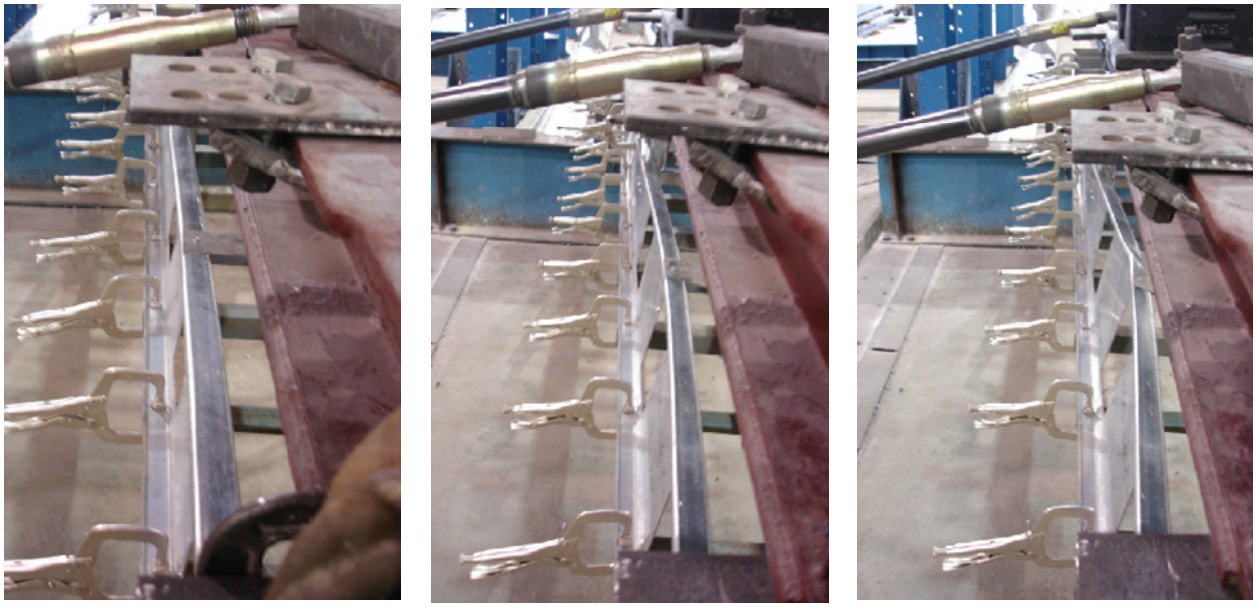

M=0.9 kN-m M=9.9 kN-m M=12.6 kN-m

Figure 4.10 Load-displacement progression of 1200S162-97-90-1

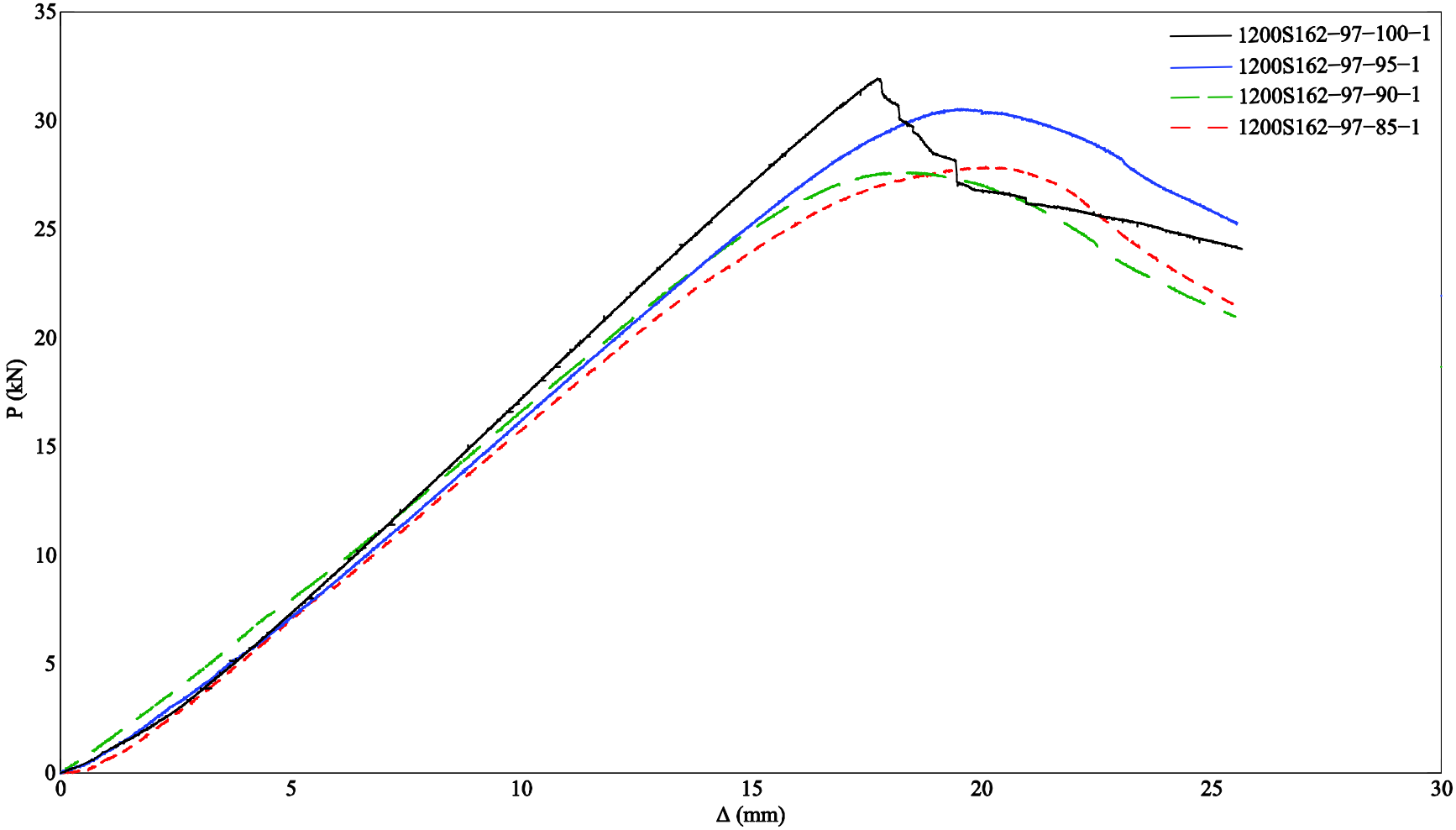

Figure 4.11. Load-displacement response of 1200S162-97 beams

Table 4.4 Tested Capacities of the 1200S162-97 beams

Beam Name	M_{test}	M_{test} avg	SD	COV
	(kN-m)	(kN-m)	(kN-m)	%
1200 S 162-97-100-1-1	31.19	32.22	2.15	6.66
1200 S 162-97-100-1-2				
1200 S 162-97-100-2-1	30.27			
1200 S 162-97-100-2-2				
1200 S 162-97-100-3-1	35.21			
1200 S 162-97-100-3-2				
1200 S 162-97-95-1-1	29.73	29.47	0.19	0.63
1200 S 162-97-95-1-2				
1200 S 162-97-95-2-1	29.31			
1200 S 162-97-95-2-2				
1200 S 162-97-95-3-1	29.37			
1200 S 162-97-95-3-2				
1200 S 162-97-90-1-1	26.98	26.68	1.80	6.76
1200 S 162-97-90-1-2				
1200 S 162-97-90-2	24.34			
1200 S 162-97-90-2				
1200 S 162-97-90-3-1	28.73			
1200 S 162-97-90-3-2				
1200 S 162-97-85-1-1	27.78	27.42	0.26	0.94
1200 S 162-97-85-1-2				
1200 S 162-97-85-2-1	27.27			
1200 S 162-97-85-2-2				
1200 S 162-97-85-3-1	27.21			
1200 S 162-97-85-3-2				

Chapter 5. Direct Strength Method for cold-formed steel members with holes

5.1 DSM for beams with hole

The elastic buckling results presented in Chapter 2 are employed to evaluate the modified DSM equations proposed by Moen (2008) for the cold-formed steel beams with pre-punched web holes. A comparison of the experimental data and the estimated capacity using the modified DSM method is provided. The modified DSM method limits the local and distortional buckling capacity of the beam to the capacity of the net section, M_{ynet}.

Lateral-torsional buckling

The nominal flexural strength, M_{ne}, for lateral-torsional buckling shall be calculated in accordance with the following:

(a) For $M_{cre} < 0.56M_y$ $\quad M_{ne} = M_{cre}$

(b) For $2.78M_y \geq M_{cre} \geq 0.56M_y$ $\quad M_{ne} = \frac{10}{9}M_y\left(1 - \frac{10M_y}{36M_{cre}}\right)$

(c) For $M_{cre} > 2.78M_y$ $\quad M_{ne} = M_y$

where

M_{cre} = critical elastic lateral-torsional buckling load

Local buckling

The nominal flexural strength, $M_{n\ell}$, for local buckling shall be calculated in accordance with the following:

(a) For $\lambda_\ell \leq 0.776$

$$M_{n\ell} = M_{ne} \leq M_{ynet}$$

(b) For $\lambda_\ell > 0.776$

$$M_{n\ell} = \left(1 - 0.15\left(\frac{M_{cr\ell}}{M_{ne}}\right)^{0.4}\right)\left(\frac{M_{cr\ell}}{M_{ne}}\right)^{0.4} M_{ne}$$

where

$\lambda_\ell = \sqrt{M_{ne}/M_{cr\ell}}$

$M_{cr\ell}$ = critical elastic local buckling moment including hole(s)

M_{ne} = defined in section above

$M_{ynet} = S_{fnet} f_y$

S_{fnet} = section modulus at the hole referenced to the extreme fiber at yield

f_y = yield stress of the beam

Distortional buckling

The nominal flexural strength, M_{nd}, for distortional buckling shall be calculated in accordance with the following:

(a) For $\lambda_d \le \lambda_{d1}$

$$M_{nd} = M_{ynet}$$

(b) For $\lambda_{d1} \le \lambda_d < \lambda_{d2}$

$$M_{nd} = M_{ynet} - \left(\frac{M_{ynet} - M_{d2}}{\lambda_{d2} - \lambda_{d1}}\right)\left(\lambda_d - \lambda_{d1}\right)$$

(c) For $\lambda_d > \lambda_{d2}$

$$M_{nd} = \left(1 - 0.22\left(\frac{M_{crd}}{M_y}\right)^{0.5}\right)\left(\frac{M_{crd}}{M_y}\right)^{0.5} M_y$$

where

$$\lambda_d = \sqrt{\frac{M_y}{M_{crd}}}$$

$$\lambda_{d1} = 0.673\left(\frac{M_{ynet}}{M_y}\right)$$

$$\lambda_{d2} = 0.673\left(1.7\left(\frac{M_y}{M_{ynet}}\right)^{-1.7} - 0.7\right)$$

$$M_{d2} = \left(1 - 0.22\left(\frac{1}{\lambda_{d2}}\right)\right)\left(\frac{1}{\lambda_{d2}}\right)M_y$$

$$M_{ynet} = S_{fnet} f_y$$

S_{fnet} = section modulus at the hole(s) referenced to the extreme fiber at yield

M_{crd} = critical elastic distortional beam buckling load including hole(s)

The linear portion of the distortional buckling equations where $\lambda_{d1}<\lambda_d\leq\lambda_{d2}$, denotes a transition from the elastic buckling regime to the inelastic regime and failure at the net section (Moen 2008).

5.2 DSM comparison to experimental results

The modified DSM results are compared against the tested capacity of the beams while investigating data trends against hole size and member slenderness. The M_{test}/M_n ratio was employed for the comparisons where M_{test} represents the tested capacity of the beams and M_n is the nominal predicted strength using DSM. The DSM predicted capacities of the 800S200-33 and 800S200-43 beams, as well as the experimental data for each cross-section, is provided in Table 5.1 and Table 5.2. Investigation of the DSM results demonstrates that local buckling is the predicted failure mode of the 800S200-33 beams with I_{net}/I_g=0.95 as well as the no hole beams while distortional buckling mode is predicted to govern the strength of the beams with larger holes. Comparing these failure modes with the modes identified in the experiments indicates that the DSM estimates the governing buckling modes with an acceptable accuracy. Investigation of

the influence of holes on the test-to-predicted capacities (Figure 5.1) indicates a decreasing trend in the test-to-predicted ratio with an increase in hole depth. Additionally, it is observed that the tested capacity of the beams with I_{net}/I_g of 0.90 and 0.85 are lower than the predictions. Experimental error, coupled with error in determination of the elastic buckling modes, are two possible reasons of such an underestimation. It is observed that the tested capacity of the beams are not affected by the beam imperfections as shown in Figure 5.2. This is due to the fact that the beam imperfections have less impact on local and the distortional buckling modes which controlled the failure of the 800S200-33 beams.

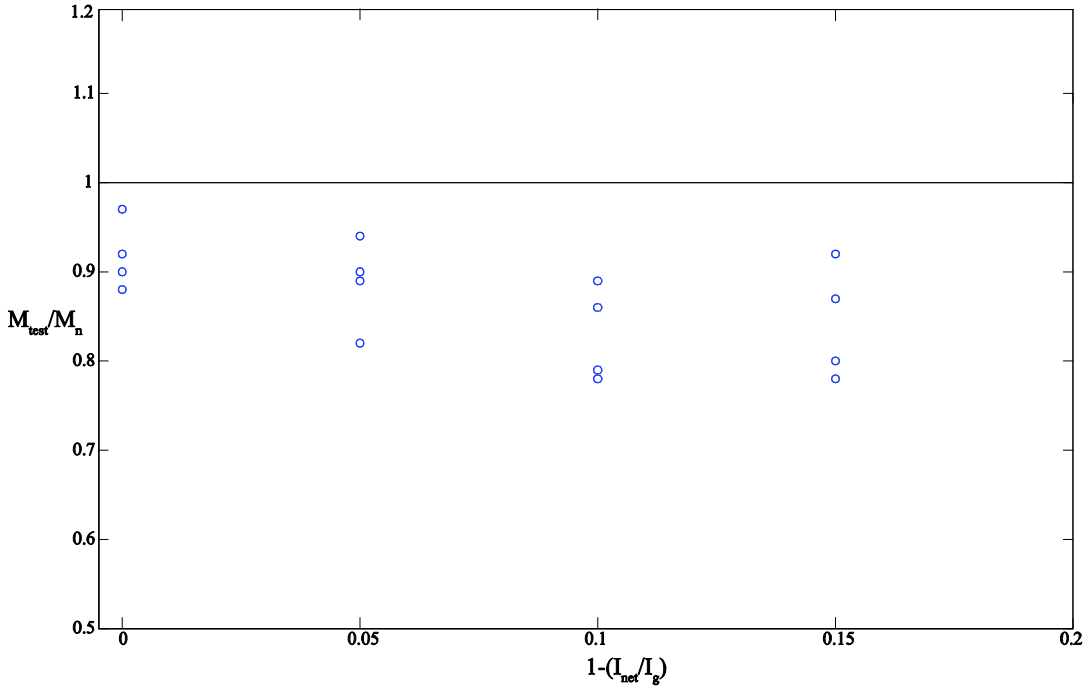

Figure 5.1 Test to predicted ratios with respect to hole size for 800S200-33 beams

Table 5.1 Comparison between the DSM and tested capacity of 800S200-33

800S200-33									
Beam	M_y	M_{ynet}	DSM				Governing mode	M_{test}	M_{test}/M_n
			$M_{n\ell}$	M_{nd}	M_{ne}	M_n			
	kN.m	kN.m	kN.m	kN.m	kN.m	kN.m		kN.m	
800 S 200-33-100-1-1	5.45	5.45	2.75	3.17	4.80	2.75	L	2.66	0.97
800 S 200-33-100-1-2	5.38	5.38	2.89	3.27	4.76	2.89	L	2.66	0.92
800 S 200-33-100-2-1	5.64	5.64	2.78	3.19	4.94	2.78	L	2.49	0.90
800 S 200-33-100-2-2	5.44	5.44	2.82	3.17	4.81	2.82	L	2.49	0.88
800 S 200-33-95-1-1	5.48	5.21	2.77	3.10	4.82	2.77	L	2.48	0.89
800 S 200-33-95-1-2	5.57	5.29	3.03	3.29	4.87	3.03	L	2.48	0.82
800 S 200-33-95-2-1	5.46	5.19	2.79	3.06	4.81	2.79	L	2.63	0.94
800 S 200-33-95-2-2	5.48	5.21	2.91	3.22	4.82	2.91	L	2.63	0.90
800 S 200-33-90-1-1	5.55	5.27	2.88	2.86	4.82	2.86	D	2.55	0.89
800 S 200-33-90-1-2	5.55	5.27	3.00	2.96	4.82	2.96	D	2.55	0.86
800 S 200-33-90-2-1	5.55	5.00	2.90	2.86	4.79	2.86	D	2.27	0.79
800 S 200-33-90-2-2	5.44	4.89	2.95	2.91	4.72	2.91	D	2.27	0.78
800 S 200-33-85-1-1	5.28	5.02	2.83	2.68	4.60	2.68	D	2.45	0.92
800 S 200-33-85-1-2	5.35	5.35	2.95	2.82	4.64	2.82	D	2.45	0.87
800 S 200-33-85-2-1	5.50	4.67	2.93	2.79	4.77	2.79	D	2.22	0.80
800 S 200-33-85-2-2	5.33	4.53	2.98	2.83	4.66	2.83	D	2.22	0.78

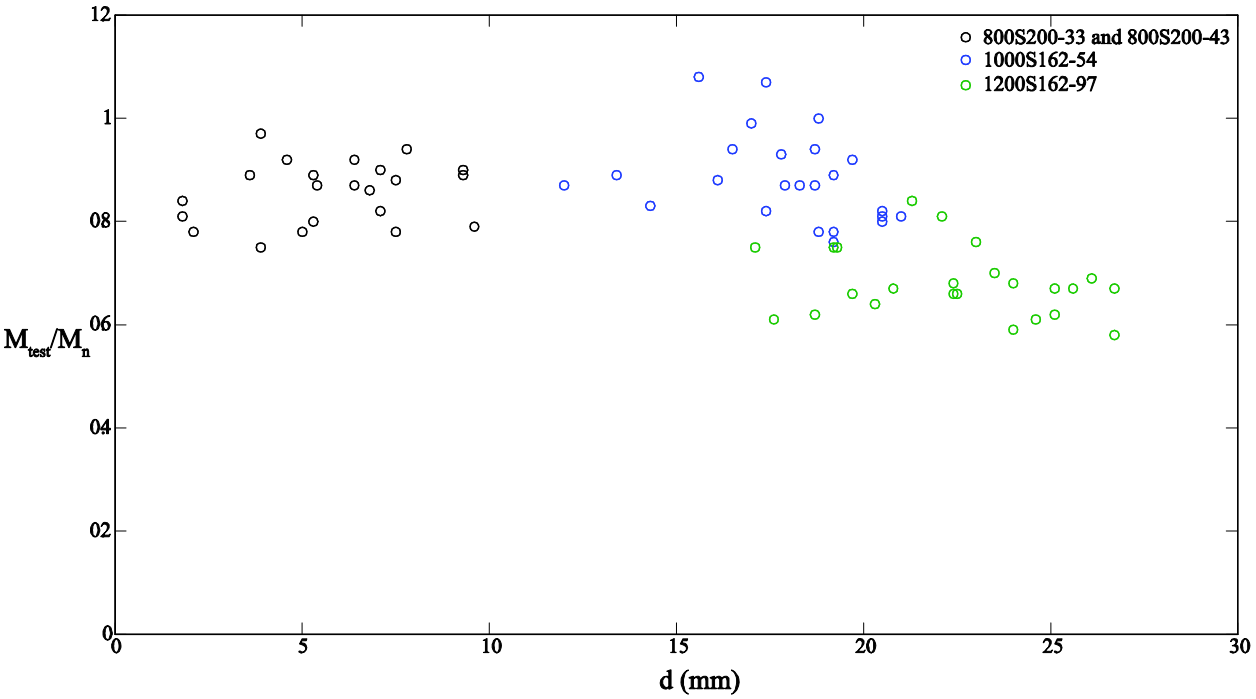

Figure 5.2 Test to predicted ratio with respect to specimen imperfections

The distortional buckling mode is predicted to control the capacity of the 800S200-43 beams as shown in Table 5.2. This is in good agreement with the results obtained from experiments; i.e. distortional buckling causes failure of the 800S200-43 beams. Evaluation of Figure 5.3 suggests that the test-to-predicted capacity increases with an increase in the hole size, but due to small number of specimens tested, a definitive conclusion is precluded.

Table 5.2 Comparison between modified DSM and tested capacity 800S200-43

800S200-43									
Beam	M_y	M_{ynet}	DSM				Governing mode	M_{test}	M_{test}/M_n
			$M_{n\ell}$	M_{nd}	M_{ne}	M_n			
	kN.m	kN.m	kN.m	kN.m	kN.m	kN.m		kN.m	
800 S 200-33-95-1-1	6.51	6.18	4.36	4.51	6.08	4.36	L	3.41	0.78
800 S 200-33-95-1-2	6.41	6.09	4.55	4.53	6.00	4.53	D	3.41	0.75
800 S 200-33-90-1-1	6.50	5.85	4.50	4.30	6.05	4.30	D	3.61	0.84
800 S 200-33-90-1-2	6.47	5.83	4.64	4.47	6.04	4.47	D	3.61	0.81
800 S 200-33-85-1-1	6.36	5.41	4.47	4.16	5.90	4.16	D	3.62	0.87
800 S 200-33-85-1-2	6.39	5.43	4.57	4.09	5.92	4.09	D	3.62	0.89

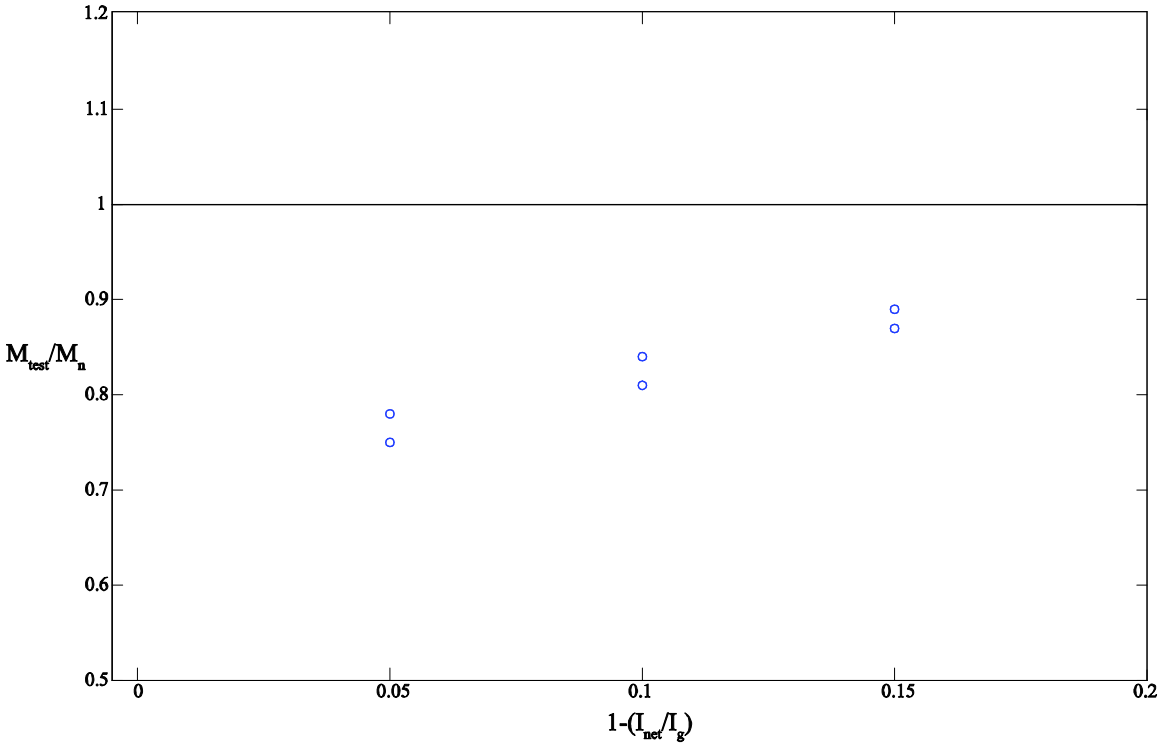

Figure 5.3 Test to predicted ratios with respect to hole size for 800S200-43 beams

Comparison of the experimental and DSM predicted capacities for the 1000S162-54 beams are provided in Table 5.3. Its observed that the DSM predicted controlling mode is local while in the experiments distortional buckling mode was observed to cause the failure of the beams. Investigation of the influence of holes in the test-to predicted capacity of the beams suggests that the beams capacity decreases with an increase in hole depth. Evaluating Figure 5.4, a similar trend in the capacity of the beams is observed in both experiments and the DSM predictions in regards to the influence of the web holes.

Table 5.3 Comparison between modified DSM and tested capacity 1000S162-54

1000S162-54									
Beam	M_y	M_{ynet}	DSM				Governing mode	M_{test}	M_{test}/M_n
			$M_{n\ell}$	M_{nd}	M_{ne}	M_n			
	kN.m	kN.m	kN.m	kN.m	kN.m	kN.m		kN.m	
1000 S 162-54-100-1-1	11.11	11.11	6.49	6.74	8.78	6.49	L	5.66	0.87
1000 S 162-54-100-1-2	11.04	11.04	6.44	6.37	8.94	6.37	D	5.66	0.89
1000 S 162-54-100-2-1	10.50	10.50	6.30	6.42	8.55	6.30	L	5.50	0.87
1000 S 162-54-100-2-2	10.60	10.60	6.49	6.16	8.66	6.16	D	5.50	0.89
1000 S 162-54-100-3-1	10.26	10.26	6.33	6.33	8.45	6.33	L	5.27	0.83
1000 S 162-54-100-3-2	10.42	10.42	6.24	6.06	8.59	6.06	D	5.27	0.87
1000 S 162-54-95-1-1	11.06	10.51	6.21	6.48	8.63	6.21	L	6.67	1.07
1000 S 162-54-95-1-2	11.08	10.53	6.17	6.30	8.85	6.17	L	6.67	1.08
1000 S 162-54-95-2-1	10.93	10.39	6.16	6.40	8.58	6.16	L	5.65	0.92
1000 S 162-54-95-2-2	10.88	10.33	5.99	6.17	8.56	5.99	L	5.65	0.94
1000 S 162-54-95-3-1	10.59	10.06	6.14	6.31	8.47	6.14	L	6.12	1.00
1000 S 162-54-95-3-2	11.12	10.57	6.17	6.29	8.89	6.17	L	6.12	0.99
1000 S 162-54-90-1-1	10.56	9.50	6.32	6.54	8.44	6.32	L	5.09	0.81
1000 S 162-54-90-1-2	10.56	9.50	6.23	6.38	8.53	6.23	L	5.09	0.82
1000 S 162-54-90-2-1	10.62	9.55	6.27	6.60	8.29	6.27	L	5.46	0.87
1000 S 162-54-90-2-2	10.67	9.60	6.21	6.38	8.55	6.21	L	5.46	0.88
1000 S 162-54-90-3-1	11.10	9.99	6.60	6.82	8.89	6.60	L	5.05	0.76
1000 S 162-54-90-3-2	10.97	9.87	6.20	6.51	8.50	6.20	L	5.05	0.81
1000 S 162-54-85-1-1	10.60	9.01	6.18	6.73	8.43	6.18	L	5.79	0.94
1000 S 162-54-85-1-2	11.38	10.81	6.24	6.79	8.79	6.24	L	5.79	0.93
1000 S 162-54-85-2-1	10.61	9.02	6.22	6.42	8.46	6.22	L	4.82	0.78
1000 S 162-54-85-2-2	10.61	9.02	6.15	6.33	8.46	6.15	L	4.82	0.78
1000 S 162-54-85-3-1	10.78	9.17	6.26	6.50	8.53	6.26	L	5.02	0.80
1000 S 162-54-85-3-2	10.84	9.21	6.13	6.33	8.56	6.13	L	5.02	0.82

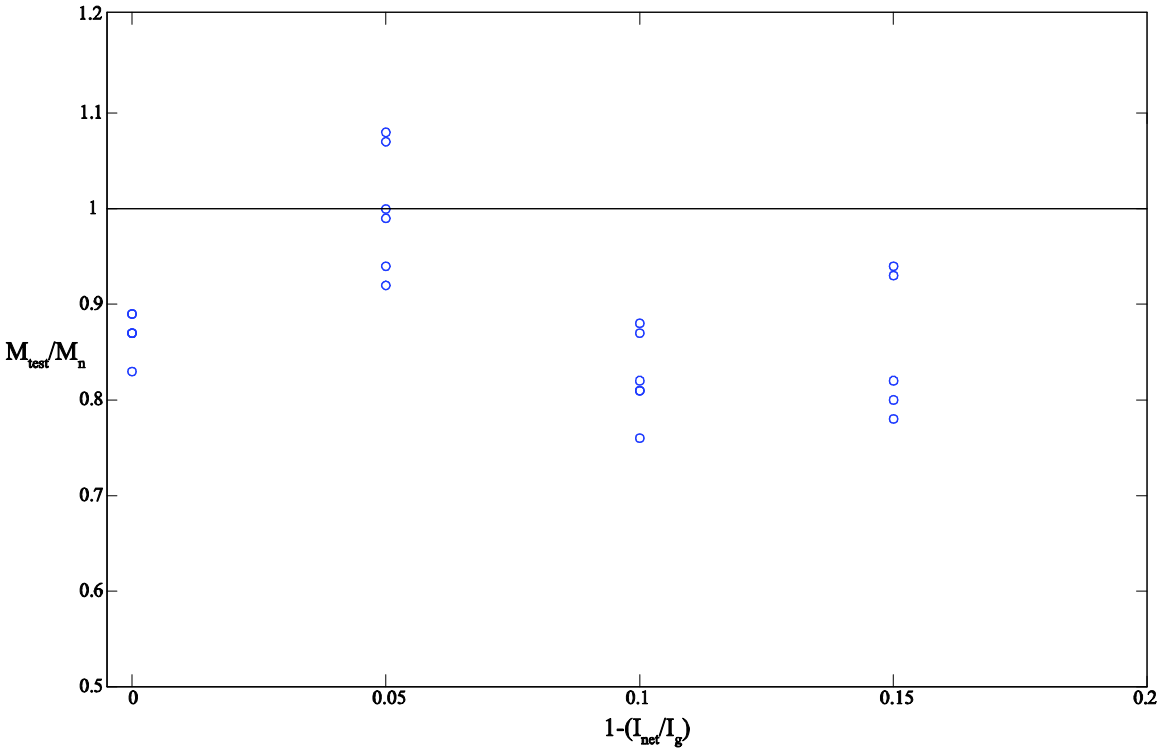

Figure 5.4 Test to predicted ratios with respect to hole size for 1000S162-54 beams

Low test-to-predicted capacities are observed for the 1200S162-97 beams (Table 5.4). This implies that the beam specimen imperfections mainly influence the lateral-torsional buckling mode, which was observed to control the failure of the 1200S162-54 beams. A noticeable reduction in the test-to-predicted ratio of 1200S162-97 beams is observed with an increasing hole depth (Figure 5.5). The local-global buckling mode is determined to govern the strength of the beams. This is in good agreement with the interaction of local and lateral-torsional buckling modes observed in the pre-peak behavior of the beams. Evaluating the trend in the test-to predicted ratios of Figure 5.2, it is observed that the specimen imperfections influence the tested capacity of the beams significantly.

Table 5.4 Comparison between modified DSM and tested capacity 1200S162-97

1200S162-97									
Beam	M_y	M_{ynet}	DSM				Governing mode	M_{test}	M_{test}/M_n
			$M_{n\ell}$	M_{nd}	M_{ne}	M_n			
	kN.m	kN.m	kN.m	kN.m	kN.m	kN.m		kN.m	
1200 S 162-97-100-1-1	27.29	27.29	20.17	21.08	22.47	20.17	L	15.25	0.76
1200 S 162-97-100-1-2	27.55	27.55	20.39	21.37	22.60	20.39	L	15.25	0.75
1200 S 162-97-100-2-1	27.66	27.66	19.79	20.68	22.67	19.79	L	14.79	0.75
1200 S 162-97-100-2-2	25.90	25.90	19.81	20.51	21.70	19.81	L	14.79	0.75
1200 S 162-97-100-3-1	27.55	27.55	20.60	21.10	23.34	20.60	L	17.27	0.84
1200 S 162-97-100-3-2	27.79	27.79	21.22	21.83	23.48	21.22	L	17.27	0.81
1200 S 162-97-95-1-1	27.41	26.04	21.34	22.07	23.06	21.34	L	14.53	0.68
1200 S 162-97-95-1-2	27.58	26.20	21.44	22.32	22.99	21.44	L	14.53	0.68
1200 S 162-97-95-2-1	28.05	26.65	21.50	22.43	23.27	21.50	L	14.32	0.67
1200 S 162-97-95-2-2	28.96	27.51	21.78	22.97	23.61	21.78	L	14.32	0.66
1200 S 162-97-95-3-1	28.73	27.29	21.81	22.82	23.70	21.81	L	14.34	0.66
1200 S 162-97-95-3-2	29.21	27.75	21.49	22.70	23.69	21.49	L	14.34	0.67
1200 S 162-97-90-1-1	27.10	24.39	21.16	21.97	22.67	21.16	L	13.15	0.62
1200 S 162-97-90-1-2	27.50	24.75	21.44	22.46	22.74	21.44	L	13.15	0.61
1200 S 162-97-90-2-1	26.82	24.14	20.13	21.11	22.04	20.13	L	11.83	0.59
1200 S 162-97-90-2-2	27.53	24.78	20.48	21.61	22.41	20.48	L	11.83	0.58
1200 S 162-97-90-3-1	27.83	25.05	20.15	21.38	22.38	20.15	L	14.02	0.70
1200 S 162-97-90-3-2	27.84	25.06	20.20	21.45	22.38	20.20	L	14.02	0.69
1200 S 162-97-85-1-1	27.03	22.98	20.14	20.90	21.55	20.14	L	13.55	0.67
1200 S 162-97-85-1-2	27.33	23.23	20.37	21.16	21.69	20.37	L	13.55	0.67
1200 S 162-97-85-2-1	28.47	24.20	20.79	21.99	22.14	20.79	L	13.30	0.64
1200 S 162-97-85-2-2	27.61	23.47	20.19	21.26	21.75	20.19	L	13.30	0.66
1200 S 162-97-85-3-1	29.35	24.95	21.54	22.59	23.28	21.54	L	13.26	0.62
1200 S 162-97-85-3-2	28.56	24.28	21.77	22.24	22.89	21.77	L	13.26	0.61

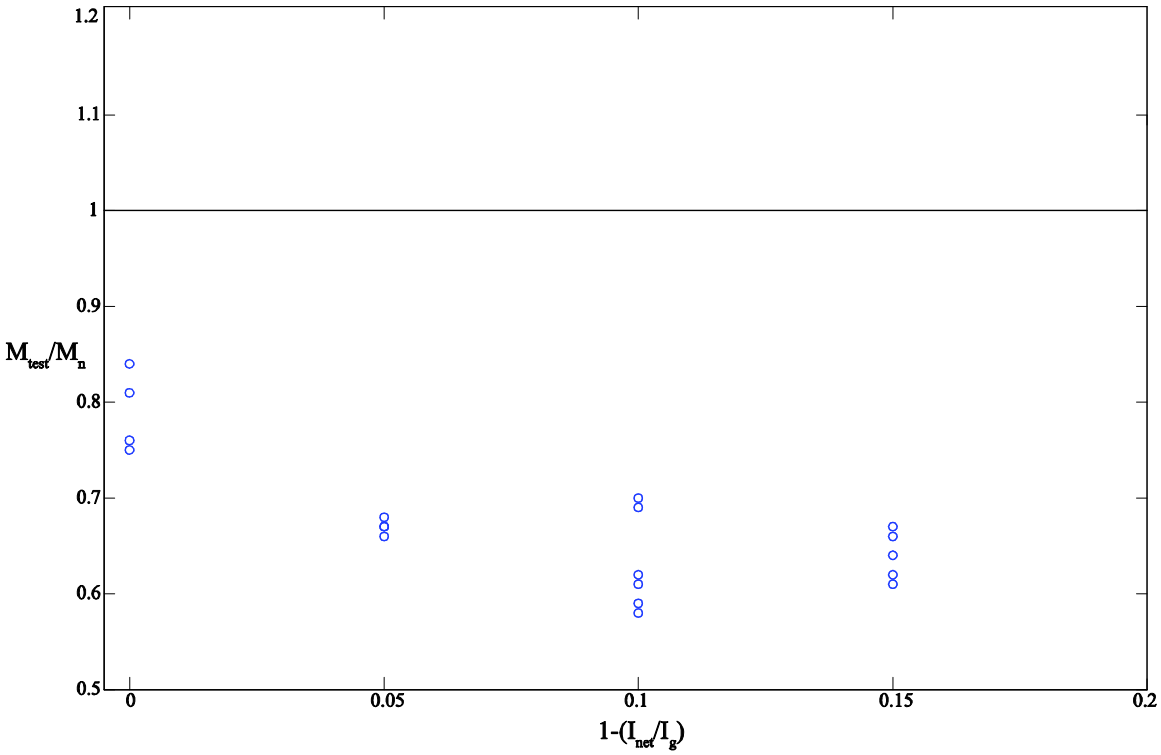

Figure 5.5 Test to predicted ratios with respect to hole size for 1200S162-97 beams

Chapter 6. Conclusions and future work

6.1 Summary

The objective of this study was to investigate the validity of the proposed modified Direct Strength Method for cold-formed steel beams with web holes. Four types of beams evaluated in this study were SSMA800S200-33, SSMA800S200-43, SSMA1000S162-54 and SSMA1200S162-97. The hole depths varied throughout the study. The criterion employed to determine the holes depth was I_{net}/I_g ratio, ranging from 0.85 to 1.0 (no hole), where I_{net} and I_g represent the net and gross moment of inertia of the beams respectively. In order to achieve the research objective a thin shell finite element eigen-buckling study of the beams were performed in ABAQUS. The critical buckling modes were identified and the load corresponding to each mode shape was recorded.

The experimental study carried out, investigated the influence of the web holes on the behavior as well as the failure mechanism of the beams. Load displacement plots were generated and the tested capacities of the beams were evaluated and compared. Results from the elastic buckling and the experimental study were used to evaluate the modifications made to the DSM local and distortional curves. Recommendations were made regarding the modifications.

6.2 Conclusion

The conclusions of this research are classified in three categories: eigen-buckling conclusions, experiment results and the DSM method conclusions.

6.2.1 Eigen-buckling conclusions

The buckling of the unstiffened strip (LH mode) influenced and sometime governed the critical buckling moments. The critical local buckling moments decreased by providing small web holes (I_{net}/I_g=0.95) while the larger holes stiffened the buckling in the unstiffened strip, causing the local buckling modes to occur away from the holes. The unstiffened strip buckling was also mixed with the distortional buckling modes at the location of the holes. The distortional and lateral-torsional buckling modes were observed to amplify with the presence of holes.

6.2.2 Experiment conclusions

Distortional buckling mode was determined as the dominant buckling mode causing failure of the 8 in. and 10 in. deep beams while the 12 in. beams failed due to an interaction of local and lateral-torsional buckling modes. A mixing of the local and the distortional buckling modes was observed in the behavior of the beams incorporating web holes. Cross-section dimensions induced global imperfections in the specimen reduced the tested capacity with an increasing height of the beams. Evaluation of the test data demonstrated that an increase in hole depth results in a decrease in the tested capacity as well as the post-peak ductility of the beams.

6.2.3 DSM conclusions

The modified DSM equations could not be evaluated with the test data achieved through this research. Beams with smaller distortional slenderness are required to investigate the validity of the transition equations proposed for elastic/inelastic distortional buckling effects. Additionally it was observed that the DSM equations do not take into account the influence of member global imperfections created by cross-section distortion during manufacturing.

6.3 Recommendations for future research

From the present research, it was concluded that the beam specimen's imperfections have an impact on the tested capacity of the members. In the future, it is recommended that a more precise test set up be used which accounts for the influence of fabrication as well as construction imperfections.

In this study six beams of 800S200-43 type were studied the results of which show an increase in the tested capacity of the member. The few number of tests performed for this type of cross-section inhibits a definitive conclusion. A more comprehensive study of the 800S200-43 beams is planned. The tested strengths of these specimens will be added to the experiment database.

Automated tools to identify the local, distortional and global buckling modes in the finite element eigen-buckling analysis are needed. Development of such a capability is a topic of current research.

The present DSM modifications were observed to predict the distortional capacity of the beams unconservatively. The equations proposed to capture the transition between elastic and inelastic buckling modes are planned to be evaluated for cross-sections with smaller distortional slenderness.

References

ABAQUS. (2009a). ″ABAQUS/Standard Version 6.7-1.″, Dassault Systèmes, http://www.simulia.com/, Providence, RI.

AISI-S100. (2007). North American Specification for the Design of Cold‐Formed Steel Structural Members, American Iron and Steel Institute, Washington, D.C.

CUFSM V3.12. (elastic-buckling analysis of thin-walled members by the finite strip method). B. Schafer.

Bowen, R. E. (2009). Experimental Verification of a Mechanics-Based Prediction Method for Coiling Residual Stresses in Cold-Formed Steel Structural Members. The Charles Edward Via, Jr. Department of Civil and Environmental Engineering. Blacksburg, Virginia Polytechnic Institute and State University. Master of Science: 30.

Chajes, A., - (1974). Principles of structural stability theory. Englewood Cliffs, N.J., Prentice-Hall.

Chu, X.-t., J. Rickard, et al. (2005). "Influence of lateral restraint on lateral-torsional buckling of cold-formed steel purlins." Thin-Walled Structures 43(5): 800-810.

Cook, R. D. (1989). Concepts and applications of finite element analysis. New York :, Wiley.

Habitat, C. o. T. B. a. U. (1993). Cold-Formed Steel In Tall Buildings. New York, McGraw-Hill, Inc.

Hancock, G. J. (1997). "Design for distortional buckling of flexural members." Thin-Walled Structures 27(1): 3-12.

Hancock, G. J. (2001). Cold-Formed Steel Structures to the AISI Specification. New York, Marcel Dekker, Inc.

Kwon, Y. B. and G. J. Hancock (1993). "Post-buckling analysis of thin-walled channel sections undergoing local and distortional buckling." Computers & Structures 49(3): 507-516.

LaBoube, R. A., W. W. Yu, et al. (1997). "Cold-formed steel webs with openings: Summary report." Thin-Walled Structures 27(1): 79-84.

Michael Davies, J., P. Leach, et al. "The design of perforated cold-formed steel sections subject to axial load and bending." Thin-Walled Structures 29(1-4): 141-157.

Moen, C. D. (2008). Direct Strength Design of Cold-Formed Steel Members with Perforations. Department of Civil Engineering Baltimore, Johns Hopkins University. Doctor of Philosophy: 592.

Moen, C. D. and B. W. Schafer (2006). Impact of holes on the elastic buckling of cold-formed steel columns with application to the direct strength method. 18th International Specialty Conference on Cold-Formed Steel Structures: Recent Research and Developments in Cold-Formed Steel Design and Construction, October 26, 2006 - October 27, 2006, Orlando, FL, United states, University of Missouri-Rolla.

Moen, C. D. and B. W. Schafer (2008). "Experiments on cold-formed steel columns with holes." Thin-Walled Structures 46(10): 1164-1182.

Moen, C. D. and B. W. Schafer (2009). "Elastic buckling of thin plates with holes in compression or bending." Thin-Walled Structures 47(12): 1597-1607.

Pennock, R. W. and J. L. Dawe (2003). Light gauge cold formed steel joists with web perforations. Canadian Society for Civil Engineering - 31st Annual Conference: 2003 Building our Civilization, June 4, 2003 - June 7, 2003, Moncton, NB, Canada, Canadian Society for Civil Engineering.

Schafer, B. W. "Review: The Direct Strength Method of cold-formed steel member design." Journal of Constructional Steel Research 64(7-8): 766-778.

Schafer, B. W. (2006). Designing cold-formed steel using the direct strength method. 18th International Specialty Conference on Cold-Formed Steel Structures: Recent Research and Developments in Cold-Formed Steel Design and Construction, October 26, 2006 - October 27, 2006, Orlando, FL, United states, University of Missouri-Rolla.

Schafer, B. W. and S. Adany (2006). Buckling analysis of cold-formed steel members using CUFSM: Conventional and constrained finite strip methods. 18th International Specialty Conference on Cold-Formed Steel Structures: Recent Research and Developments in Cold-Formed Steel Design and Construction, October 26, 2006 - October 27, 2006, Orlando, FL, United states, University of Missouri-Rolla.

Schafer, B. W. and T. Pekoz (1998). Direct strength prediction of cold-formed steel members using numerical elastic buckling solutions. Fourteenth International Specialty Conference on Cold-Formed Steel Structures: Recent Research and Developments in Cold-Formed Steel Design and Construction, October 15, 1998 - October 16, 1998, St. Louis, MO, United states, University of Missouri-Rolla.

Shan, M. Y., K. D. Batson, et al. (1994). "Local buckling flexural strength of webs with openings." Engineering Structures 16(5): 317-323.

von Karman, T., E. E. Sechler, et al. (1932). "The strength of thin plates in compression." ASME 54(54-5).

Winter, G. (1947). "Strength of thin steel compression flanges." American Society of Civil Engineers -- Proceedings 73(1, 3): 360-366.

Yu, C. and B. W. Schafer (2002). Local buckling tests on cold-formed steel beams. Sixteenth International Specialty Conference on Cold-Formed Steel Structures: Recent Research and Developments in Cold-Formed Steel Design and Construction, October 17, 2002 - October 18, 2002, Orlando, FL, United states, University of Missouri-Rolla.

Yu, C. and B. W. Schafer (2003). "Local buckling tests on cold-formed steel beams." Journal of Structural Engineering 129(12): 1596-1606.

Yu, C. and B. W. Schafer (2005). Distortional buckling tests on cold-formed steel beams. 17th International Specialty Conference on Cold-Formed Steel Structures: Recent Research and Developments in Cold-Formed Steel Design and Construction, November 4, 2004 - November 5, 2004, Orlando, FL, United states, University of Missouri-Rolla.

Yu, C. and B. W. Schafer (2006). "Distortional buckling tests on cold-formed steel beams." Journal of Structural Engineering 132(4): 515-528.

Yu, C. and B. W. Schafer (2006). Finite element modeling of cold-formed steel beams: Validation and application. 18th International Specialty Conference on Cold-Formed Steel Structures: Recent Research and Developments in Cold-Formed Steel Design and Construction, October 26, 2006 - October 27, 2006, Orlando, FL, United states, University of Missouri-Rolla.

Yu, C. and B. W. Schafer (2007). "Simulation of cold-formed steel beams in local and distortional buckling with applications to the direct strength method." Journal of Constructional Steel Research 63(5): 581-590.

Yu, W.-w., - (2000). Cold-formed steel design. New York ; Chichester :, Wiley.

Yu, W.-W. and C. S. Davis (1973). "COLD-FORMED STEEL MEMBERS WITH PERFORATED ELEMENTS." 99(ST10): 2061-2077.

Yu, W.-W. and R. A. LaBoube "University of Missouri-Rolla research on cold-formed steel structures." Thin-Walled Structures 28(3-4): 213-223.

Appendix A Experimental results

This appendix contains the load-deformation behavior of each test as well as the buckling modes observed to control the failure of the beam specimens. The description of different buckling modes as well as the maximum capacity of each beam specimen is provided in Chapter 4.

800S200-33-100-1

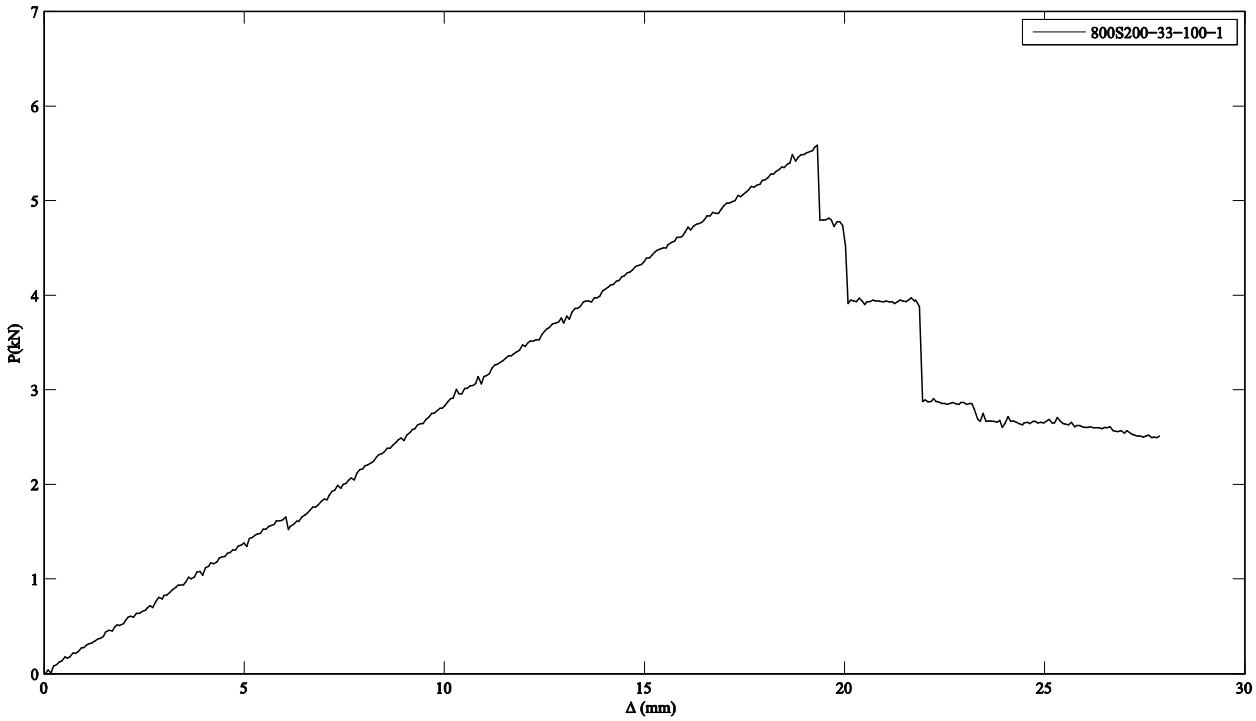

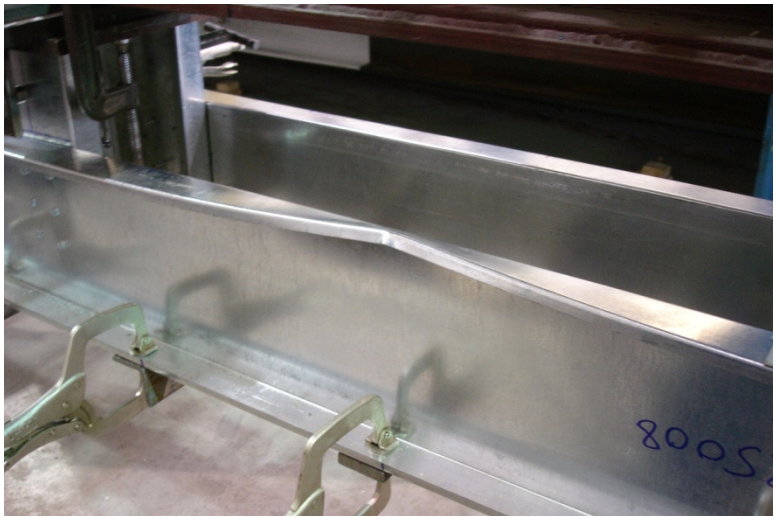

Notes:

Beams failed by distortional collapse

Dents were observed in the top flange

800S200-33-100-2

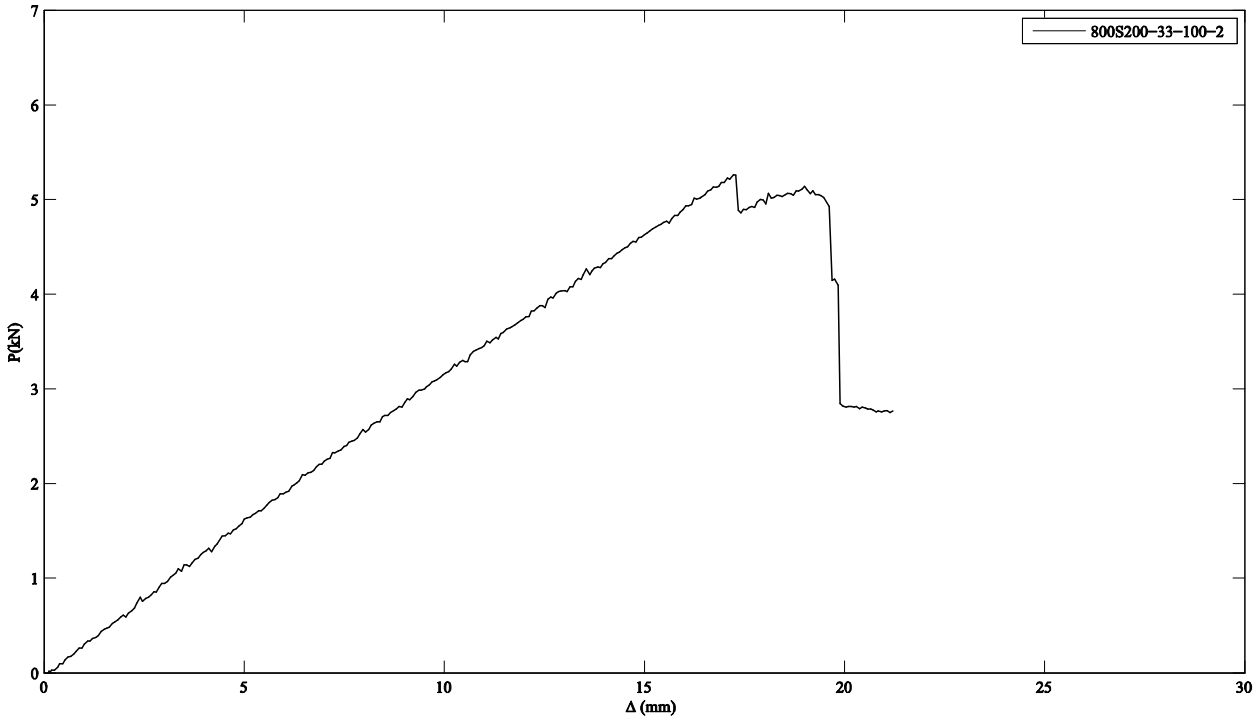

Notes:

Beams failed by distortional collapse

800S200-33-95-1

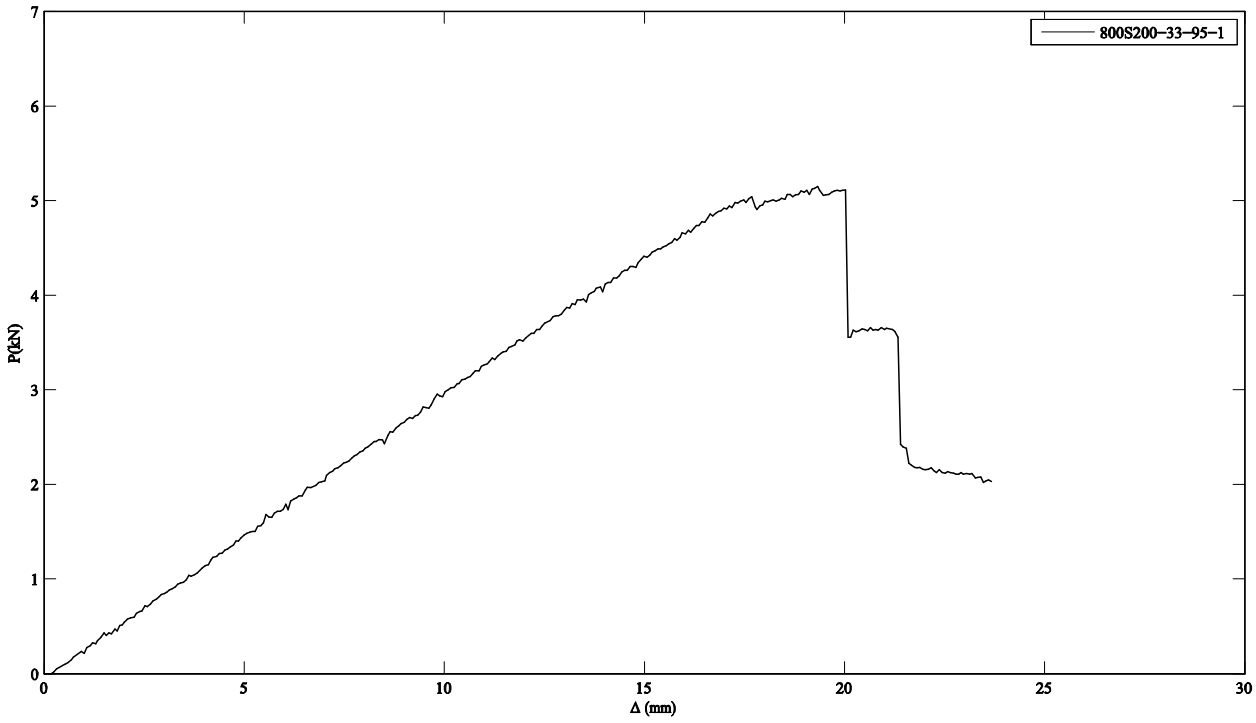

Notes:

Beams failed by distortional collapse

Failure initiated in beam 2

800S200-33-95-2

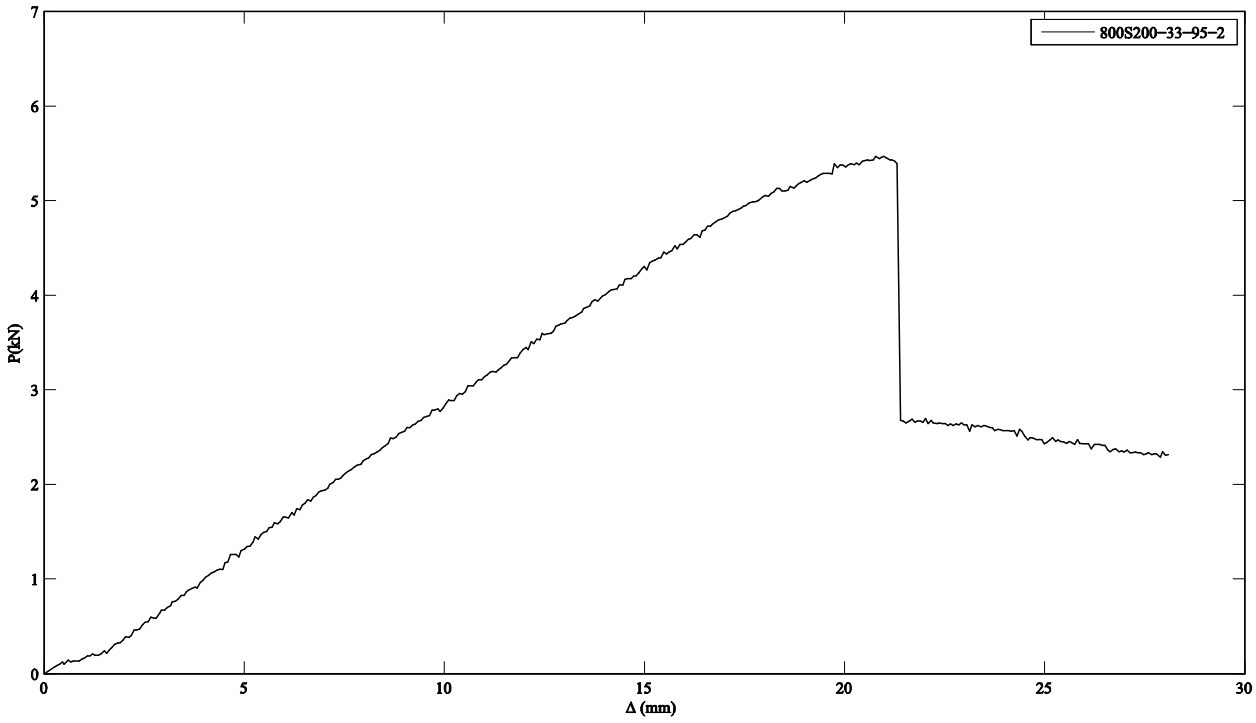

Notes:

Beams failed by distortional collapse

800S200-33-90-1

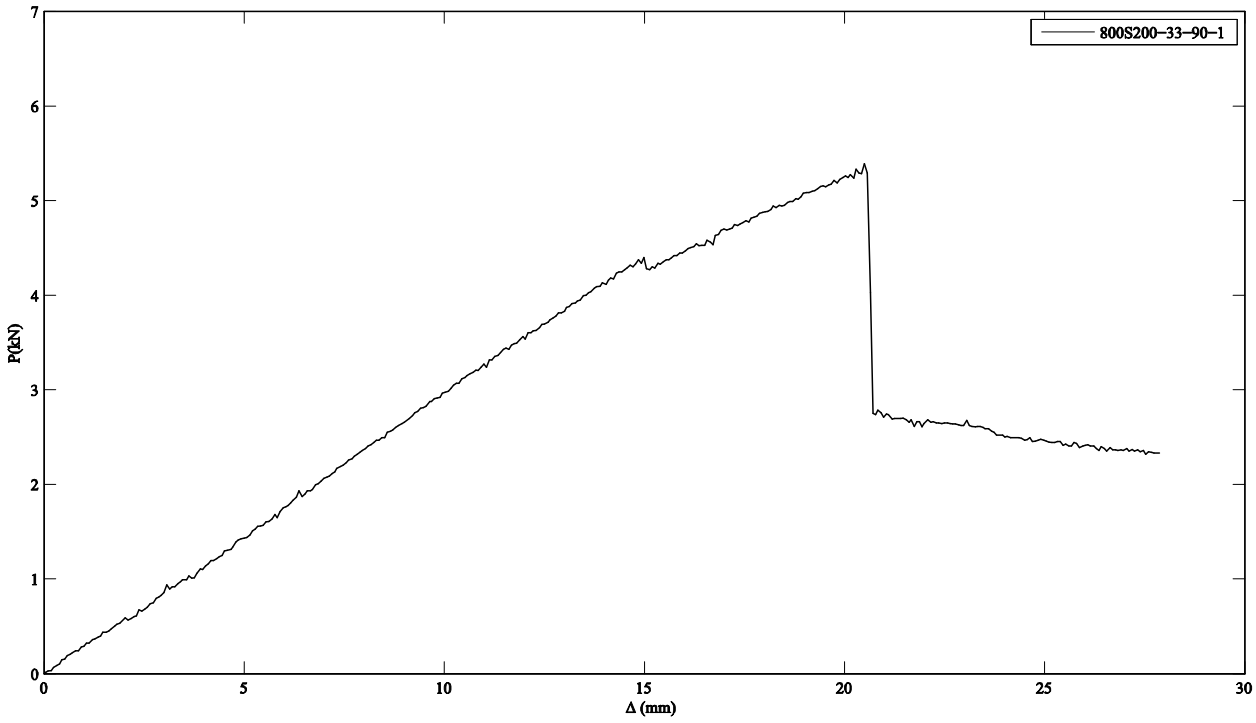

Notes:

Beams failed by distortional collapse

Dents were observed in top flange

800S200-33-90-2

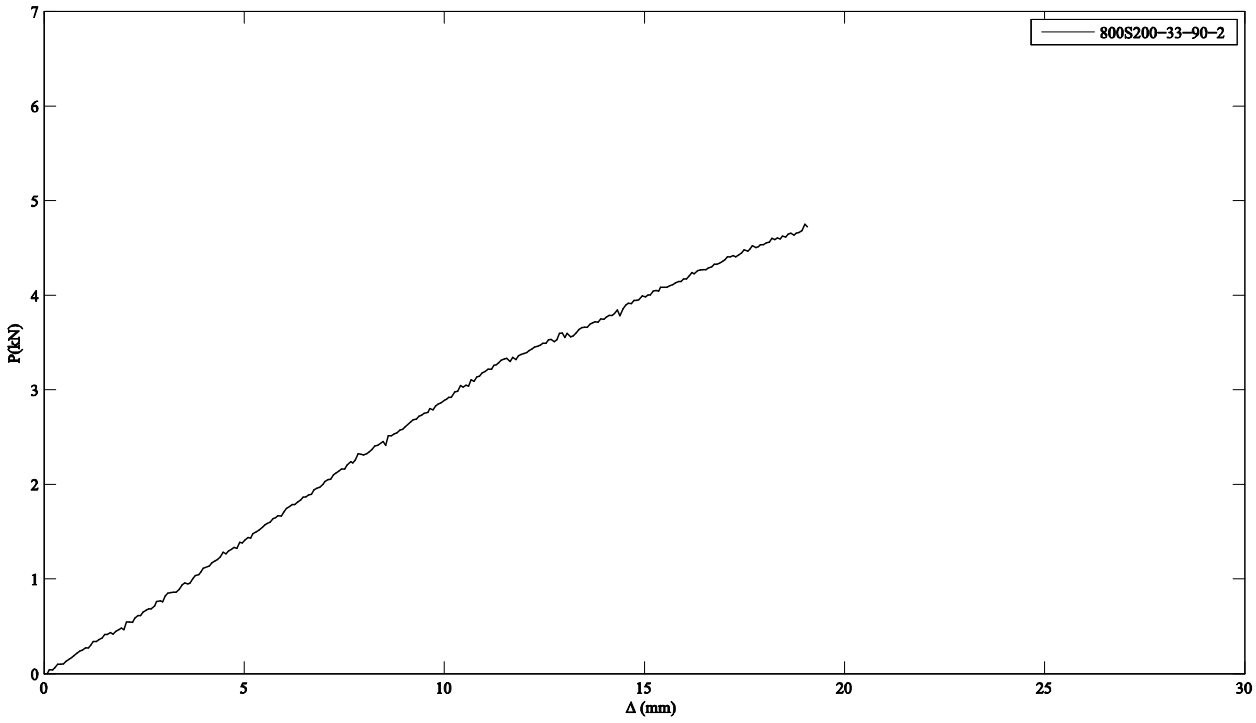

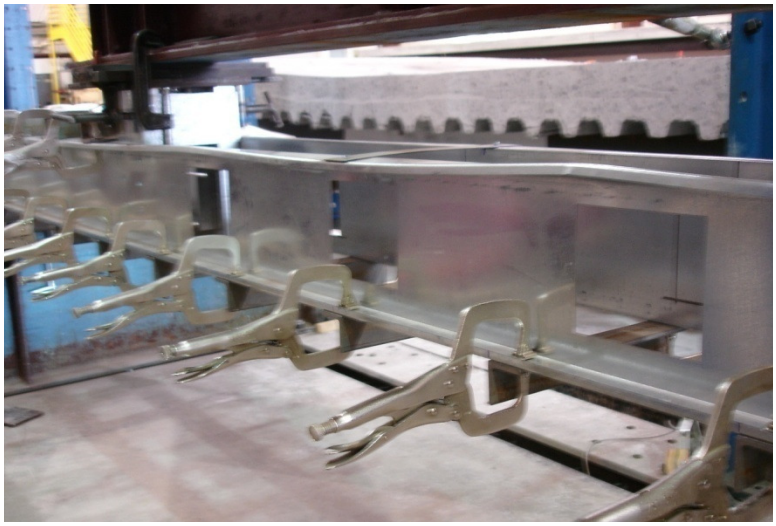

Notes:

Beams failed by distortional collapse

800S200-33-85-1

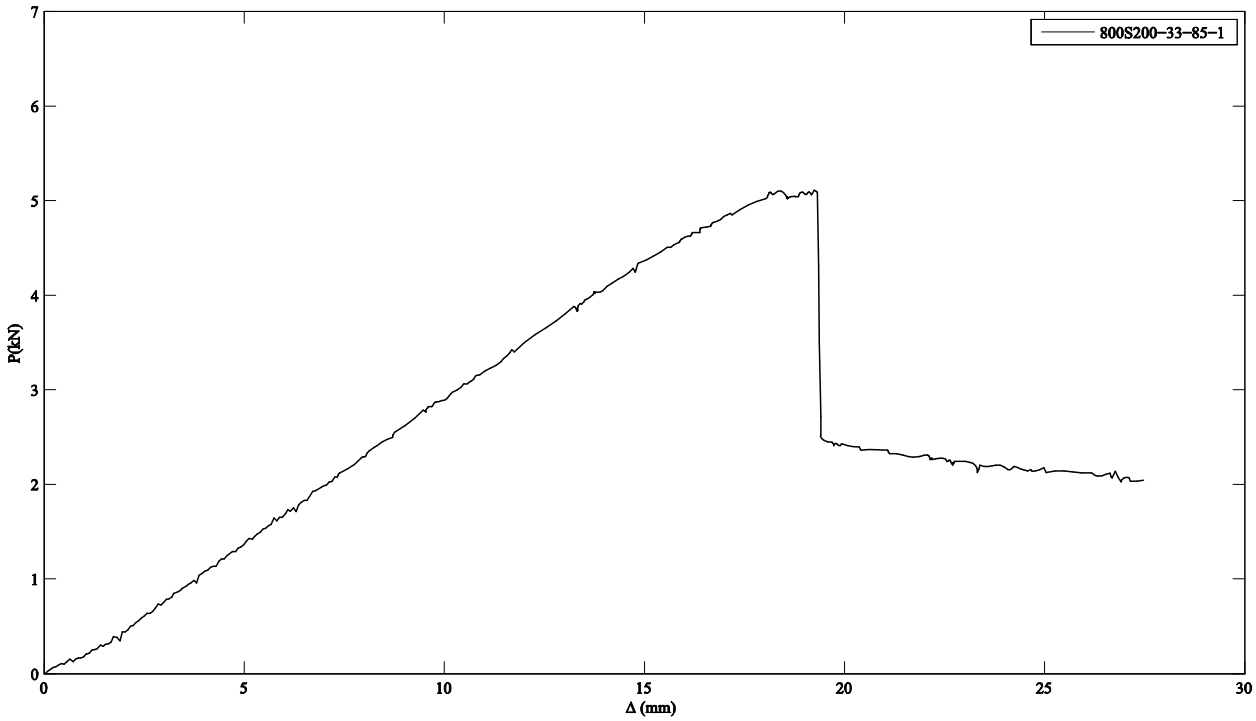

Notes:

Beams failed by distortional collapse

800S200-33-85-2

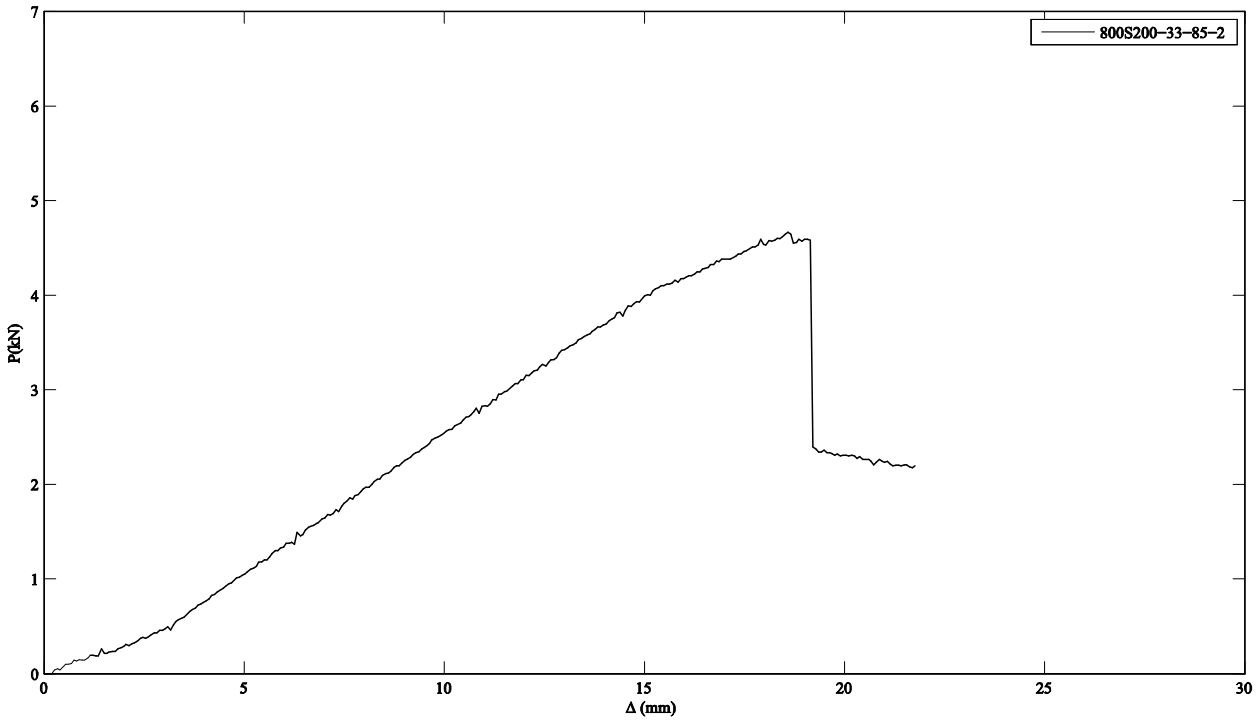

Notes:

Beams failed by distortional collapse

800S200-43-95-1

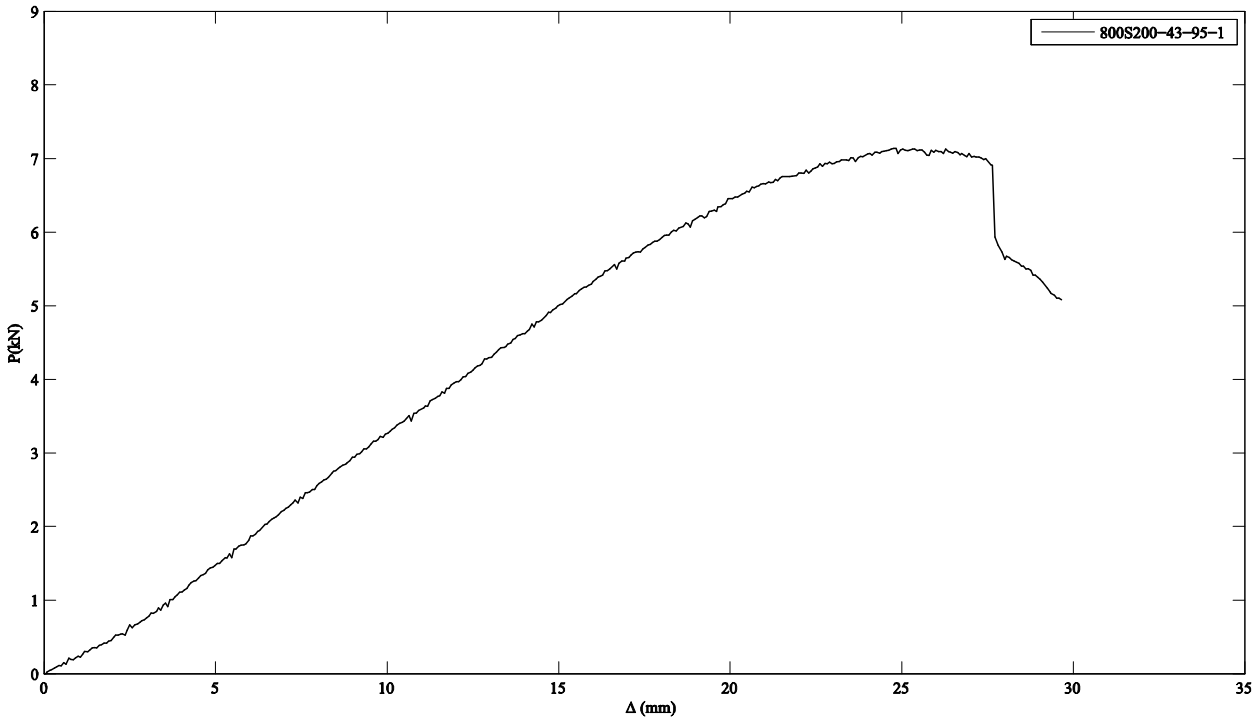

Notes:

Beams failed by distortional collapse

Neoprene pads were used to spread the loads

Dents were observed in the web

800S200-43-90-1

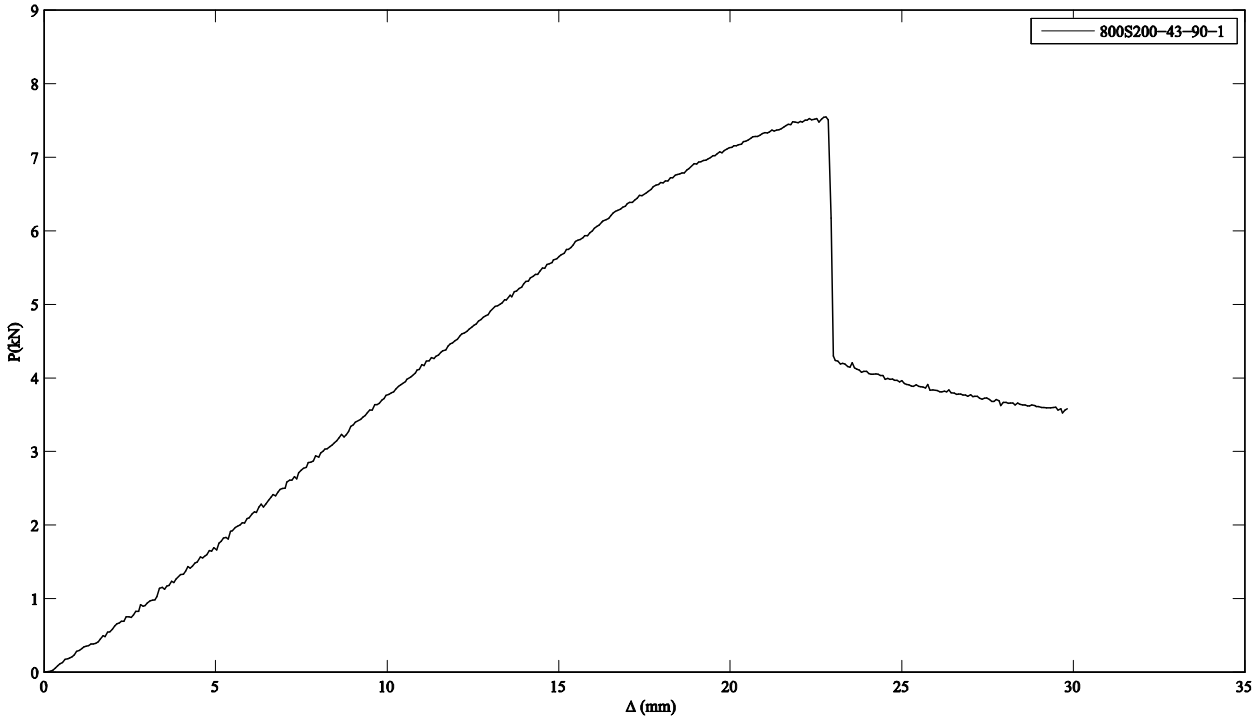

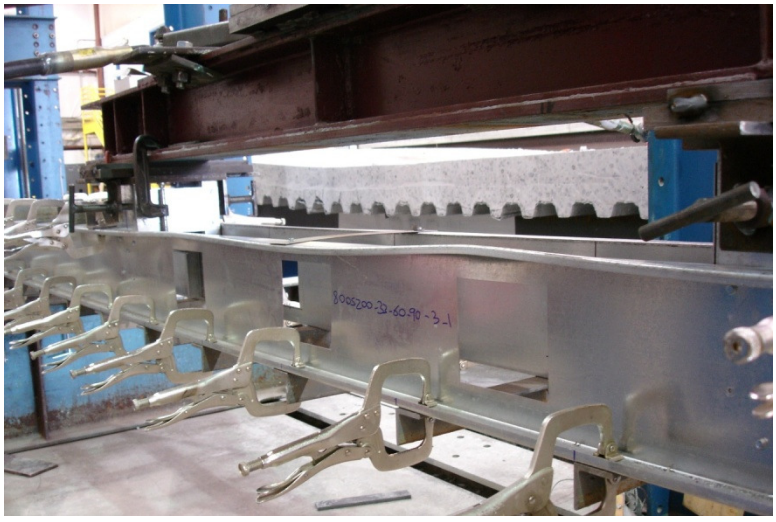

Notes:

Beams failed by distortional collapse

Extended rotation of loading points were observed

800S200-43-85-1

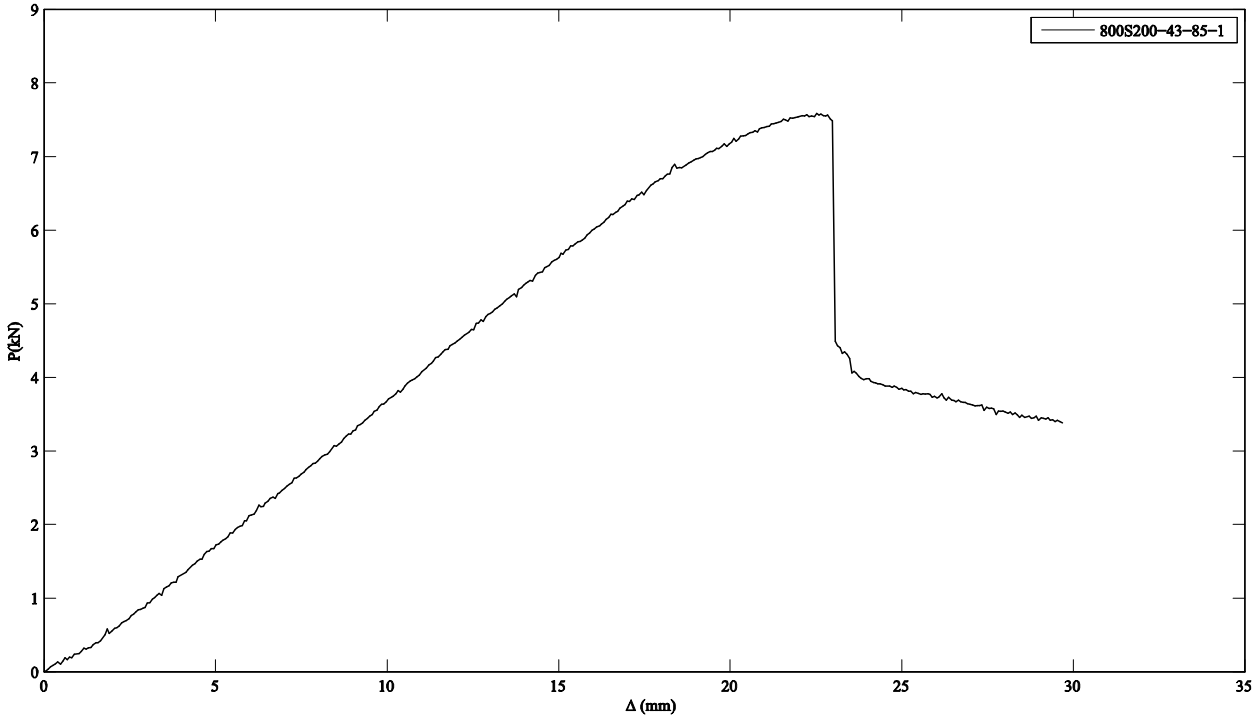

Notes:

Beams failed by distortional collapse

1000S162-54-100-1

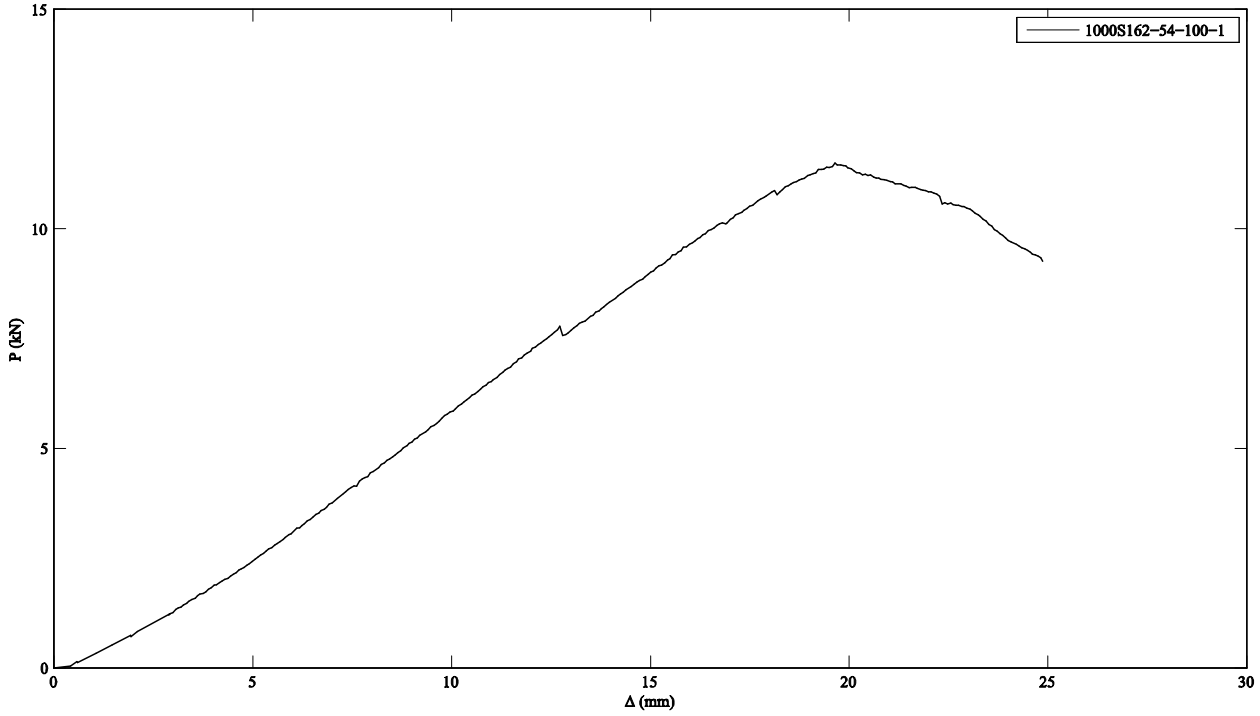

Notes:

Beams failed by distortional collapse

1000S162-54-100-3

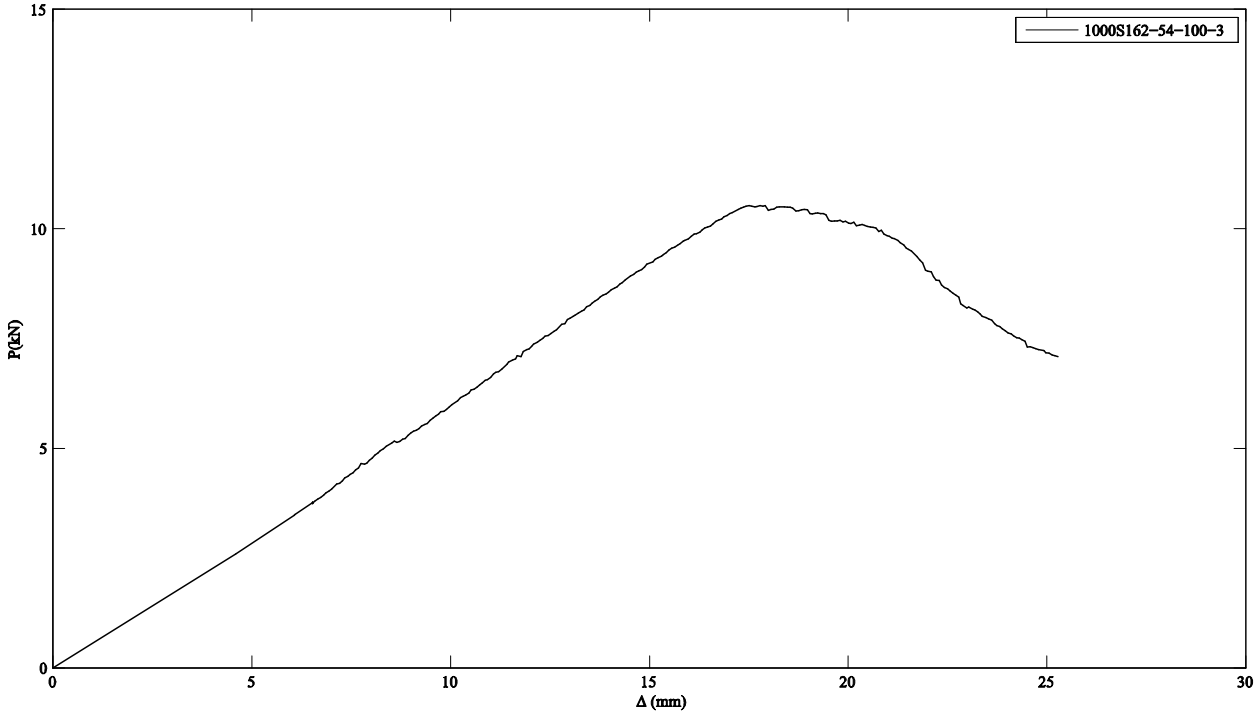

Notes:

Beams failed by distortional collapse

1000S162-54-95-1

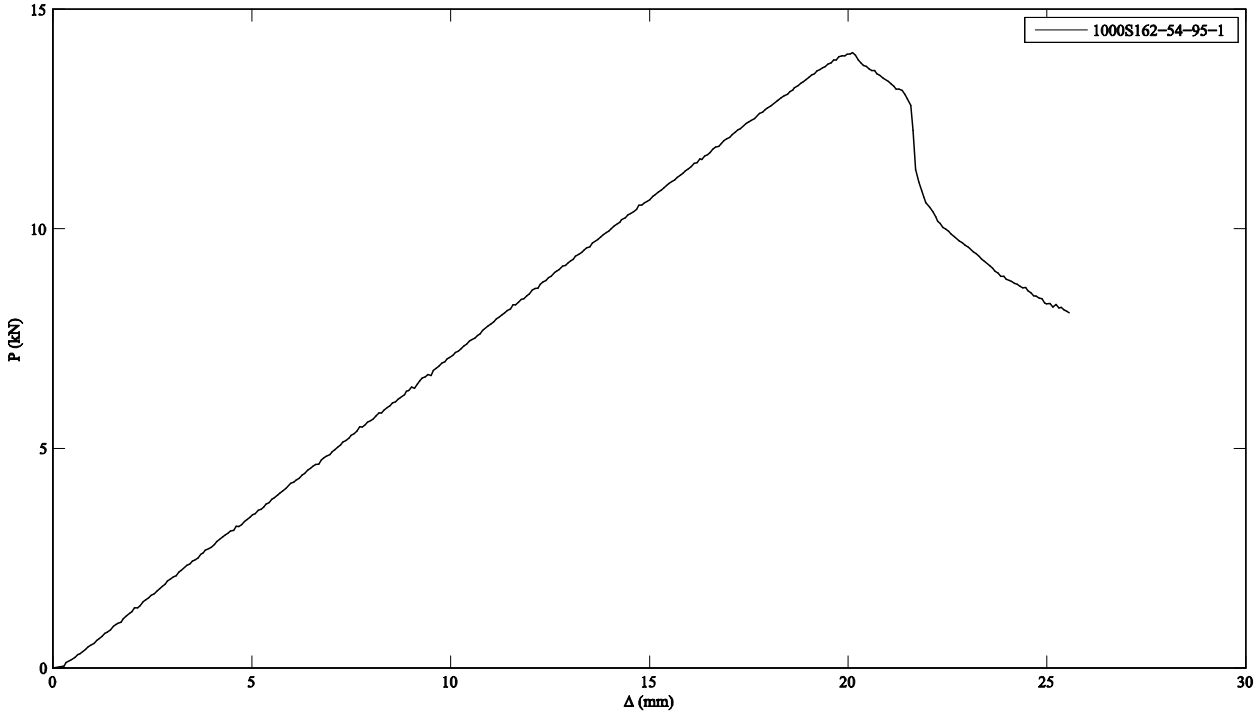

Notes:

Beams failed by distortional collapse

1000S162-54-95-2

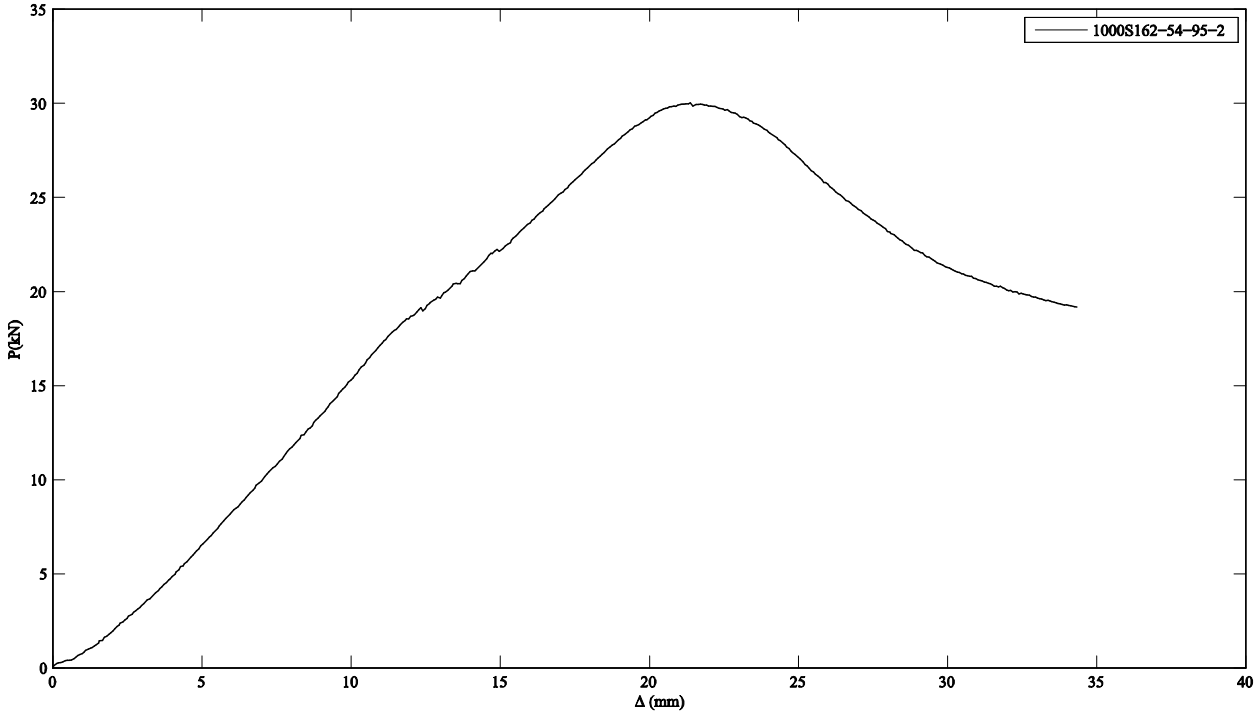

Notes:

Beams failed by distortional collapse

The scissor braces were adjusted while loading the beams

1000S162-54-95-3

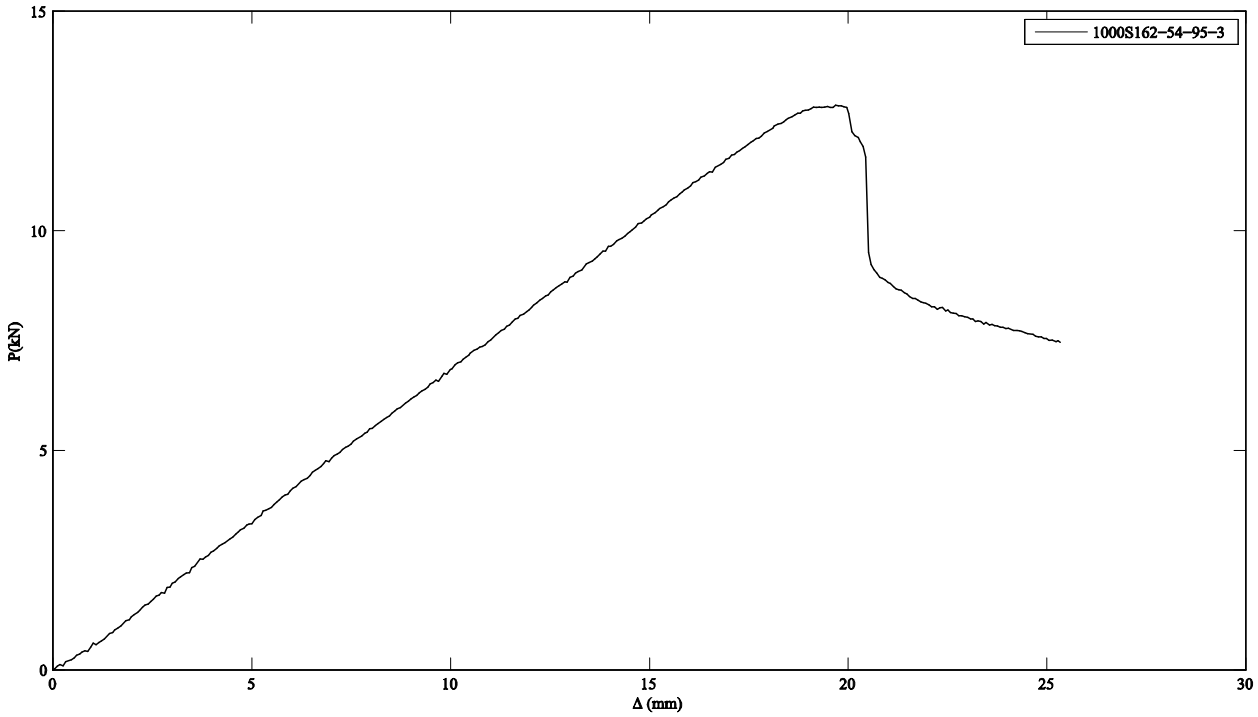

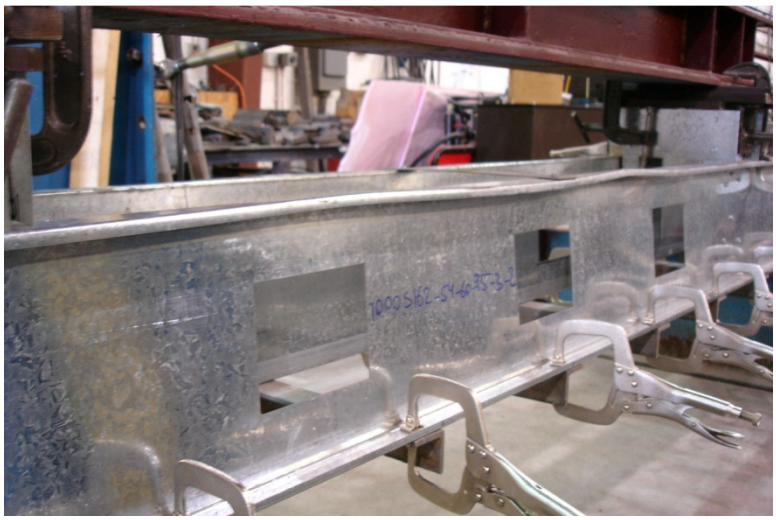

Notes:

Beams failed by distortional collapse

1000S162-54-90-1

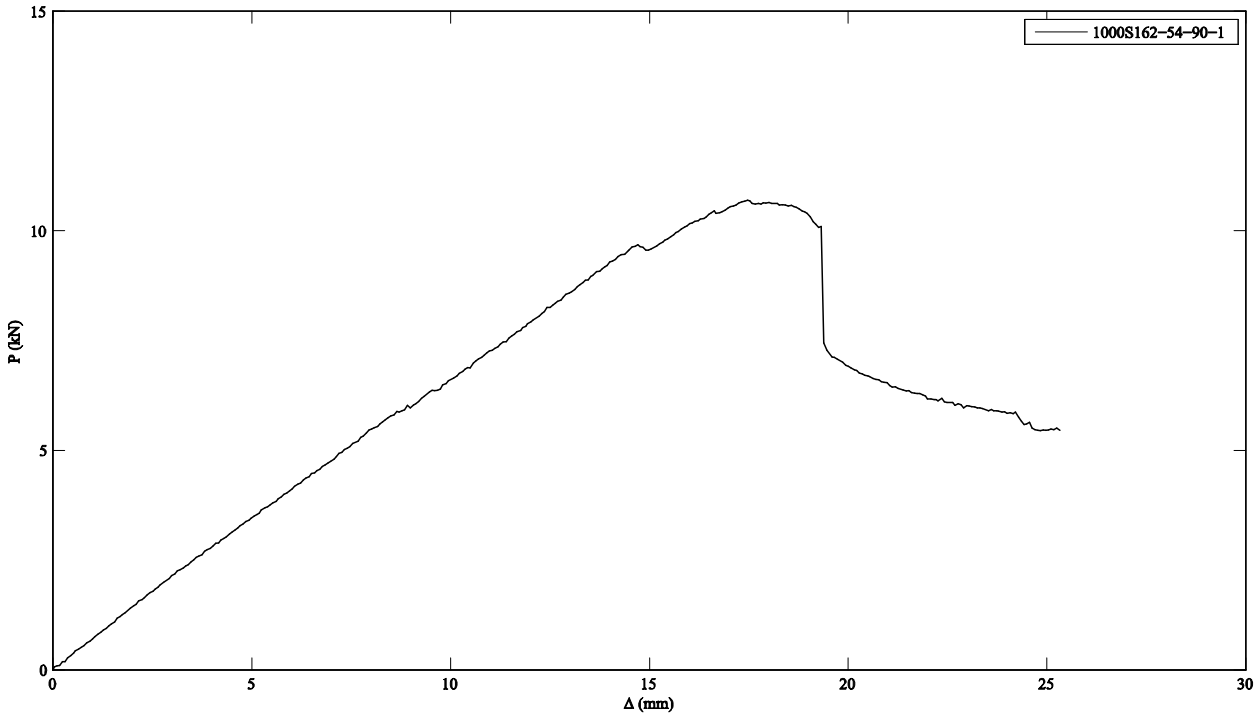

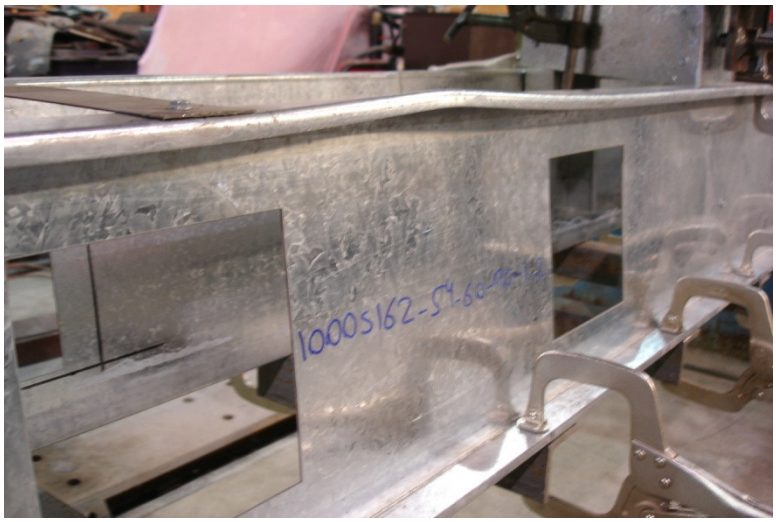

Notes:

Beams failed by distortional collapse

The scissor braces were adjusted while loading the beams

1000S162-54-90-2

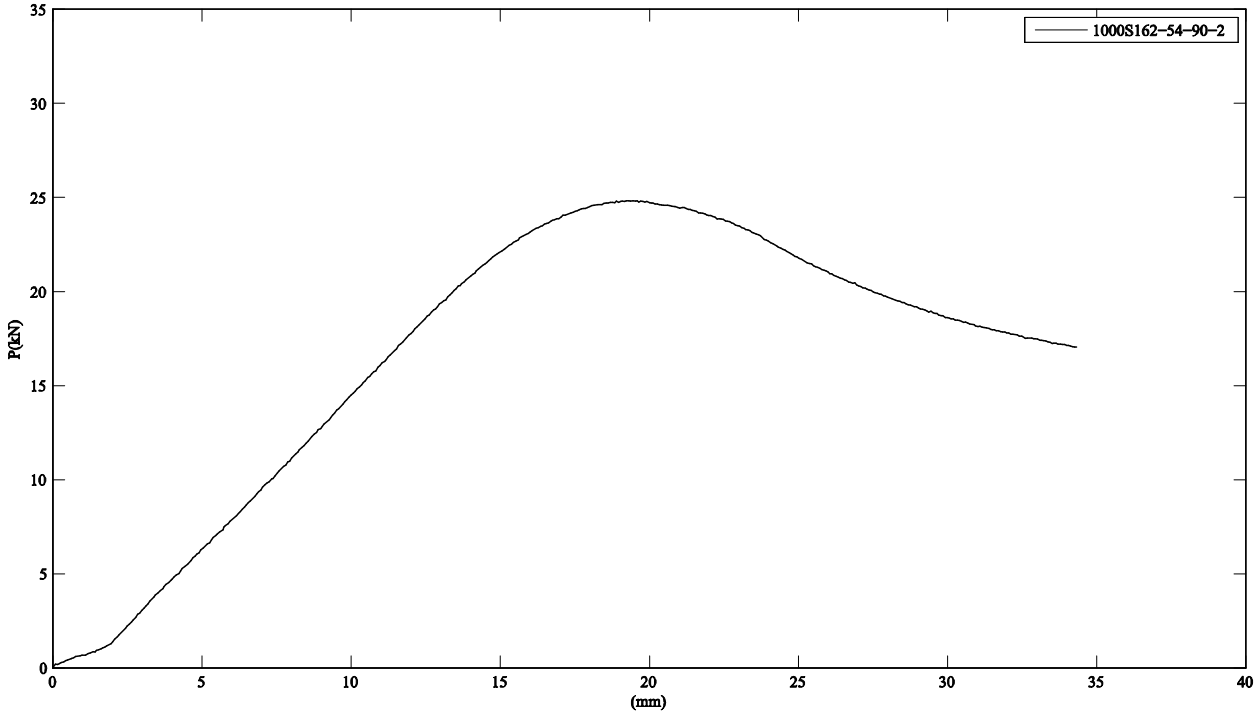

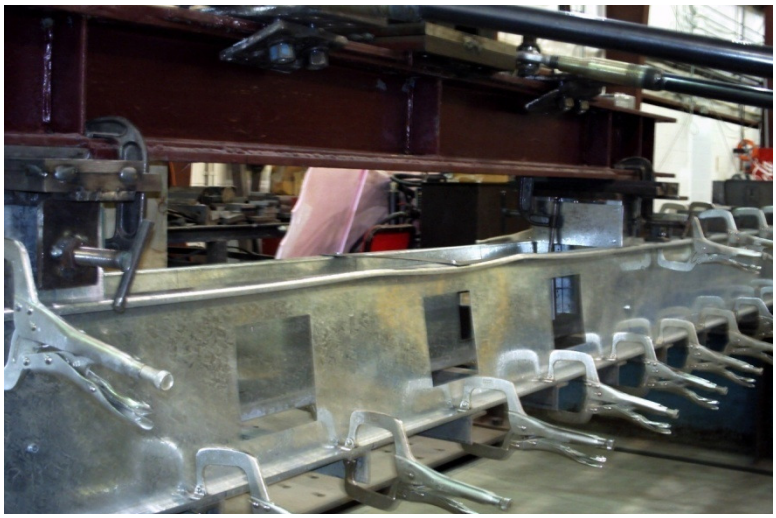

Notes:

Beams failed by distortional collapse

1000S162-54-90-3

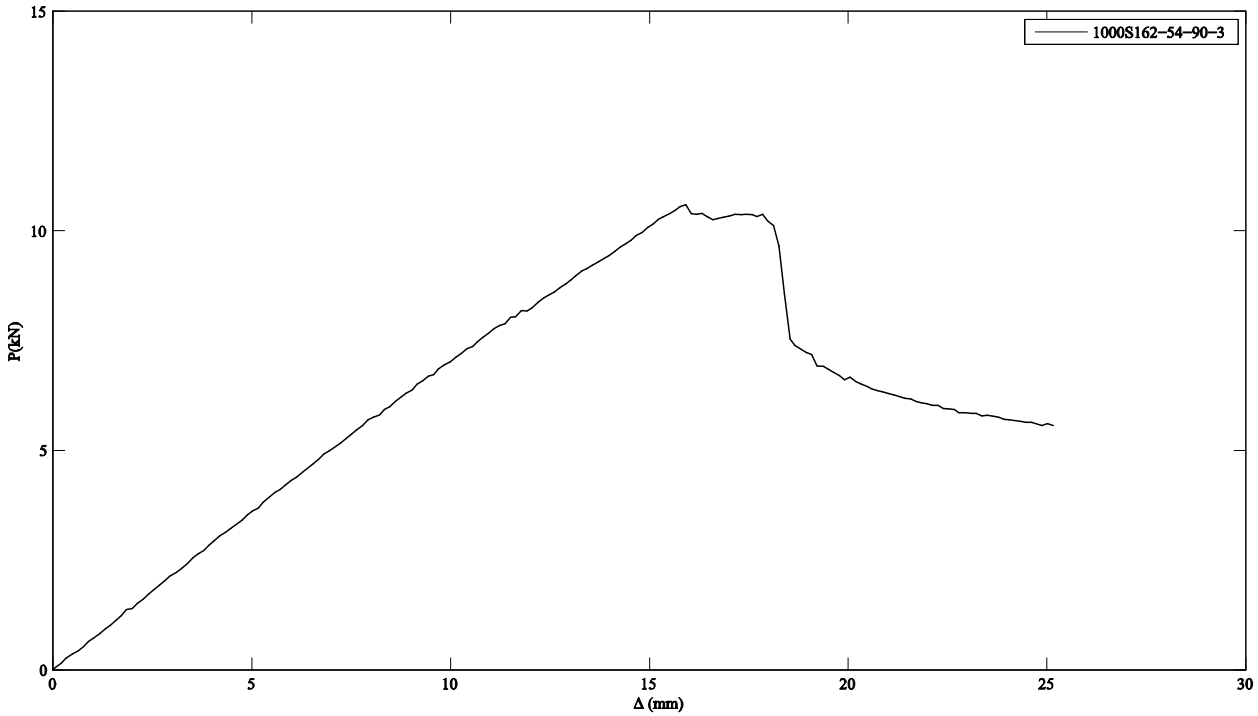

Notes:

Beams failed by distortional collapse

The scissor braces were adjusted while loading the beams

1000S162-54-85-1

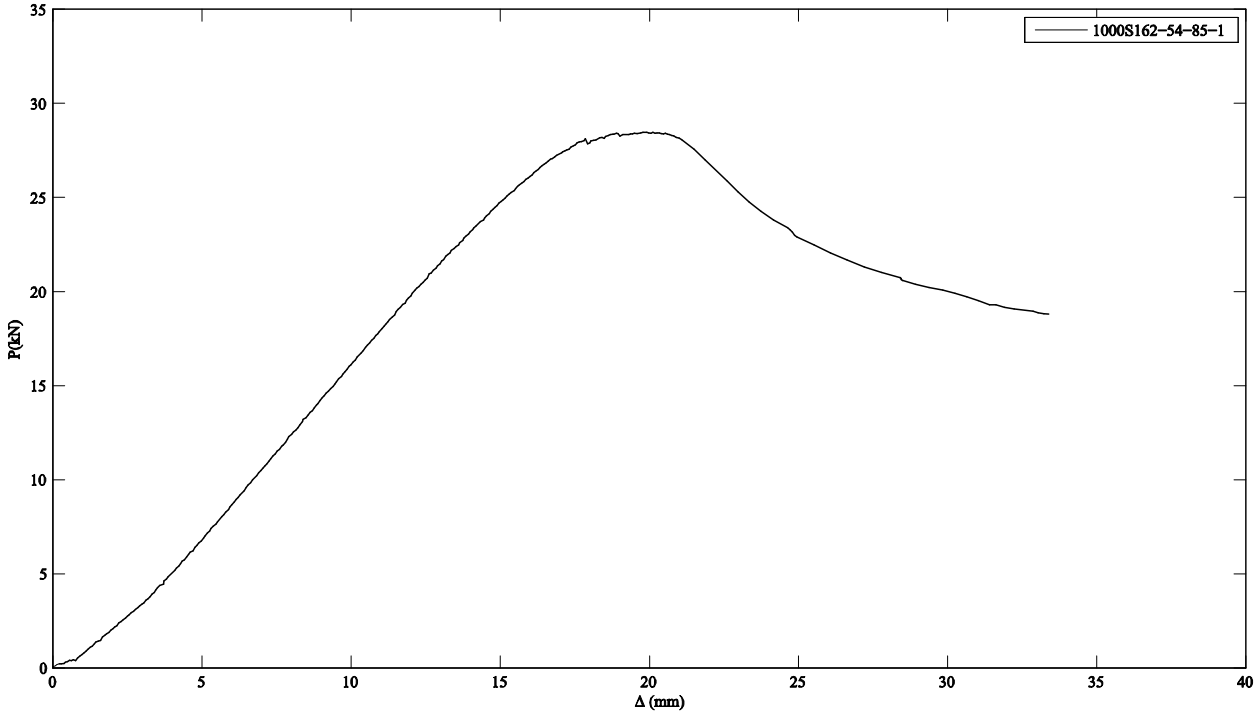

Notes:

Beams failed by distortional collapse

Dents were observed in the top and bottom flanges

1000S162-54-85-2

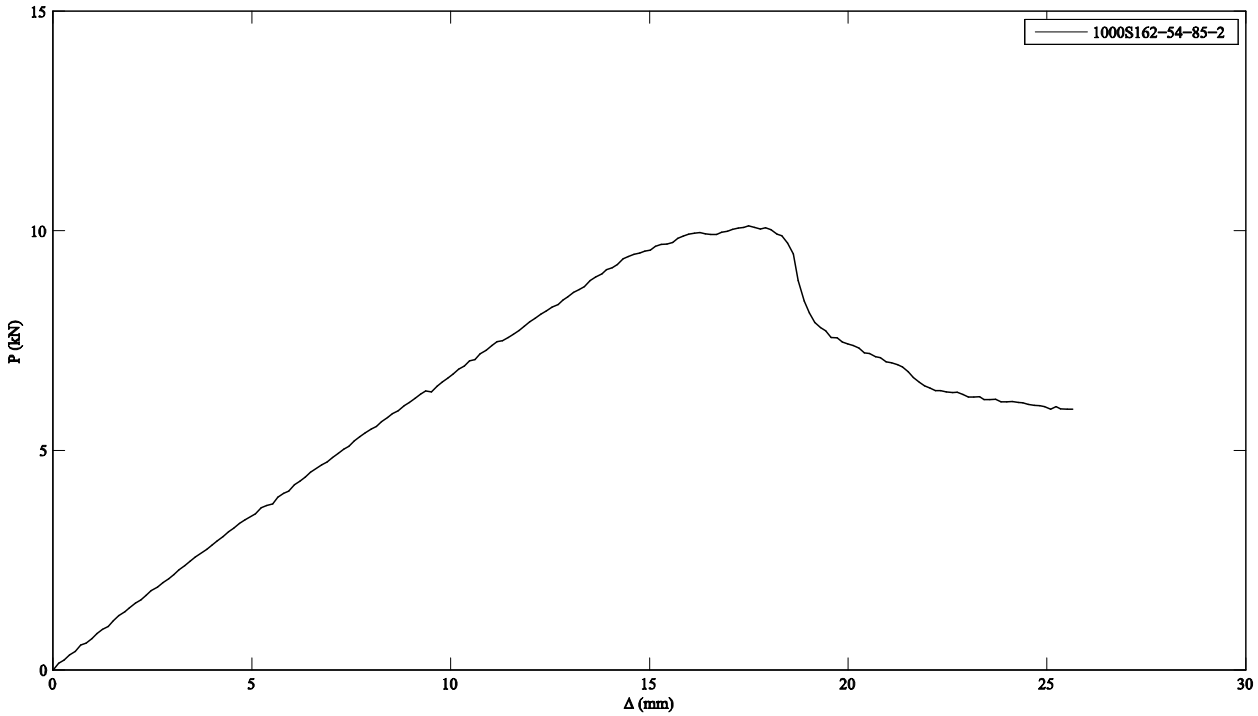

Notes:

Beams failed by distortional collapse

The scissor braces were adjusted while loading the beams

1000S162-54-85-3

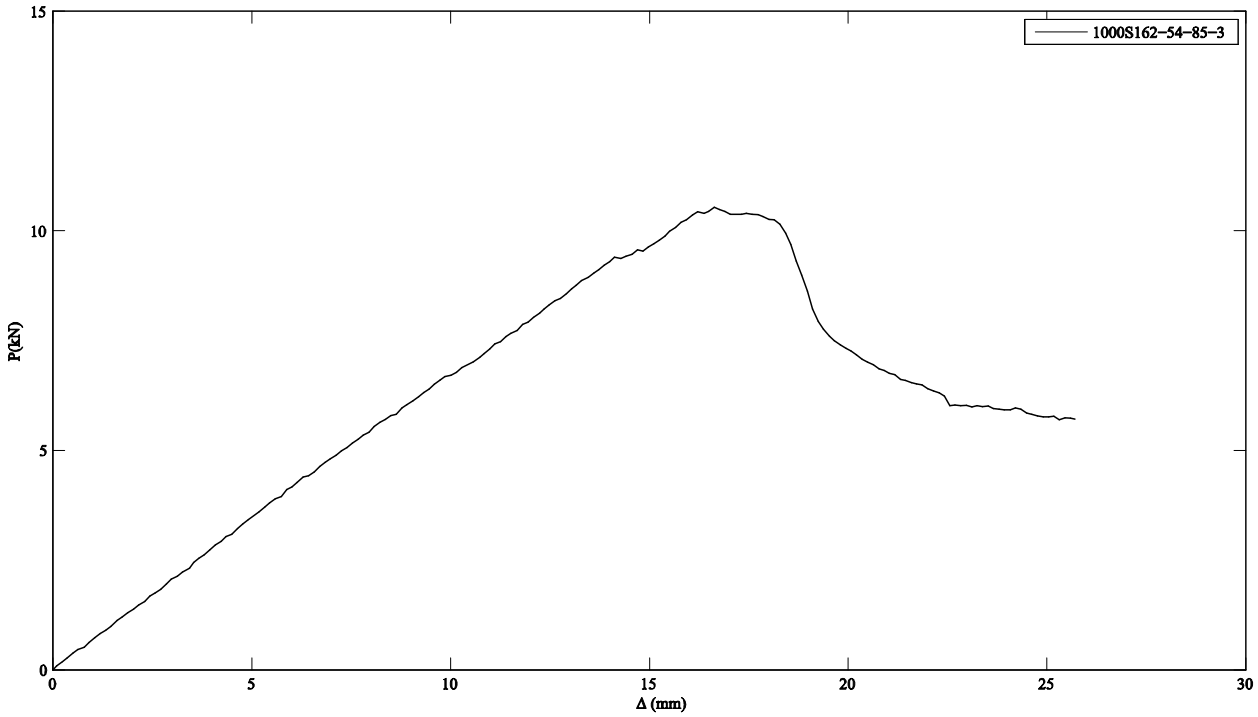

Notes:

Beams failed by distortional collapse

The scissor braces were adjusted while loading the beams

1200S162-97-100-1

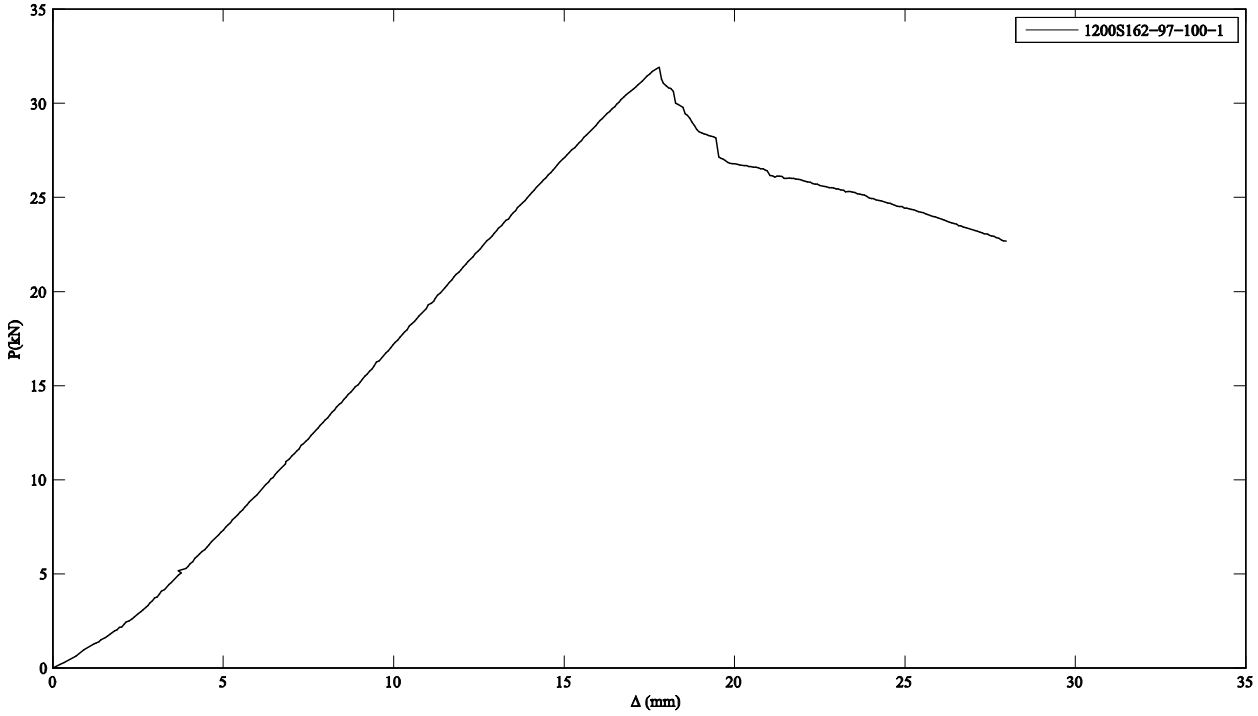

Notes:

Beams failed by distortional collapse

There is no photos available for 1200S162-97-100-1 beam specimens

1200S162-97-100-2

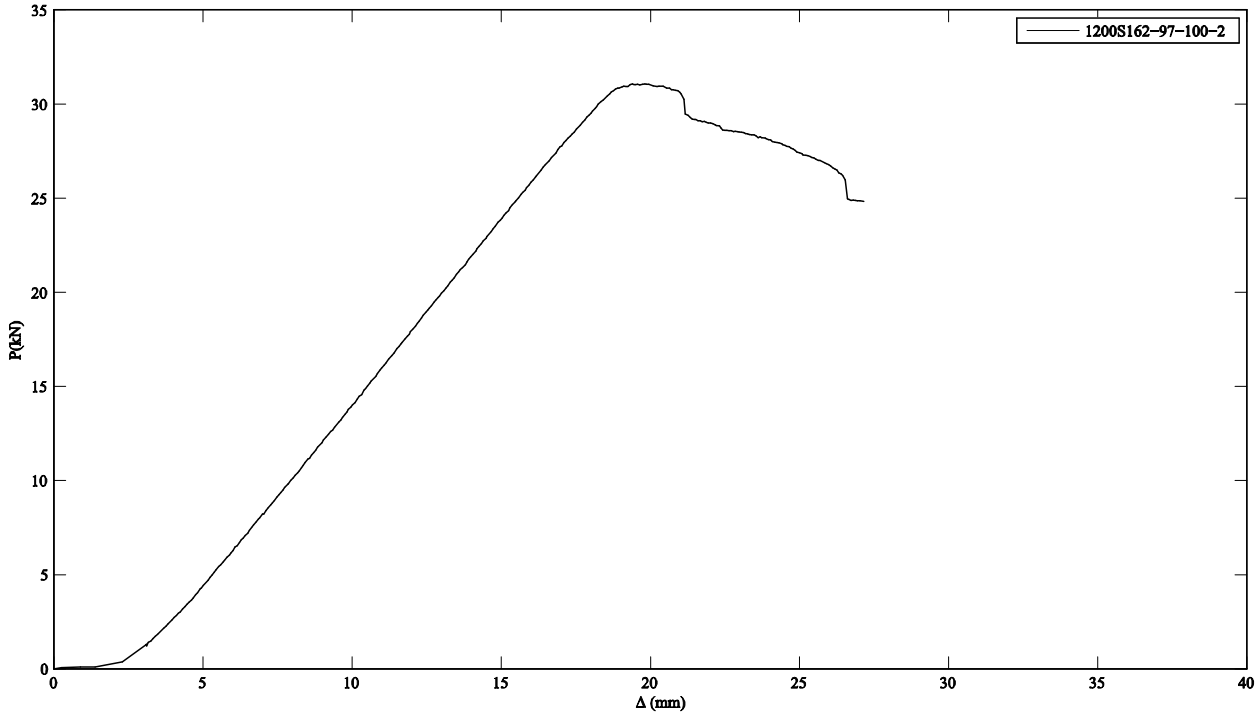

Notes:

Beams failed by distortional collapse

There is no photos available for 1200S162-97-100-2 beam specimens

1200S162-97-100-3

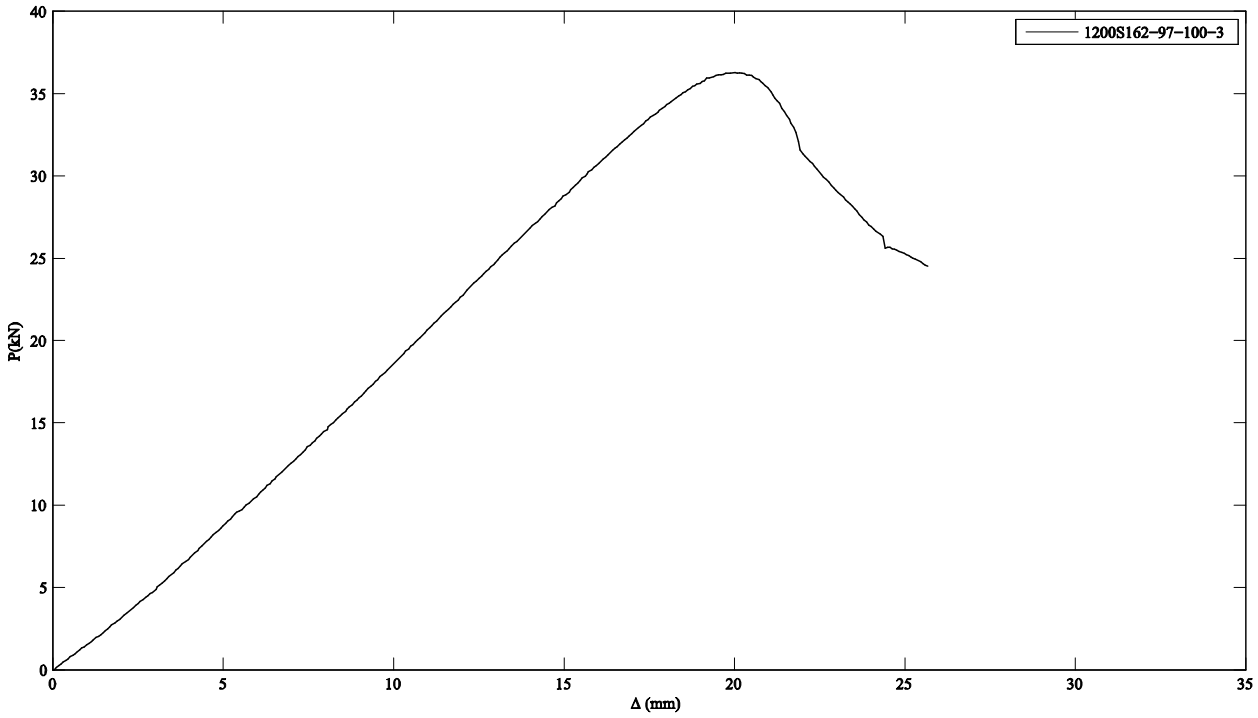

Notes:

Beams failed by lateral-torsional collapse

1200S162-97-95-1

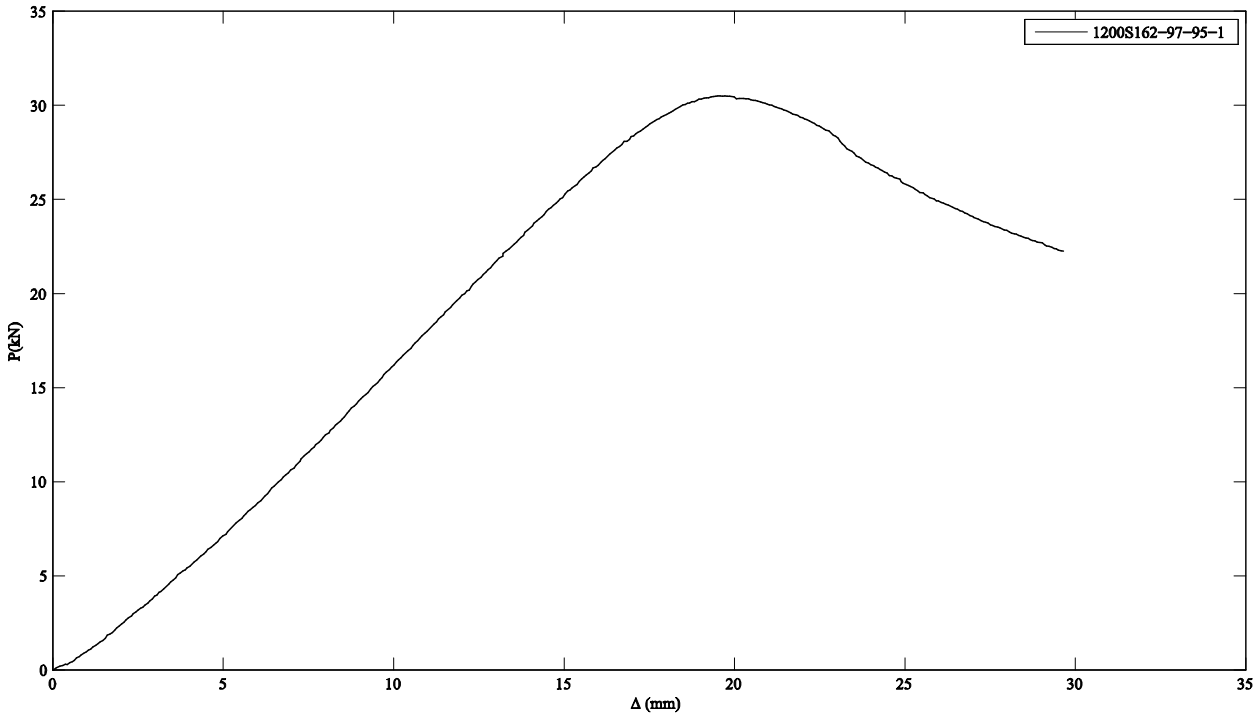

Notes:

Beams failed by lateral-torsional collapse

1200S162-97-95-2

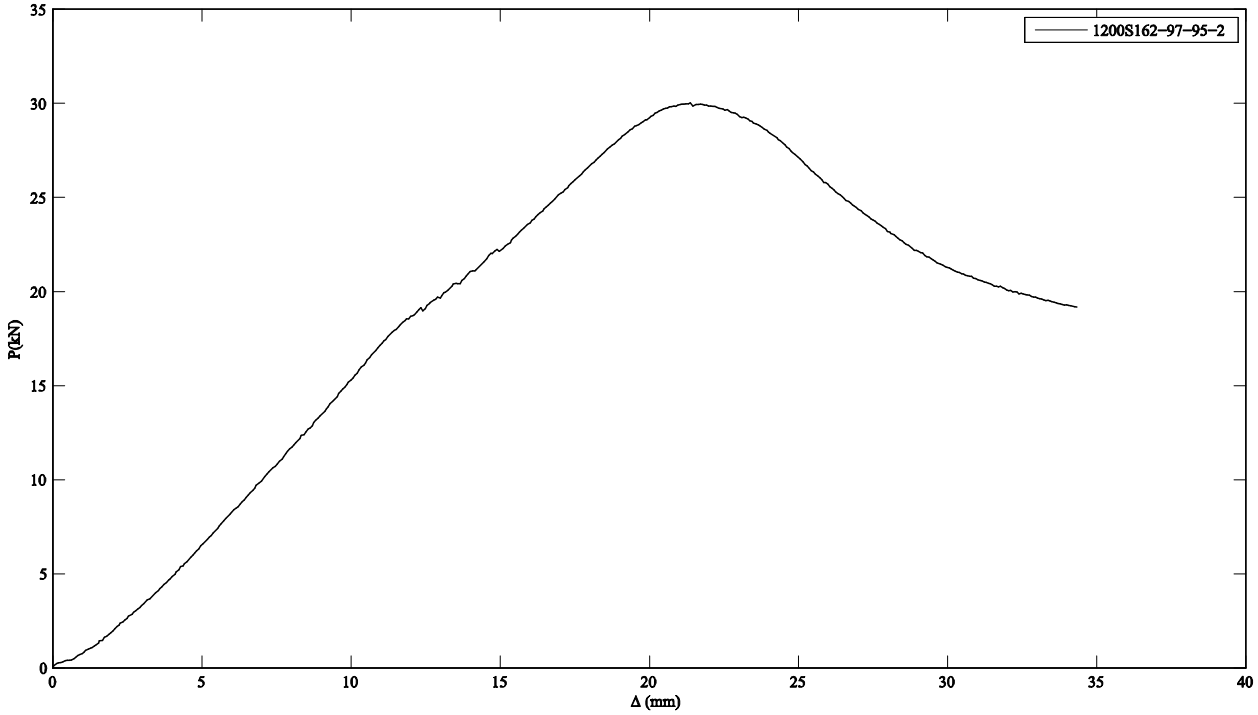

Notes:

Beams failed by lateral-torsional collapse

1200S162-97-95-3

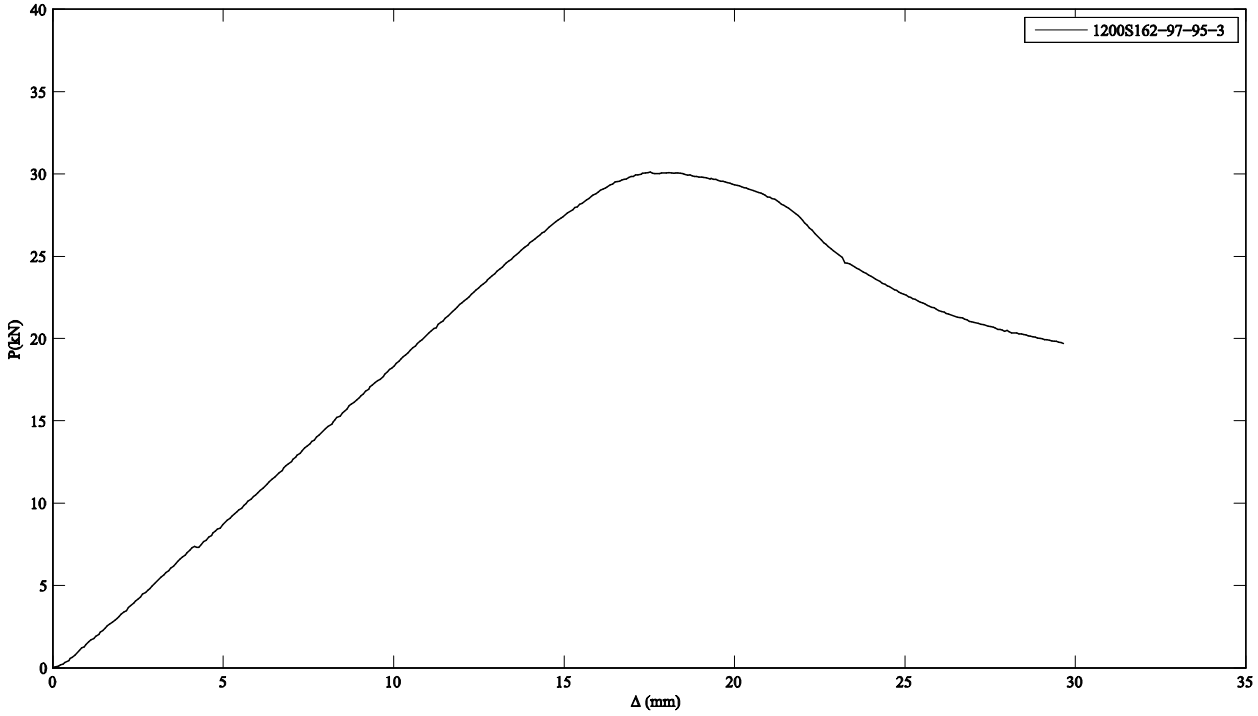

Notes:

Beams failed by lateral-torsional collapse

Dents were observed in the web

1200S162-97-90-1

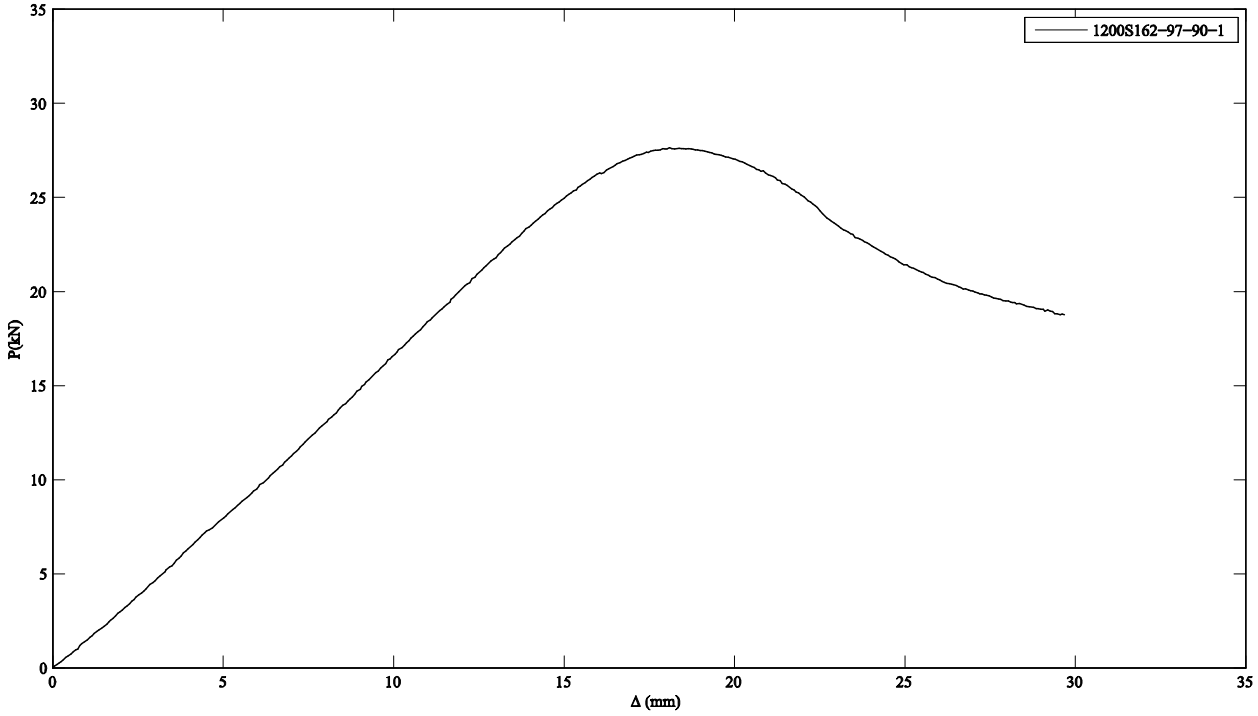

Notes:

Beams failed by lateral-torsional collapse

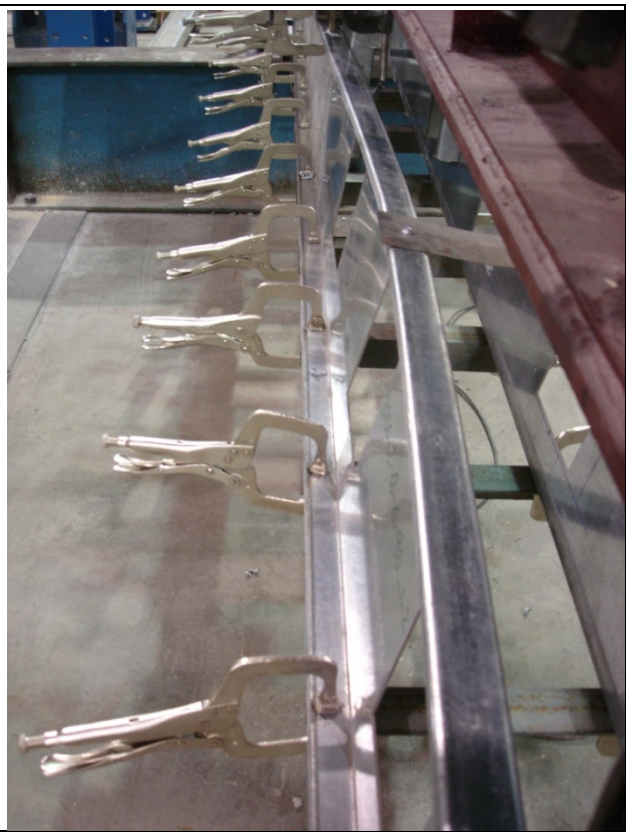

1200S162-97-90-2

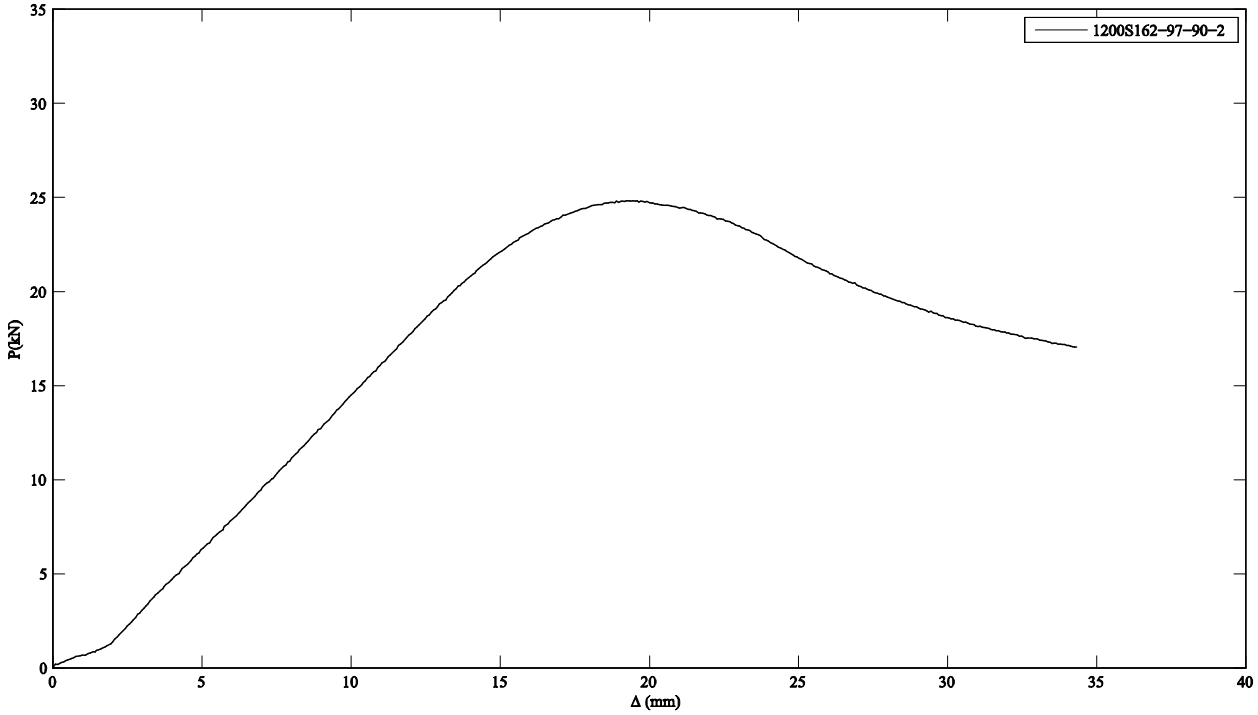

Notes:

Beams failed by lateral-torsional collapse

1200S162-97-90-3

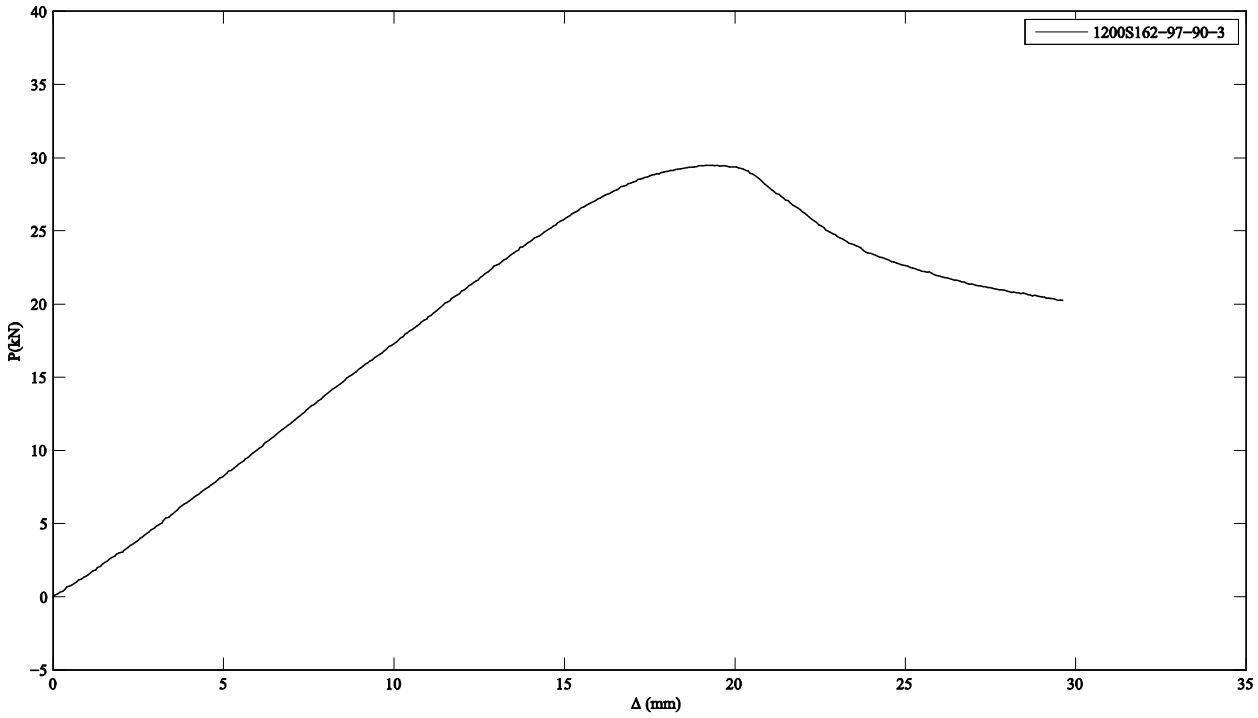

Notes:

Beams failed by lateral-torsional collapse

1200S162-97-85-1

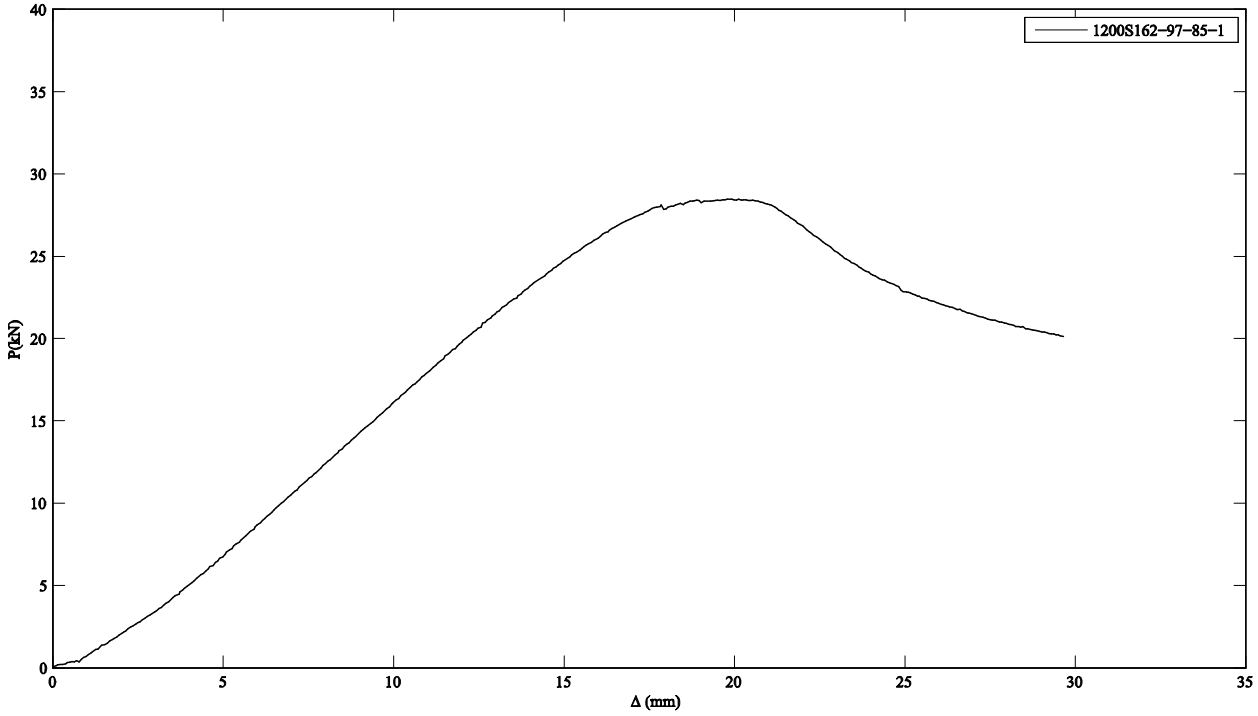

Notes:

Beams failed by lateral-torsional collapse

1200S162-97-85-2

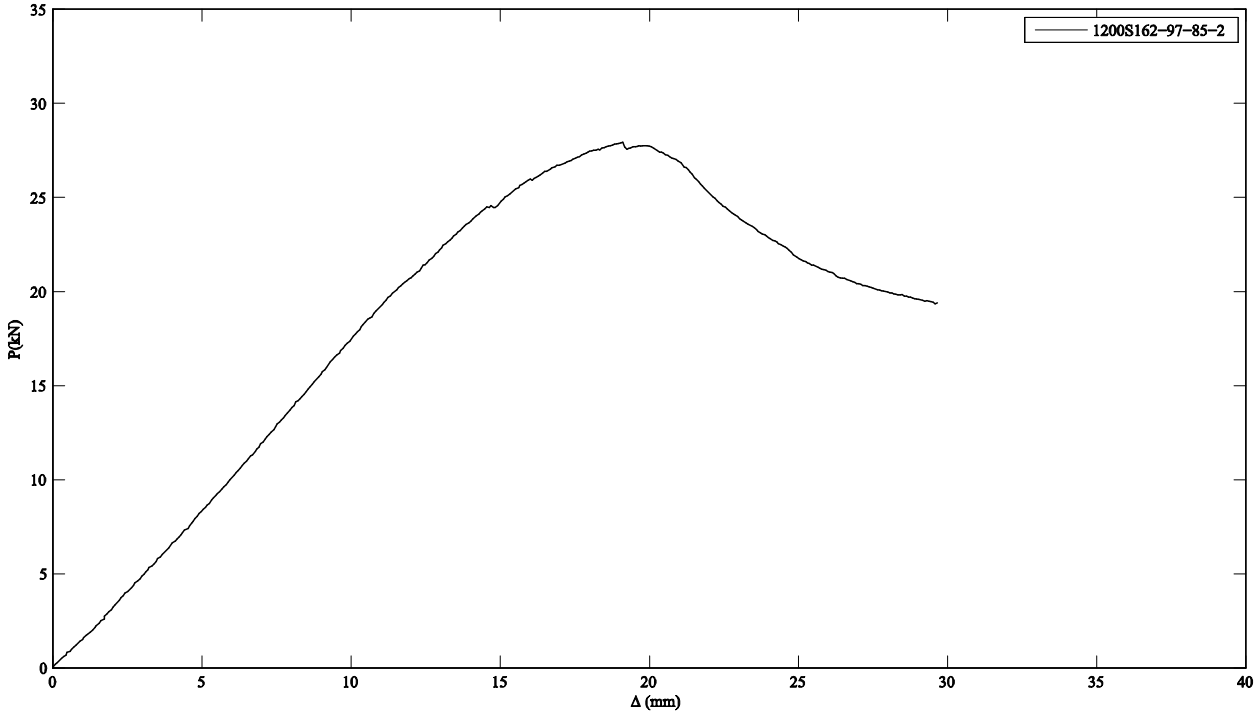

Notes:

Beams failed by lateral-torsional collapse

1200S162-97-85-3

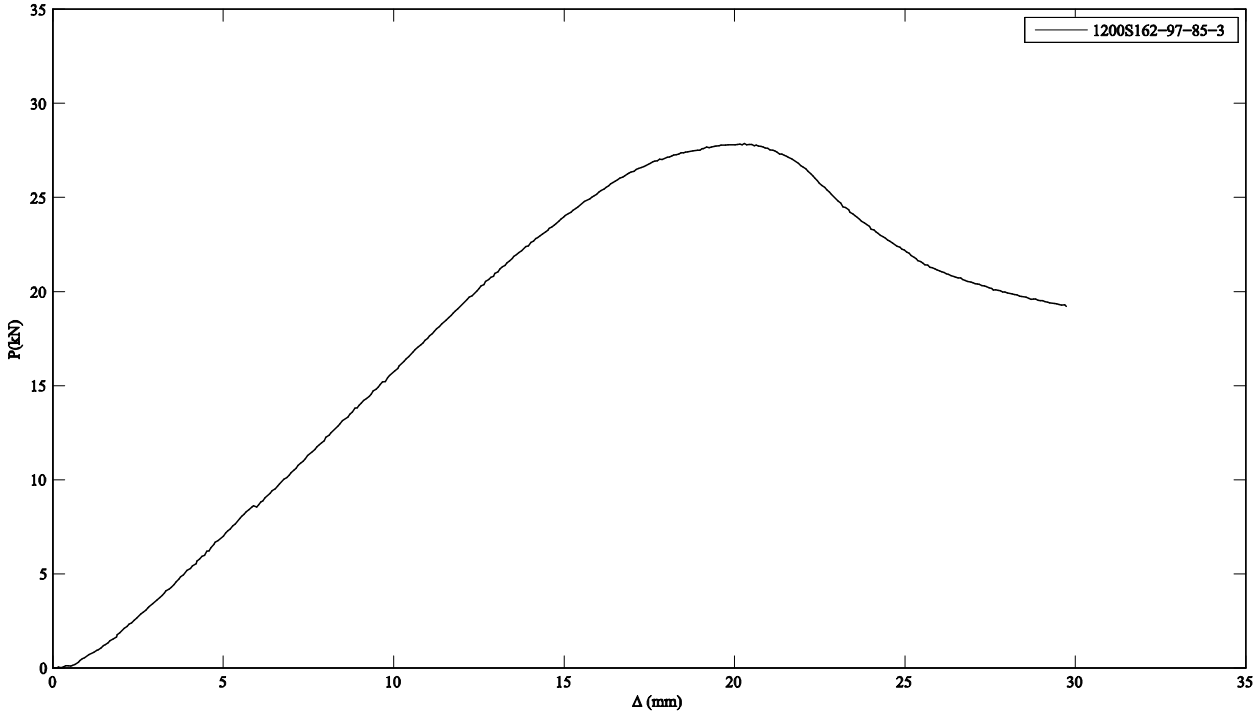

Notes:

Beams failed by lateral-torsional collapse